Vers une mesure précise du potentiel Casimir-Polder entre des atomes d'argon métastables et un nanoréseau en transmission.

Toward accurate measurement of Casimir-Polder potential between metastable argon atoms and nanofrabricated transmission grating.

THÈSE DE DOCTORAT
présentée par

Charles GARCION

pour l'obtention du grade de
DOCTEUR EN PHYSIQUE

soutenue le 1er décembre 2022 devant le jury d'examen composé de :

Mme. Laurence Pruvost, DR, Université Paris Saclay .... Présidente du jury
M. Eric Charron, Prof. Dr., Université Paris Saclay .... Rapporteur
M. Carsten Henkel, Prof. Dr., Universität Potsdam .... Rapporteur
M. Ernst Rasel, Prof. Dr., Leibniz Universität Hannover .... Examinateur
M. Benoît Darquié, CR, Université Sorbonne Paris Nord .... Examinateur
M. Gabriel Dutier, MCF, Université Sorbonne Paris Nord .... Directeur de thèse

Acknowledgments

First of all, I would like to thank Gabriel Dutier, who was my PhD supervisor. He was always available to answer all kinds of questions. I would like to thank him for these 3 years of work together during which he taught me a lot.

I am grateful to all the members of the Optics and Atomic Interferometry group. Francisco Perales, who has always given good advice, and was always ready to answer physics questions. Martial Ducloy for his knowledge. Quentin Bouton for his advice. Nathalie Fabre, for the discussion we had regarding nanostructures. Julien Lecoffre, who is always friendly and keeps the experiment going.

I acknowledge Naceur Gaaloul, with whom I collaborated on the simulations, and had some very interesting physics discussions. I would also like to thank the members of the simulation team from the university of Hannover, who always made themselves available. I would like to greet all the members of the Laser Physics Laboratory. Especially the doctoral students, with whom I had convivial moments. I am grateful to Isabelle Maurin and Olivier Gorceix who gave me the opportunity to teach at the IUT of Saint-Denis.

I am thankful to the members of the jury. Prof. Eric Charron (university Paris-Saclay) for his wise advice regarding the simulations. Dr. Benoît Darquié (university Sorbonne Paris Nord) for all the interesting discussion we had about testing a model. Dr. Laurence Pruvost (university Paris-Saclay), Prof. Carsten Henkel (university Potsdam) and Prof. Ernst Rasel (university Hannover).

I warmly thank my parents who have always supported me as well as my sister and my girlfriend.

Contents

Introduction

Atom-surface interactions have been studied since the 1950s through numerous experiments and many more theoretical developments, due to their close connection with fundamental physics. These interactions originate from the fluctuations of the electromagnetic field between the two bodies. In 1948, Casimir and Polder published an article in which they used a quantum electrodynamical approach to model the interaction of a neutral atom with a perfect conductor. Since then, we also refer to atom-surface interactions as Casimir-Polder interactions, regardless of the atom and the material.

This thesis describes a cold atom experiment designed to accurately measure atom-surface interactions. To date, the Casimir-Polder interaction potential has not been measured with better accuracy than 10%. Achieving an accurate measurement of the atom-surface interactions is of utmost importance since it constitutes a test for quantum electrodynamics theory.

Chapter 1 provides a brief historical review of the research on atom-surface interactions and also of the experimental techniques that have been used to study the Casimir-Polder potential. The experiment presented in this thesis is in the vein of experiments performed in the 2000s with nanostructures and supersonic atomic beams, but with a slow beam of atoms. Our experimental setup is detailed in chapter 2. A first model based on a semi-classical approach is reviewed in chapter 3. This model enables us to probe retarded effects for atom-surface distances smaller than 51 nm. It also enables us to see the strong correlations between experimental and theoretical parameters (e.g. the interaction strength and the nanostructure geometry) which are often considered as known and fixed. However, regarding the slow atomic velocities involved in the experiment, the eikonal approximation on which the presented semi-classical model is based doesn't hold anymore. Thus, this model has to be either corrected or replaced by a full quantum mechanical model. We decided to develop a model which is based on the numerical resolution of the time-dependent

Schrödinger equation. This new model is presented in chapter 4. This simulation gives access to the propagation of a wave function in a nanostructure by taking into account both atom-surface interactions and absorbing boundary conditions.

This new TDSE simulation leads to promising results for Casimir-Polder metrology. However, we must remain critical regarding the validity of our model in the presented experimental configuration. To this end, in chapter 5 we introduce statistical tools such as the χ^2-test, adapted to our experimental data, to perform goodness-of-fit tests. Only then, a rigorous Casimir-Polder measurement will open our results to physical subject of importance.

Chapter 1

Context

1.1 Brief history

1.1.1 Theory of atom-surface interactions

In the first half of the twentieth century, atom-atom and atom-surface interactions for neutral atoms were described using London's approach. London published an article in 1930, in which he derived the interaction energy between two neutral atoms. This energy is $\propto -1/l^6$, with l being the distance between the two atoms. London's approach considers that an atom has an instantaneous dipole because of the motion of the electrons. This instantaneous dipole affects the electron cloud of the second atom and thus induces a dipole. The interaction between the two atoms is then described by considering the dipole-dipole interaction.

This approach was also used to describe the interaction of a neutral atom with a perfect conductor.

Following London's work, Overbeek applied theory to colloidal systems. Overbeek emphasized that this approach did not reproduce the results of the experiment when the distance between the particles was large. Indeed, Overbeek noticed that for large distances the interaction energy was more of the form $\propto -1/l^7$.

A full discussion can be found in the article by Casimir and Polder [1]. In this article, the authors used a quantum electrodynamics approach to first derive the interaction energy between a neutral atom and a perfect conductor. The expression of the interaction energy they derived is $\propto -1/l^3$ for short separation distances between the atom and the surface l, while $\propto -1/l^4$ for large separation distances due to retardation effects. Second, they derived the interaction energy between two neutral atoms. The expression they derived becomes $\propto -1/l^6$ for short distances l between the atoms and $\propto -1/l^7$ for large l.

In 1956, Lifshitz published an article [2] in which, using a macroscopic approach, he derived the interaction energy between two media. The use of a macroscopic approach is possible until the separation distances are large compared to the interatomic distances. The benefits of the Lifshitz approach are listed below:

1. It enables one to calculate the interaction energy between two bodies for all kinds of material.

2. It takes into account retardation effect.

3. It is possible to take into account the temperature dependence.

4. By considering rarefied media, it is possible to retrieve both the interaction energy between a neutral atom and a surface (whatever the material), and between two neutral atoms.

Important remarks

Atom-atom and Atom-surface interactions in the non retarded limit, which are $V_{At-At} \propto -1/l^6$ and $V_{At-Surf} \propto -1/l^3$ respectively, are often called van der Waals interactions (one also talks about the van der Waals regime).

In the retarded limit, $V_{At-At} \propto -1/l^7$ and $V_{At-Surf} \propto -1/l^4$, one often talks about the Casimir regime. Nowadays, the atom-surface interactions tend to be called Casimir-Polder interactions. This denomination applies regardless of the material of the surface, the geometry, the temperature, and the distance between the atom and the surface. One also talks about the Lifshitz limit, when, for distances larger than the Wien wavelength (wavelength at which the thermal spectrum exhibits a maximum), the potential depends linearly on the temperature.

Review Articles and books

In this thesis, different phenomena of atom-surface interactions, such as repulsive interactions and temperature dependence, are not discussed. The interested reader is referred to the following review article [3], and for a more recent review article, see [4]. The book [5] that focuses on Casimir interactions has two chapters dedicated to Casimir-Polder interactions. S.Y. Bumahn's books [6][7] present in depth theoretical calculations of atom-surface interactions.

1.1.2   Experiments

We will not give an exhaustive review of all the experiments which treats about atom-surface interactions (see [5]). Here, we just briefly present mains experimental techniques, used to measure atom-surface interactions. There are four main experimental techniques.

1 - Atomic beam deflection:

A well-known experiment, which was also the first to probe the need to use the Casimir-Polder potential instead of the non-retarded regime $\propto -1/l^3$, is the experiment from E.A. Hinds' group [8]. In this experiment they used a supersonic beam of Sodium atoms. The beam was passing through a cavity made of gold plates. They measured the flux of atoms at the exit as a function of the cavity size (and thus the atom-surface distance). The flux loss was due to the sodium atoms sticking to the gold plates.

2 - Bose Einstein Condensate oscillation:

Some experiments used Bose Einstein condensate to explore the atom-surface interactions (between the atoms of the BEC and a surface). The principle relies on the modification of the trap potential when the BEC is brought close to the surface. This modification then influences the oscillation of the center of mass of the BEC. See, for example, the experiment by E. Cornell's group [9]. In this paper, the authors measured the Casimir-Polder interactions for separation distance between the center of the BEC and the surface $l \in [6, 12]$ μm.

3 - Spectroscopy:

Spectroscopy measurements are based on the energy shifts of atom energy levels resulting from the atom-surface potential. There are three often used spectroscopic methods :

- Selective reflection spectroscopy.
- Evanescent wave spectroscopy.
- Transmission spectroscopy of atomic vapor in thin cells.

Most of the time, it is performed on the vapor of Alkali atoms. Because the measurement is based on the displacement of the energy difference between two atomic levels, it is possible to study the atom-surface interactions for atoms in an excited state other than metastable (which is not very different from the behavior of a ground

state). For a review of atom-surface interactions that details the three spectroscopic techniques mentioned above, see [3].

4- Matter wave interferometry:

There have been two main approaches exploiting matter wave interference. Both approaches so far have used a material transmission grating, with a period of the order of 100 nm.

- Mach-Zender atom interferometer.

On this kind of experiments, the Mach-Zender interferometer is made out of three gratings, either optical [10], or material nanogratings [11]. In both experiments, they added a material transmission nanograting on one arm of the Mach-Zender interferometer. They measured the shift in the position of the diffraction pattern when the additional grating was moved in and out of the interferometer.

- Diffraction from material transmission nanogratings.

Instead of making use of Mach-Zender atom interferometers, some groups measured atom-surface interactions by placing a single nanograting in supersonic beams of atoms. They measured the interactions by modeling the diffraction envelope. The model was based on Fresnel diffraction, with the addition of a phase shift induced by the atom-surface interactions. The first measurement of atom-surface interactions using this technique was done in J.P. Toennies group [12] for helium and Krypton supersonic beams. In the same group, they also measured the atom-surface interactions for metastable[1] He* and Ne* [13]. It has been done in A.D. Cronin's group for Na atoms [14].

Another experimental technique to measure the Casimir-Polder potential is to observe the reflection of cold [15] or ultracold [16] atoms by a potential, which is the sum of the Casimir-Polder potential (attractive unknown) and an evanescent electromagnetic wave (repulsive known).

1.1.3 Main limitations in experiments

One of the main limitation that occurs in all experimental techniques is related to atomic species. When atoms stick to the surface, the atom-surface interactions are

---

[1]Metastable : long lifetime excited state.

modified, as experimentally studied in E. Cornell's group [17]. Thus, it is interesting to perform experiments using rare gas atoms.

The geometry of the object used as the surface also has a strong influence on the dependence of the atom-surface interaction potential with the distance. Furthermore, the atom-surface distance is also a challenging parameter to control.

Regarding some of the limitations, one notices that the experiments from J.P. Toennies group using He and Kr [12] and also He* and Ne* atoms [13] with a nanograting, are promising for precise measurements. In these experiments, there are two main difficulties. First, they used a thermal beam of atoms, so modifications of the diffraction envelope due to atom-surface interactions are small and thus difficult to measure. Second, the geometry and properties of the nanograting (slit size, shape, etc.) constitute the main source of systematic uncertainty.

Finally, whatever the experimental techniques used, the atom-surface interactions have not yet been carefully measured with a better accuracy than 10%.

1.2 The Villetaneuse experiment

The experiment presented in this thesis relies on atom interference method. Actually, it consists of the diffraction of atoms by a material nanograting.

The Villetaneuse experiment has been designed to address the drawbacks of atom diffraction experiments, such as [13]. In the present experiment, we also use rare gas (metastable argon atoms), but in a slow beam. Thus, the interaction time between the metastable argon atoms and the surfaces of the nanograting is increased. Moreover, the nanograting we use was designed and manufactured by the Optic and Atomic Interferometry (OAI) team members. Therefore, the geometry of the nanograting is known with better accuracy than in previous experiments. The experiment is presented and described in the following chapter.

Chapter 2

Experimental Setup

2.1   Introduction

The atomic diffraction experiment is analogous to diffraction experiments in classical optics. As illustrated figure 2.1, the experiment starts with a cold source of atoms, the atoms freely propagate from the source to the grating, pass through the grating, and are finally detected 30 cm after the grating.

The diffraction pattern is obtained after the detection of thousands of atoms. The observed diffraction pattern differs from the usual diffraction pattern in optics. Indeed, here we look at the diffraction of matter-wave by a material nanograting. When the atoms propagate through the grating, the atoms interact with the internal surfaces of the grating. Hence, the diffraction pattern carries information on atom-surface interactions.
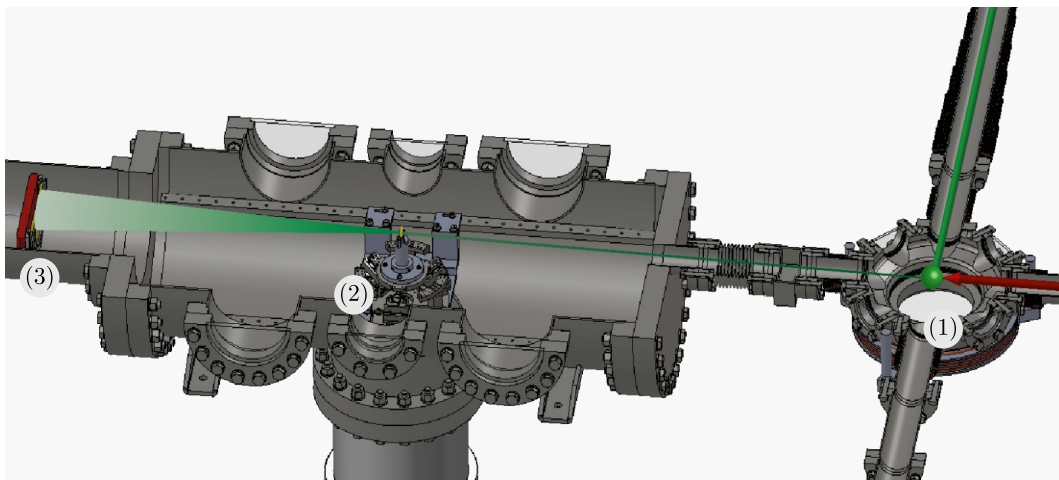

Figure 2.1: Matter-wave diffraction experiment principle. The diffraction experiment start with a cold atomic source (1), atoms pass then through the grating (2), and are detected 30 cm away (3).

The atomic diffraction experiment is performed with argon atoms in a metastable state, i.e with a long excited state lifetime, denoted by Ar*. There are two main reasons we work with Ar*, on the first hand, argon atoms in metastable state have enough internal energy to perform single atom detection using a MCP-DLD detector (see section 2.1.5). On the second hand, argon atoms belong to the rare gas family, thus when hitting the nanograting surface, it doesn't stick to it. Therefore the nanograting geometry is preserved along the experiments.

The whole experiment does not simply boil down to the diffraction chamber. We need to start the experiment by exciting the argon atoms from their fundamental level to the metastable level, then we need to cool them, before trapping them. The atomic trap which is simply a collection of Ar* will be the source of atoms for the diffraction experiment. The whole scheme of the experiment, from the argon gas bottle to the detection of the diffraction pattern is represented in figure 2.2.

The different numbers in figure 2.2 correspond to the following steps in the experiment :

1. Argon atoms exit the bottle of gas. Using a nozzle and a skimmer, we obtain a supersonic beam of fundamental Ar atoms ($v \approx 560$ m/s).

2. Ar atoms are excited by counter-propagating electrons. It leads to a mixture of Ar atoms in the fundamental state and in the states ($3p^5 4s$; $^3P_2$) and ($3p^5 4s$; $^3P_0$).

3. Ar atoms freely propagate over ≈ 30 cm. The metastable flux can be measured with a Faraday cup.

4. Atoms enter the Zeeman slower, where only the $^3P_2$ state Ar atoms will be slowed.

5. $^3P_2$ Ar atoms are then trapped in a magneto-optical trap (This will be the source for the diffraction experiment).

6. Finally, the $^3P_2$ Ar atoms are pushed with a laser beam, in the direction of the diffraction chamber. They pass through the nanograting and are detected on the MCP-DLD detector.

A detailed description of the different steps presented above can be found in [18].
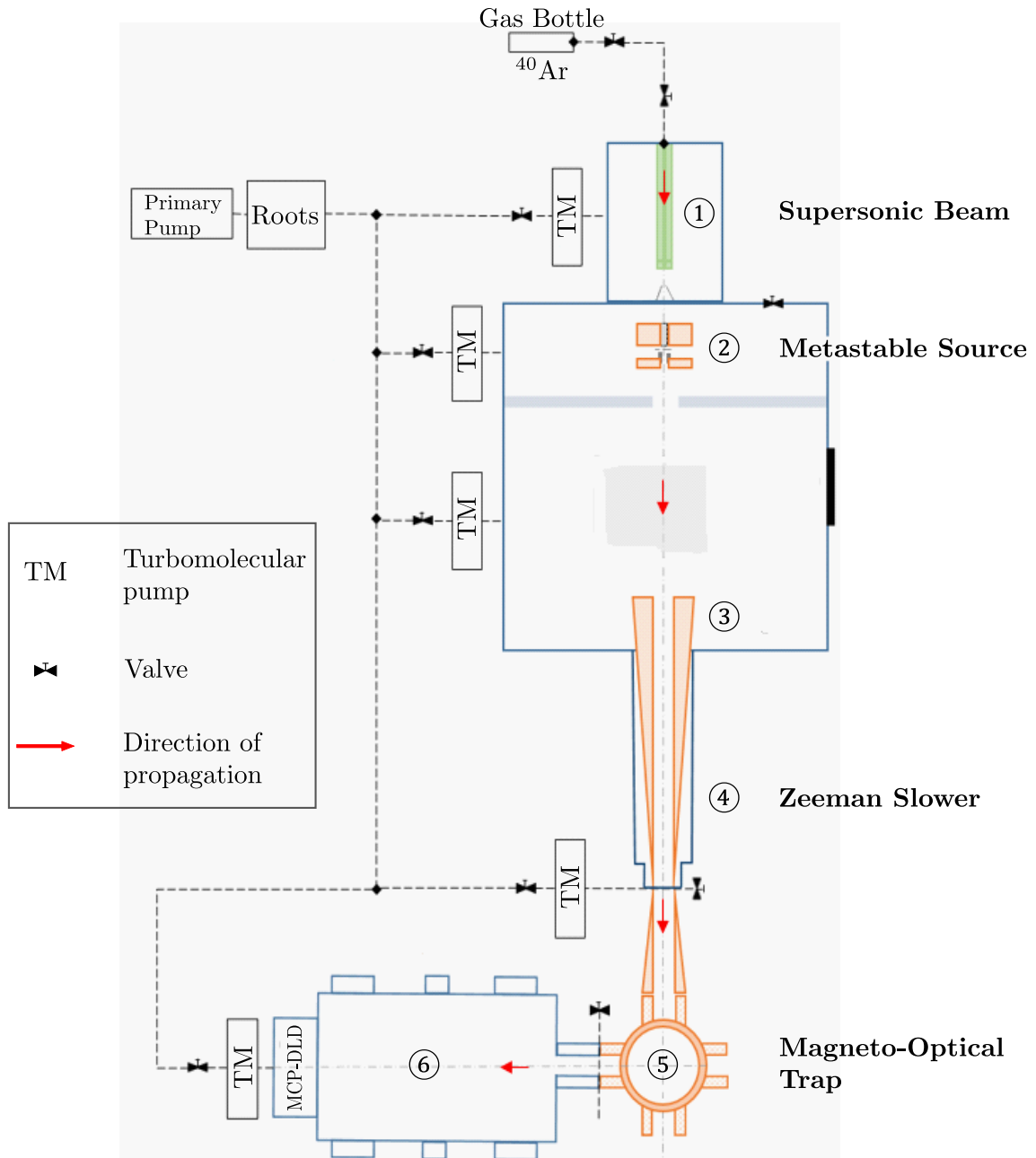
Figure 2.2: Experimental scheme

2.1.1   Argon levels

Some of the argon levels are represented figure 2.3. In the experiment, we take advantage of the closed transition at 811.531 nm (at rest in air) between states $^3P_2$ and $^3D_3$.
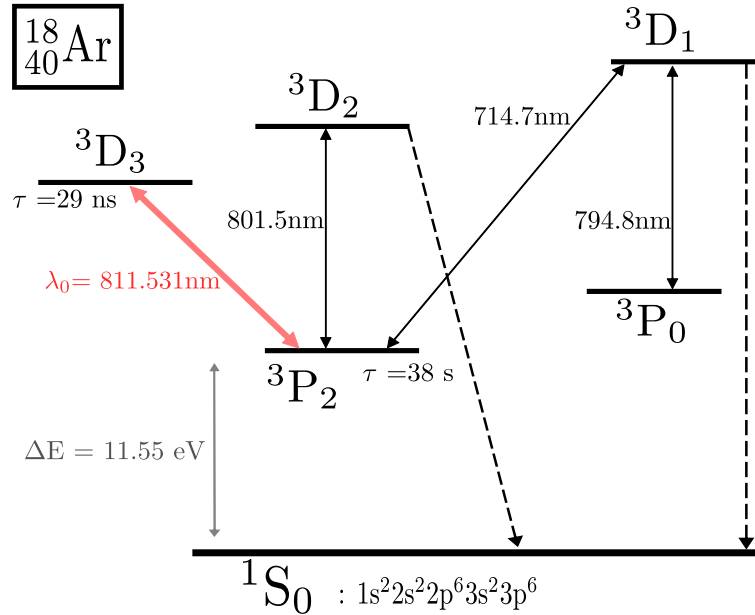
Figure 2.3: Argon levels, the red arrow represent the cycling transition we use in the experiment.

In the metastable state $^3P_2$ ($3p^5 4s^1$), Ar atoms have about 11.55 eV of internal energy. Thus, it is possible to perform single atom detection with a MCP-DLD (see section 2.1.5).

2.1.2   Zeeman Slower

After being excited in the $^3P_2$ state, the atoms enter the Zeeman slower at thermal velocities of about 560 m/s. There, (figure 2.4) an atom absorbs counter-propagating photons from the resonant laser beam. Since the momentum exchange due to spontaneous emission averages to zero, the atom loses momentum in its propagation direction.

The presence of the magnetic field splits degenerate levels, the σ^+-polarised laser populates and slow the atoms via momentum transfer on the transition $(^3P_2, m_i = +2) \to (^3D_3, m_f = +3)$. The change of magnetic field intensity along the propagation direction changes the energy difference between the two levels via Zeeman effect. This compensates the Doppler shift, so the atomic transition is resonant with the laser

Figure 2.4: illustration of the Zeeman slower

while atoms slow down. At the exit of the Zeeman slower (about 1 m long), atoms have velocities of a few tens of m/s (about 50 m/s). To get more details on our Zeeman slower, see [19].

2.1.3   Magneto-Optical trap

At the exit of the Zeeman slower, the Ar* atoms have sufficiently low velocities to be trapped in a 3D magneto-optical trap (MOT), which then is the source of cold Ar* for the diffraction experiment.

As illustrated in figure 2.5, the counter-propagating laser beams, red-detuned with respect to the atomic transition, exert scattering forces on the atoms. As the atoms go away from the center of the trap, a non-homogeneous magnetic field generated by coils in anti-Helmholtz configuration splits the degenerate levels by Zeeman effect. The laser beams being circularly polarized, it creates an imbalance between the scattering

Figure 2.5: illustration of the MOT

forces. Transitions with Δm_j=+1 (respect. -1) will absorb σ^+-polarized (respect.

17

σ^--polarized) light. Note that in figure 2.5, only two over all possible transitions have been represented. The temperature of the MOT in our experiment is about 150 μK. It has been estimated by fitting the density distribution. To get more details about our MOT, see [18].

2.1.4   Slow Ar* beam

The magneto-optical trap constitutes the source of cold atoms for the diffraction experiment. The principle of the diffraction experiment is illustrated in figure 2.6.
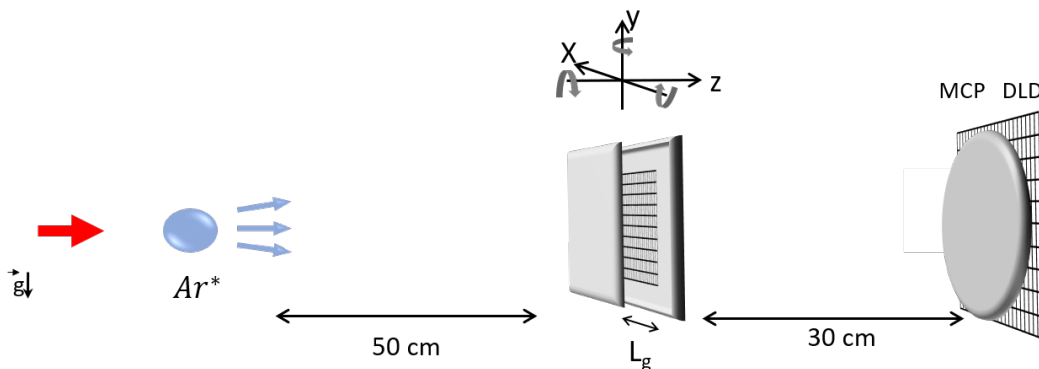
Figure 2.6: Ar* are pushed with a laser during t_p. After freely propagating over 50 cm, atoms pass through the nanograting. Finally, atoms are detected 30 cm away from the nanograting with a MCP-DLD

To produce the slow beam of Ar* atoms, we start by turning off all laser beams of the MOT, while at the same time, the pushing laser beam is turned on during t_p (note that the magnetic field of the MOT is always on, but we recently added a switch to turn it off in future experiments). After the atoms have been pushed, the MOT laser beams are turned on, and the MOT is loading until another cycle is started.

To give orders of magnitude, the MOT laser beams are turned off for 5 ms, at the same time the pushing laser is turned on for 0.4 ms. At the end of the 5 ms, the atoms are far from the trap, so we can turn on the MOT again. Then the MOT is loading for 65 ms. Therefore, a full cycle is about 70 ms. One has to find an optimum between the loading duration of the MOT and the total cycle duration to have the maximum atomic flux.

To change the final velocity of the atoms, it is possible to either push more or less longer the atoms by adjusting t_p, or to adjust the detuning of the pushing laser beam. In the experimental results presented in section 2.4, we only changed the detuning of the pushing laser beam, thus for both velocity ranges, we have the same

pushing time t_p.

The spontaneous emission that occurs during the pushing process implies that the beam of Ar* is divergent. Its divergence depends on the interaction time, but also on the detuning of the pushing laser, and on the magnetic field of the MOT (which is always on). This has been characterized in [20], where the authors showed that the divergence of the Ar* beam is well described by a random walk.

Due to the divergence of the Ar* beam, and the opening surface of the nanograting (1x1 mm^2), we have to select the beam with a metallic plate, see figure 2.6, to increase the visibility of the interfringes. This increases the transverse coherence of the beam.

The nanograting is placed on a hexapod from SmarAct company in order to position it in the atomic beam. This enables us to move and rotate the nanograting in all directions. Thus, the nanograting angle with respect to the direction of propagation of the atoms can be precisely adjusted. Using the hexapod, the minimum translation increment possible is 1 nm and the minimum rotation increment is 1 μrad.

Note : When one wants to spatially select the beam, one has to be careful on the choice of material. Here, Ar* have about 11.5 eV of internal energy, which is sufficient to pull out electrons from materials ($\propto$ 5 eV to pull out electrons from metals). Indeed, we observed a lot of electronic noise on the detector while using a piezo slit, and the same when using slits made in too thin objects. The problem seems to be solved by making use of a thick grounded metallic plate.

2.1.5   Detection

2.1.5.1   MCP-DLD detector

Ar* atoms are detected with a microchannel plate (MCP) coupled to a delay line detector (DLD), which is referred to as MCP-DLD in the following.

The principle of this MCP-DLD is illustrated in figure 2.7. When an Ar* atom hits the MCP, it has enough internal energy to tear out an electron. This electron is accelerated by an electric field. The accelerated electron can trigger an electronic avalanche which reaches the copper lines, and induces a current impulse that can be detected on both sides of the lines. Resolving the arrival time of the current impulses on both sides of the copper line, and, knowing the length of the copper

line, the position where the electronic avalanche hits the line is determined. This detector is able to detect the arriving positions of a single atom.
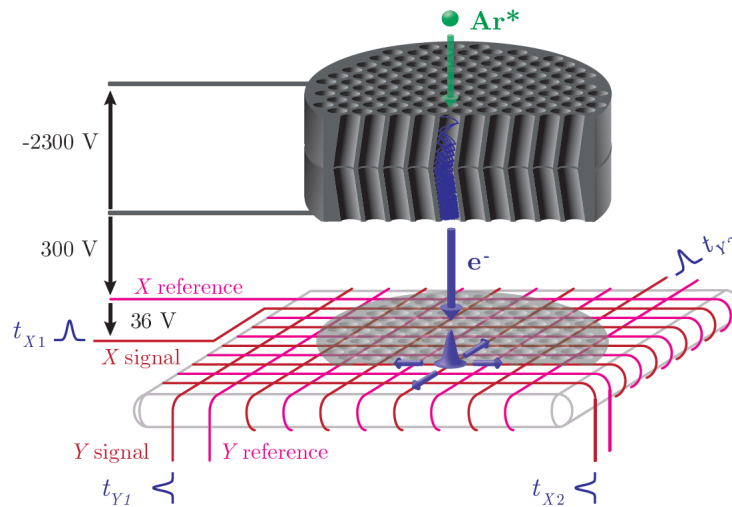
Figure 2.7: MCP-DLD detector principle

The announced characteristics of the detector by RoentDek Handels GmbH company are the following :

- Diameter : 80 mm
- Spatial resolution : 150 μm
- Temporal resolution : 2 ns

2.1.5.2 Distortion test pattern

The MCP-DLD is capable of detecting a single atom in position, but is the position the detector pretends to have detected an atom the real position at which the atom arrived?

Our measurement method of the atom surface interactions relies on the ability of the detector to detect the spatial distribution of atoms. Thus, we need to characterize if there is any spatial distortion. To do so, we manufactured a test pattern, illustrated figure 2.8a. We place this pattern in front of the detector.

(a) Distortion test pattern

(b) Detected pattern on the detector
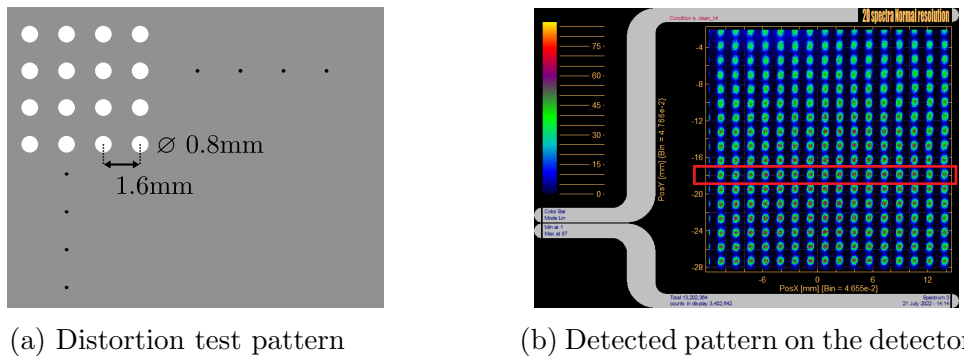
Figure 2.8: Spatial distortion characterization

The holes in the manufactured pattern let the atoms pass, so we just need to see if the detected atoms reproduce the test pattern, see figure 2.8b.

The first thing one can do is illustrated in figure 2.9a. The black curve corresponds to the 1D projection of one single line of holes of the detected atoms on the horizontal axis (see figure 2.8b). The red curve in figure 2.9a is the symmetric of the black curve with respect to the vertical axis. The test pattern is periodic, hence if there are no distortions one should see the red peaks overlap the black ones. Here, the peaks do not overlap, so there are spatial distortions.

(a) Before spatial distortion correction

(b) After spatial distortion correction
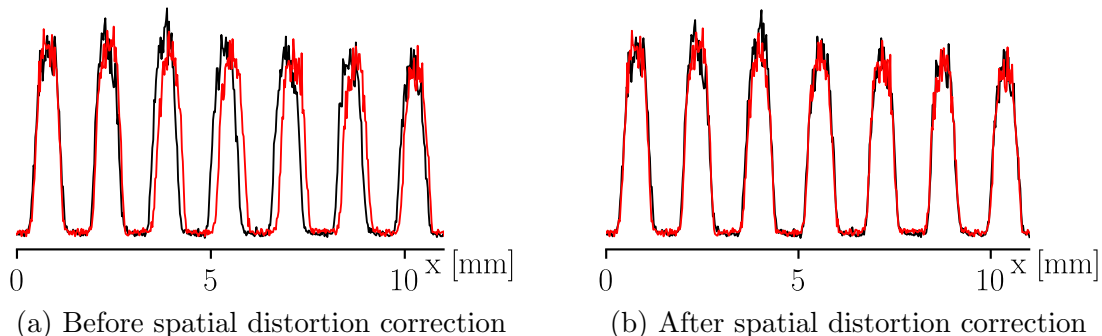
Figure 2.9: Distortion test

To correct the spatial distortion, we superimpose the theoretical shape of the test pattern (red curve) to the detected pattern (black curve), see figure 2.10a. Then we look at the position difference between the middle of a black peak and the position it should be. One can then construct the correction function figure 2.10b.

When this correction is applied to the detected pattern, we can perform the same analysis as before. In figure 2.9b, the black curve corresponds to the spatially corrected atom pattern, the red curve is the symmetric with respect to the vertical axis. There the red peaks overlap the black ones therefore the spatial distortion has been successfully corrected.

21

(a) Principle of the correction

(b) Correction function
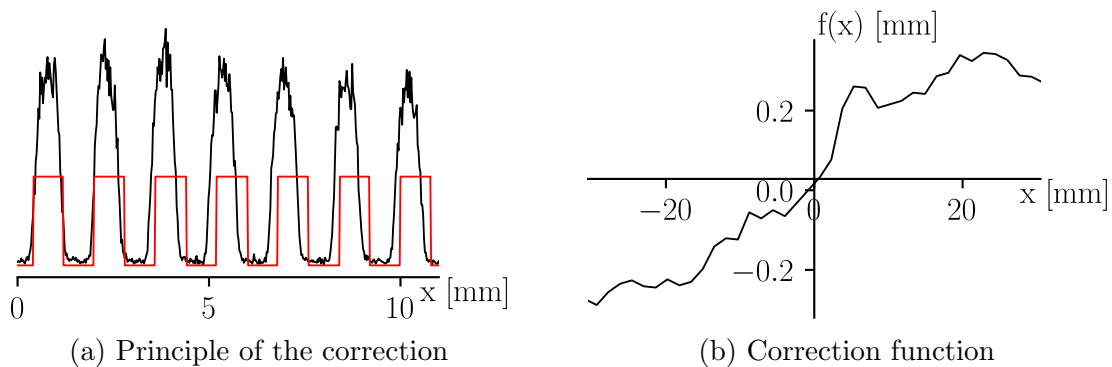
Figure 2.10: Principle of the correction

2.1.6 Velocity measurement

In the atomic diffraction experiment, the atom-surface interaction potential will modify the diffraction envelope but not the interfringe. The interfringe on the detector is given by : $i = (\lambda_{dB} D_{gd})/p_g$, where λ_{dB} is the de Broglie wavelength, D_{gd} the grating to detector distance, p_g the period of the nanograting.

As in optics, from the interfringe we have two possibilities, either getting λ_{dB} knowing D_{gd}, or getting D_{gd} knowing λ_{dB}. In the experiment, it is difficult to have an accurate measure of the distance from the grating to the detector. This is due to different reasons such as the different accesses in the vacuum chamber, but we also do not want to put a ruler in contact with neither the nanograting nor the microchannel plate. As a consequence, we have a large uncertainty of a few percent on D_{gd}, and hence on the propagation velocities of the atoms. We decided to measure atoms propagation velocities by mean of a deflection method succinctly presented hereafter, and thus to get D_{gd} knowing λ_{dB}. Interested readers will find a detailed description of the deflection method in [21].

2.1.6.1 Principle

The principle of the deflection method is illustrated in figure 2.11. In this method, one makes use of the time detection resolution of the detector. It is performed after the atoms stop interacting with the pushing laser beam (and are far from the influence of $\vec{B}_{\text{MOT}}$), thus the atoms are freely propagating.
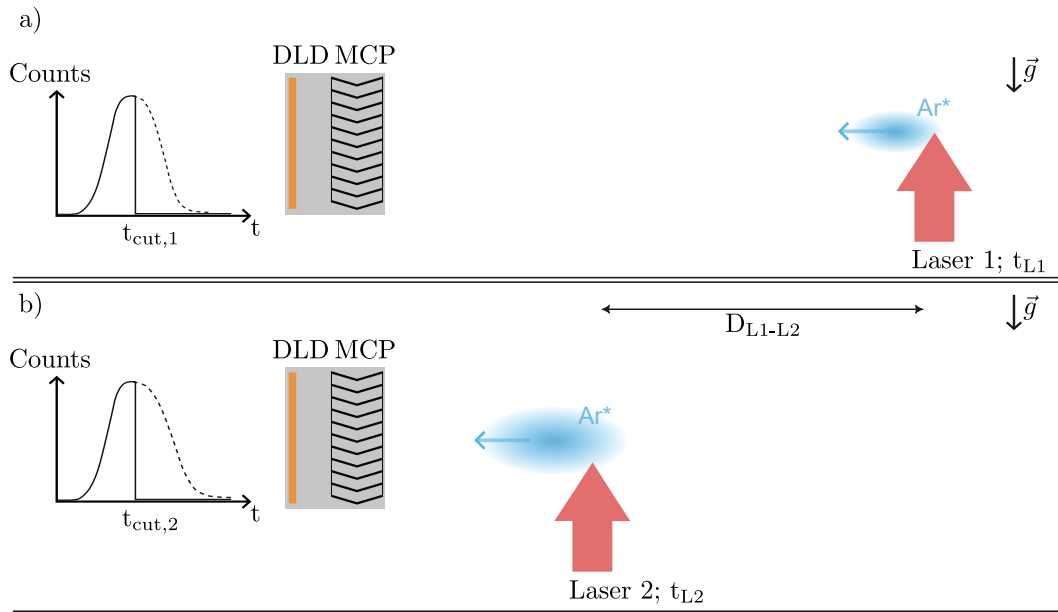
Figure 2.11: Light chopper using two resonant lasers orthogonal to the propagation axis. The measurement is performed in two steps, first with the laser L1 inset a), and second with the laser L2 located D_{L1-L2} further, inset b).

The measurement is performed in two steps. First, a laser perpendicular to the atoms propagation axis is turned on at a time t_{L1}, thus, slower atoms with time of flight larger than $t_{cut,1}$ are not detected. Second, we do the same with another laser located further on the atoms propagation axis, one has to turn on this second laser at a time t_{L2} such that we do not detect atoms with time of flight larger than $t_{cut,2}=t_{cut,1}$. Therefore, the propagation velocity of the atoms that reach the detector at $t_{cut,2}=t_{cut,1}$ is given by $v = D_{L1-L2}/(t_{L2} - t_{L1})$.

It is possible to measure the distance between the laser 1 and 2 outside of the experimental chamber. We measured the separation distance $D_{L1-L2} = 266.5 \pm 1.3$ mm. The determination of $t_{cut,1}$ and $t_{cut,2}$, depend on the slope of the induced discontinuity in the time of flights, and so on the atomic flux. Thus for the velocity ranges in the experimental data presented in section 2.4, the accuracy on the time sequence is about 8 ‰ for atomic propagation velocity $v \approx 19$ m/s, and 1 ‰ for $v \approx 26$ m/s.

2.1.6.2   Velocity variation due to free fall

The velocity measurement techniques described in the previous section give us an accurate measure of the longitudinal velocity v_z. Although, while atoms freely propagate after the pushing time, they experience free fall. Thus, atom propagation velocity $\vec{v} = v_y.\vec{e_y} + v_z.\vec{e_z}$ is not constant. In the following, we give orders of magnitude of the velocity variation Δv due to the free fall and show that it is indeed negligible under our experimental conditions.

After a free propagation during t, the velocity variation due to the free fall is given by

$$
\begin{aligned}
\frac{\Delta v}{\|\vec{v}(0)\|} &= \frac{\|\vec{v}(t)\| - \|\vec{v}(0)\|}{\|\vec{v}(0)\|} \\
&= \sqrt{\frac{v_{0z}^2 + (v_{0y} - gt)^2}{v_{0z}^2 + v_{0y}^2}} - 1.
\end{aligned}
\tag{2.1}
$$
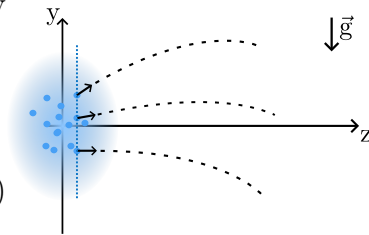
Figure 2.12: Velocity distribution after the pushing process

Let $v_{0z} = 20.0$ m/s, be the longitudinal velocity measured with high accuracy. This corresponds to the atoms selected by their time of flight, $t = 40$ ms. To get the velocity variation of equation (2.1), we need to estimate v_{0y}. During the pushing process, the atoms experience a random walk. So, the velocity distribution along the y-axis, at the end of the interaction with light, follows a Gaussian distribution with standard deviation $\sigma_{v_{0y}} = v_{recoil}\sqrt{N_{abs}}/\sqrt{3}$, see [20]. Knowing that the recoil velocity is $v_{recoil} \approx 1.23$ cm/s, the number of photons absorbed to reach v_{0z} is about $N_{abs} \approx 1600$. Therefore, $\sigma_{v_{0y}} \approx 0.29$ m/s. Since the velocity distribution along the y-axis follows a Gaussian distribution, 99.7% of the initial transverse velocity v_{0y}, will be in $[-3\sigma_{v_{0y}}; 3\sigma_{v_{0y}}] = [-0.9; 0.9]$ m/s. Finally, we can estimate the velocity variation due to free fall, for atoms freely propagating during $t = 40$ ms : $\Delta v/\|\vec{v}(0)\| \in [1; 0.1]‰$.

Actually, all pushed atoms will not pass through the nanograting (1 mm height) nor the laser beams for the velocity measurement (≈ 1 mm Ø). This means that the nanograting, or the lasers, select the velocity distribution along the y-axis. Thus, the velocity variation due to the free fall for atoms of interest (those that pass through the nanograting) is smaller than the variation we estimated before.

To continue to give orders of magnitude, we take the idealized case illustrated in figure 2.13, where the source is aligned with the nanograting. Here, we take $y_{max} = +360$ μm $= -y_{min}$, and $h_{max} = 0.5$ mm $= -h_{min}$. If the nanograting is

located 50 cm after the source, then $|v_{0y}| \leq 0.16$ m/s, and so $\Delta v/\|\vec{v}(0)\| \leq 0.05$ ‰. This is negligible compared to the accuracy we have on the velocity measurement of the longitudinal velocity v_z.

Hence, under our experimental conditions, it is reasonable for atoms selected by their TOF, to neglect the velocity variation due to the free fall. Therefore, we consider that atoms (selected with respect to their TOF) propagate freely with a constant velocity given by $v = D_{L1-L2}/(t_{L2} - t_{L1})$.
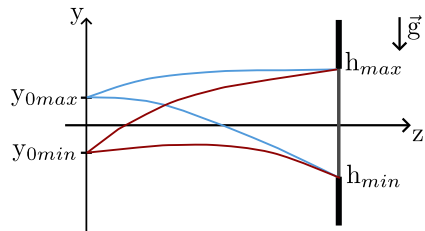
Figure 2.13: Velocity distribution and selection, implied by the nanograting height

2.2 Optical setup

In order to manipulate the atoms (to cool them trap them and push them), we use the laser system illustrated in figure 2.14. The different optical elements are represented figure 2.15. The optical setup has been redesigned compared to the one presented in [21] after we finished the acquisition of the two experimental results presented in section 2.4. The main goal was to gain stability. The first amplifier used, TA 100 (from Toptica Photonics), introduced instabilities such as mode jumps when used at too high current intensities. We observed the same phenomenon after replacing it by a new tapered amplifier BoosTa pro also from Toptica Photonics. To gain stability, we decided to use two amplifiers, each working at lower current intensities.

2.2.1 Brief overview of the optical system

Only one wavelength is needed in the laser system. The master laser is a Narrow-Diode (at 811.5 nm) from Radiant Dyes Laser company. This diode can be scanned in our optical system over 6 GHz without mode hops when properly adjusted. The laser beam is then injected in a tapered amplifier TA 100. At the exit of the TA 100 we use a fiber coupler 80/20. At exit 20, 20% of the total exiting power is used to inject the second amplifier. The exit with 80% of the total exiting power is used for the Zeeman slower, and for the saturated absorption spectroscopy to lock the laser. Also one can see from figure 2.14 that the laser beam is shifted in frequency of -160 MHz by double pass in a 80 MHz AOM before going to the saturated absorption setup. Hence, the master diode is locked at $\lambda_0 + 160$ MHz.

The second amplifier (BoosTa) is used for the magneto-optical trap laser beams, and the pushing beam. The laser beams of the MOT have to be red-detuned, so we have to shift the laser frequency a few MHz with respect to the transition wavelength. Small frequency shifts are obtained by double-pass AOMs. The master diode is locked at $\lambda_0 + 160$ MHz, thus using a double-pass $(80\pm\Delta)$MHz AOM, we have $\lambda_0 + 160$ MHz$-2(80 \pm \Delta)$ MHz $=\lambda_0 \pm 2\Delta$, where $\Delta \in [0, 15]$ MHz.

2.2.2 The different wavelength and laser intensities

The different laser intensities and wavelength on the optical system at the locations identified by numbers from 1 to 5 on figure 2.14, are the following :

1. $\lambda_0 + 160$ MHz, laser beam intensity: $I_1 = 51$ mW.

2. λ_0, laser beam intensity: $I_2 = 22$ mW.

3. $\lambda_0 - 340$ MHz, laser beam intensity: $I_3 = 27$ mW.

4. $\lambda_0 - 2\Delta_{MOT}$ MHz, laser beam intensity: $I_4 = 51$ mW.

5. $\lambda_0 \pm 2\Delta_{Push}$ MHz, laser beam intensity: $I_5 = 7$ mW.
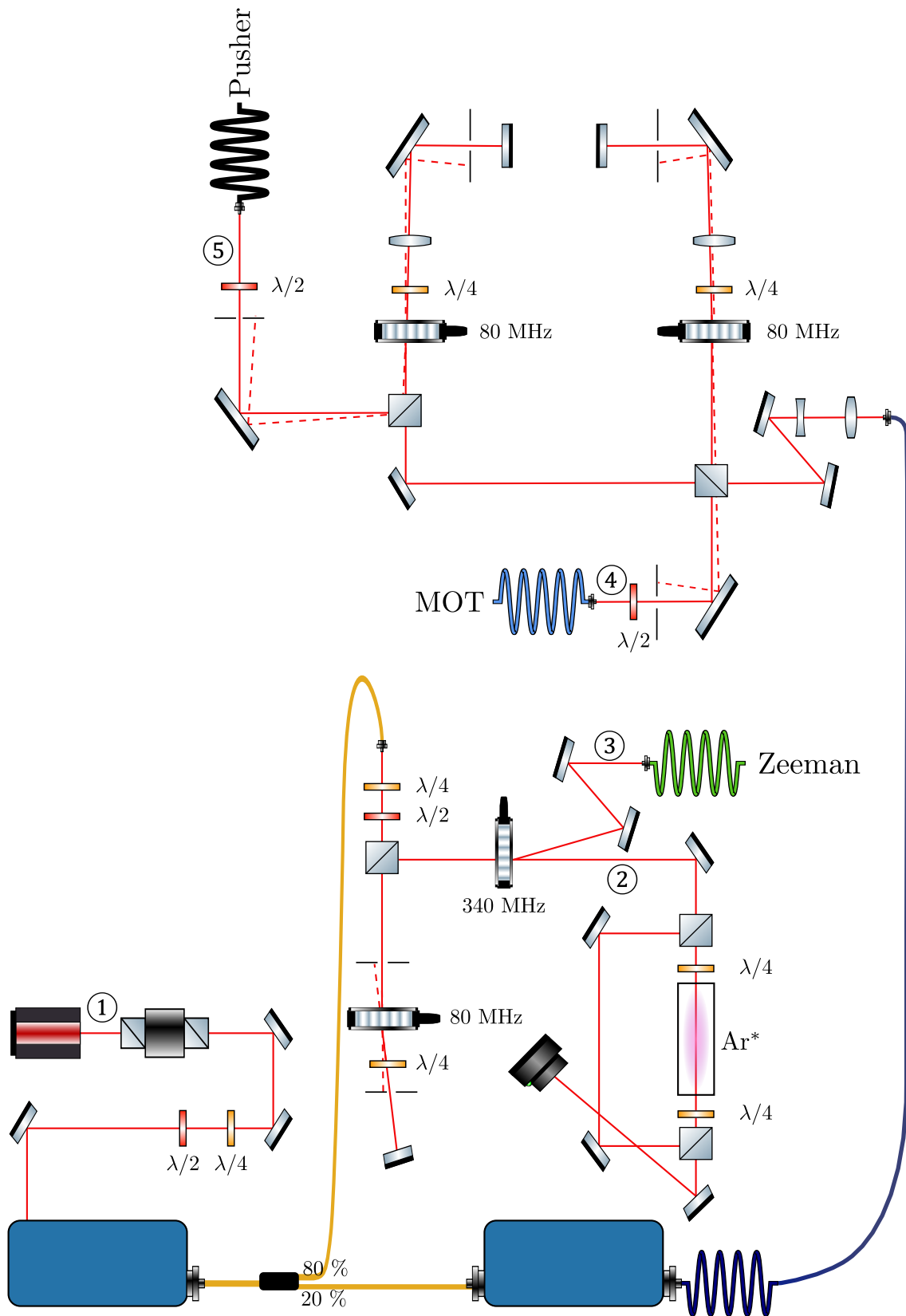
Figure 2.14: Optical setup

$\lambda/4$

$\lambda/2$

Beamsplitter

Faraday Isolator

Fiber

NarrowDiode

Ar^*

Argon Cell

Photodiode

Tapered Amplifier

Convergent Lens

Divergent Lens

Mirror

Accousto-Optic Modulator

80 %

20 %

Fiber Coupler
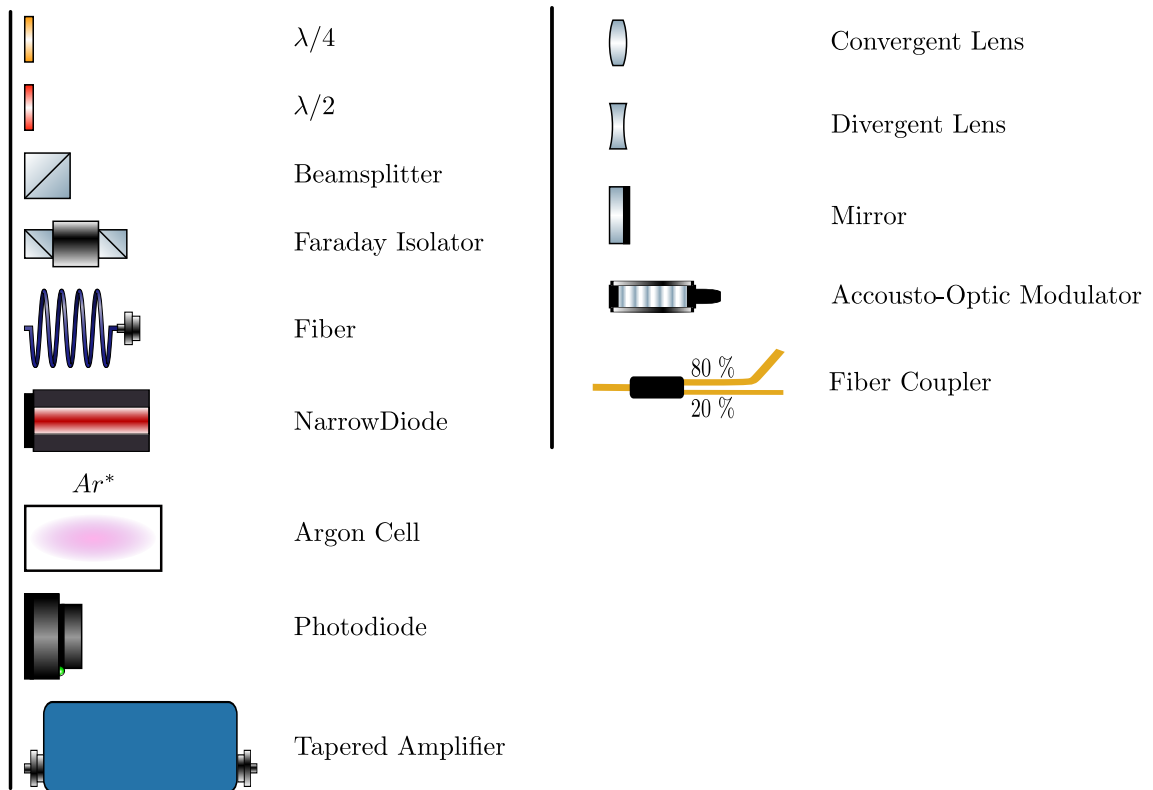
Figure 2.15: Optical components

2.3   Nanograting

The nanogratings previously used in the OIA group have been manufactured by UV-lithography. It was lent by professor Alexander D. Cronin (University of Arizona). The problems of those UV made gratings were their geometry characterizations. Moreover, such kind of nanogratings are no longer produced. Thus, it has been decided in the OIA group to develop their own transmission nanogratings. It was the subject of Hanane Bricha Tazi's PhD thesis [22]. The manufacturing process has changed, and now the nanogratings are made by electronic beam lithography instead of UV-litography. This enables a better control of the geometric properties. Also, rather than measuring atom-surface interactions from available nanogratings, the nanogratings made in the OIA group are developed in order to study atom-surface interactions.

The first nanograting produced in the group was made in October 2019. Unfortunately it has some defects such has holes, i.e that several bars of the nanograting were damaged. So, more atoms passing through the nanograting were contributing to the zeroth order of interference. Another nanograting has been produced by Nathalie Fabre in June 2020 at the IEMN (Lille). This nanograting does not have any holes or other observed defects on scanning electronic microscope images. This is the nanograting presented hereafter and from which we obtain the diffraction patterns presented section 2.4.

2.3.1   Scanning electron microscope images of the nanograting

The nanograting is in fact a collection of nanogratings over a surface of 1x1 mm^2. As observed in figure 2.16, there is a collection of squares of size 30x30 μm^2, each of the squares is made of twenty lines, each line contains 150 slits. These slits are the actual diffracting elements for matter waves. In total, over the whole surface of the nanograting, there are 1 323 000 slits.
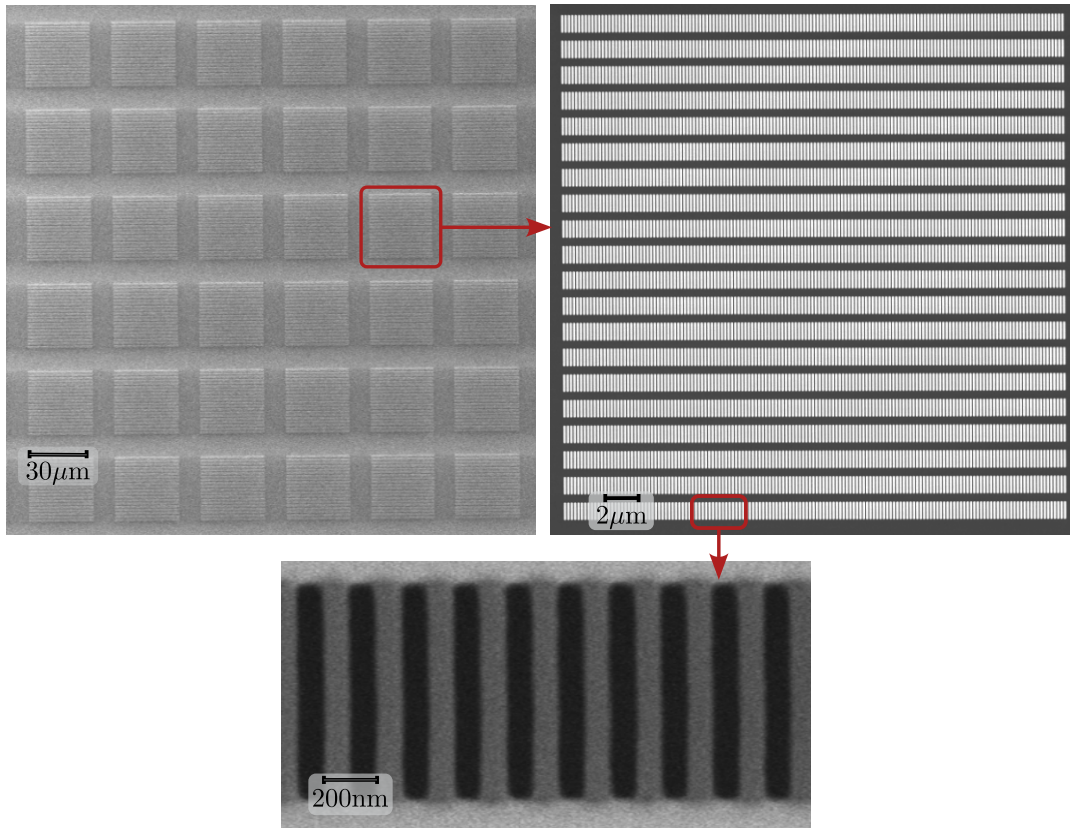
Figure 2.16: view face of the nanograting, SEM images

2.3.2   Geometrical characterisation

From the SEM images, we now characterize the geometrical properties of the nanograting. The scale given on the different SEM images is mostly indicative, and we cannot use it to perform a measurement of the slit size. Moreover, the choice of the positioning of the cursors on the SEM software is arbitrary. Thus it is not really precise since one can be influenced by the relative intensity on the images.

The image figure 2.17, corresponds to a cleaved nanograting, during the manufacturing process (i.e., the slits are not opened, z will correspond to the propagation axis).
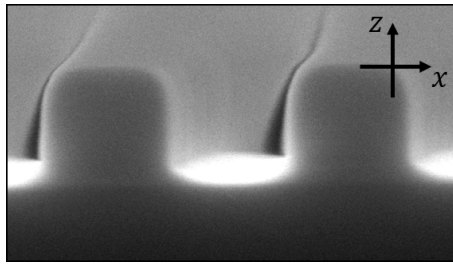
Figure 2.17: SEM image of a cleaved nanograting during the manufacturing process. The slits are not opened, the propagation axis correspond to the z-axis.

We see from the cleaved grating that the slits do not have a straight shape over all depth of the slits (z-axis).However, it is not trapezoidal as in UV-made nanogratings. The estimated geometry in depth of the slits is illustrated in figure 2.18b, in total, the depth is 100 nm (announced by the manufacturer of the membrane on which we perform e-beam lithography).

(a) Slit shape by UV-lithography

(b) Slit shape by electron-lithography
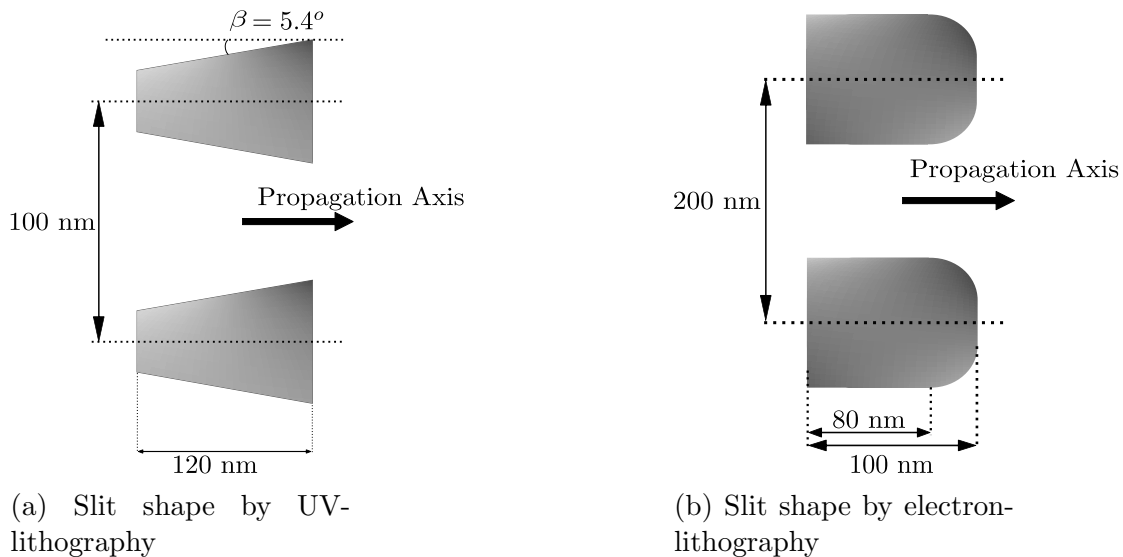
Figure 2.18: Nanograting in the propagation direction

When plotting the intensity profile from SEM images such as in figure 2.16, one does not find a square function. This is due to the electron beam of the SEM which has a Gaussian intensity profile, see figure 2.19.

The intensity profile obtain from SEM images is the result of the convolution product between a Gaussian (electron beam) and a square function (the grating). We plotted in figure 2.20 the intensity profile from the projection on the horizontal axis between the two
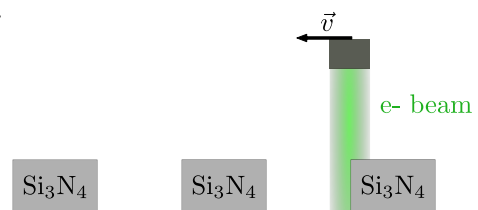
Figure 2.19: illustration of SEM imaging of the nanograting

31

blue lines represented in the inset. This is in order not to be affected by the stadium shape of the slits, as one can see from the most zoomed image figure 2.16.
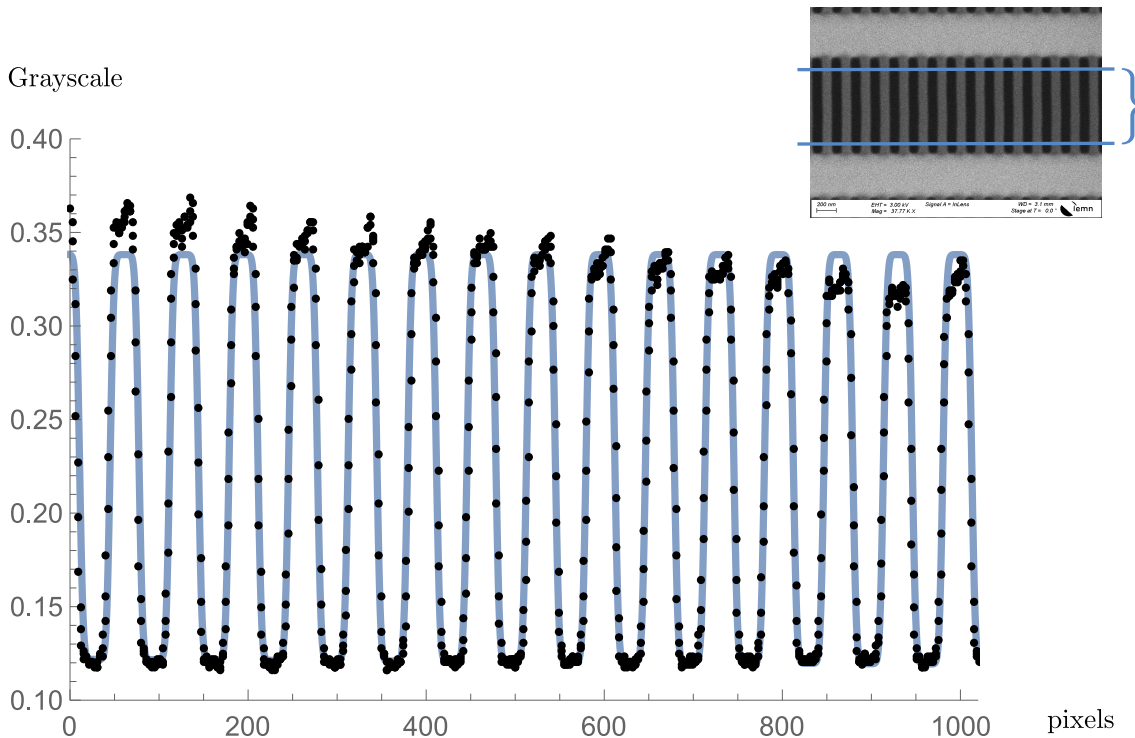
Figure 2.20: Projected profile from SEM images (Black dots) and the fit (Blue curve)

In figure 2.20, the blue curve is the result from the convolution product of a Gaussian function with a square function. The fit returns the best parameters in pixels. In the manufacturing process of the nanograting, the only fixed parameter is the period, which is 200.0 nm for this nanograting. From this and the period in pixels obtained from the fit, we get the conversion factor from pixel to nanometer.

To estimate the size of the slits, we divided the image from the SEM in slice on the height. Then we find the slit size from the fit in each of the slices projections illustrated figure 2.21a. The result is given figure 2.21b, we see the influence of the stadium shape.

Moreover, the slit size comes from a fit over multiple slits, thus it is an averaged size. On a picture, all slits don't have the same size, indeed the slit sizes vary between $[\overline{a}_{slit} - 3\ nm; \overline{a}_{slit} + 3\ nm]$, where $\overline{a}_{slit}$ is the averaged slit size obtained from the fit.

Due to the stadium shape, the slit size vary over its height, with $\overline{a}_{slit} \in [92.1; 102.7]$ nm, see figure 2.21b.

(a) Illustration of the slices to get slits size dependence on the stadium shape

(b) Slit size distribution in the slices
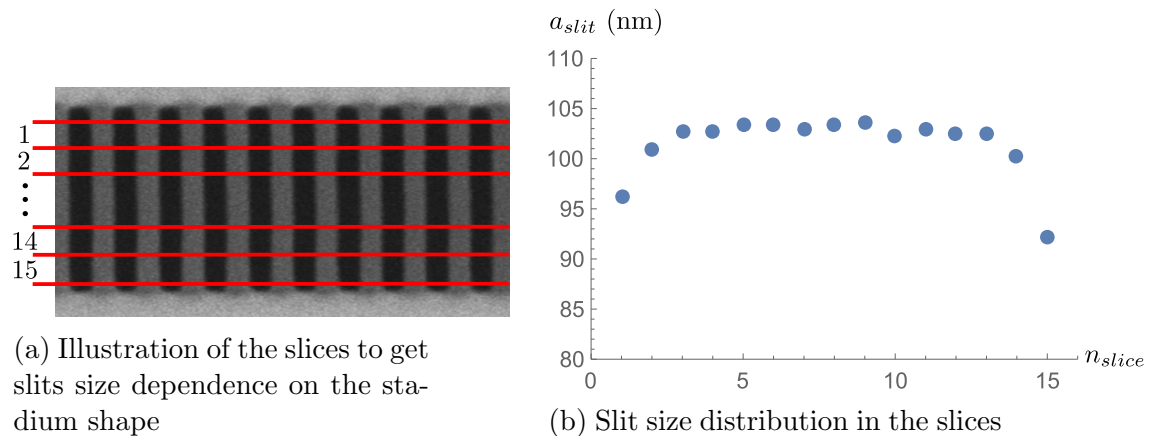
Figure 2.21: study of the slit size dependence on the stadium shape

2.4 Experimental Results

So far we have presented all elements of the experimental setup. Here we present two experimental results obtained for two different velocity ranges. In both cases the velocity has been measured by the technique presented in section 2.1.6.1. In order to increase the signal, the selection in TOF is 1 ms centered around the TOF at which the velocity has been measured. The pushing time was the same for both experiments. The opening of the nanograting along the diffraction axis was $L_g = 306 \pm 3$ μm (following figure 2.6 notation).

2.4.1 Faster beam $v_{prop} = 26.2$ m/s

In the experimental data presented figure 2.22, the propagation velocities of the TOF selected atoms are $v \in [25.5; 26.9]$m/s. For a total number of 150 128 detected events, the total recording time is about 13 hours.
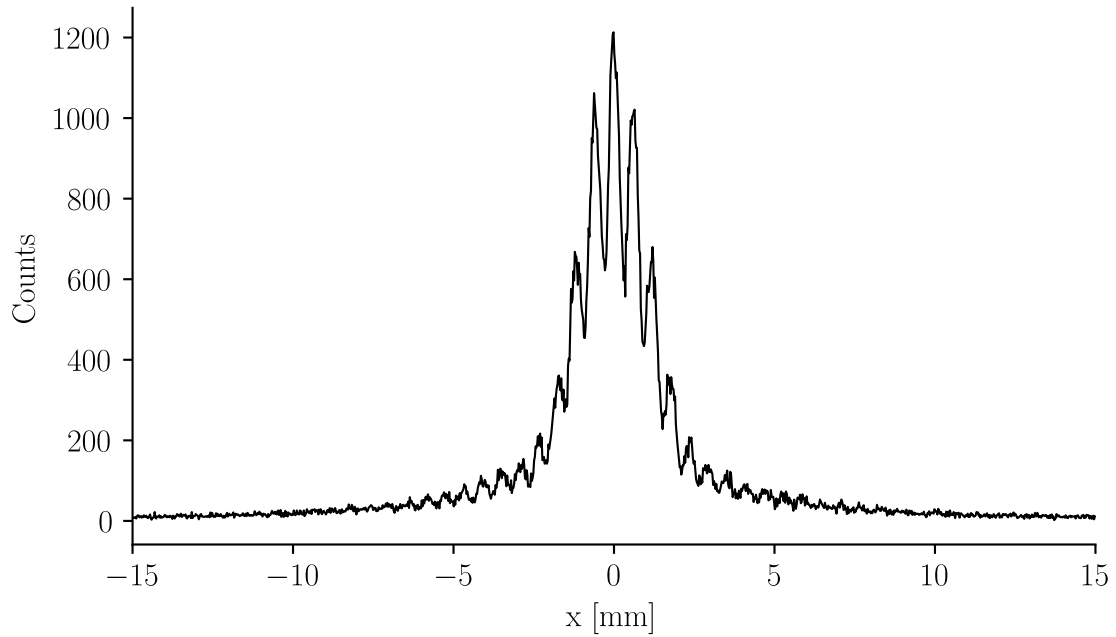
Figure 2.22: Experimental result for atoms propagating at $v \in [25.5; 26.9]$m/s

2.4.2 Slower beam $v_{prop} = 19.1$ m/s

The experimental data figure 2.23 correspond to propagation velocities $v \in [18.7; 19.5]$m/s. The total number of detected events is 99 451, for a total recording time of about 40 hours.
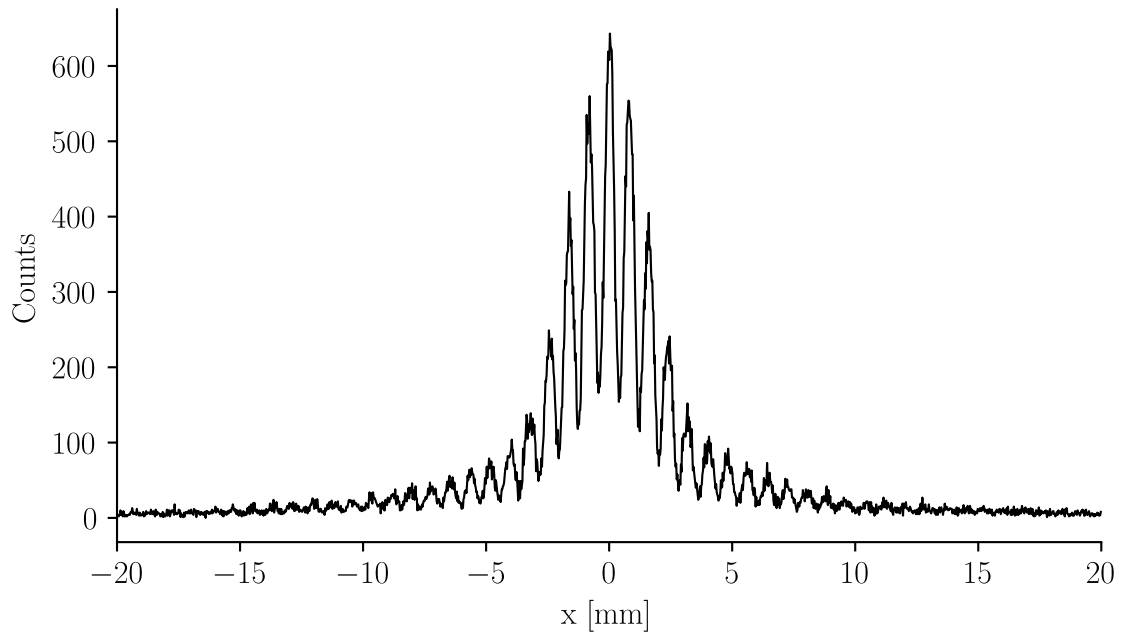
Figure 2.23: Experimental result for atoms propagating at $v \in [18.7; 19.5]$m/s

2.5   Experimental setup summary

1. We have a velocity-tunable pulsed beam of Ar* atoms. The velocity is measured with an accuracy better than the percent.

2. The geometry of the nanograting has been characterized from SEM images. It has a period $p_g = 200.0$ nm, a total depth of 100 nm (80 nm straight + 20 nm rounded), a slit size of $a_{slit} = 102.7$ nm. Moreover, the slits have a stadium shape, and we characterized $a_{slit} \in [92.1; 102.7]$ nm

3. The position of the nanograting can be precisely adjusted in all directions using a hexapod from SmarAct company.

4. The atomic beam is selected using a thick metallic slit. The opening length of the grating in the direction orthogonal to the atomic beam propagation is: $L_g = 306 \pm 3$ μm

5. The grating-detector distance is obtained from the interfringe and de Broglie wavelength of the velocity selected atoms. The distance from the grating to the detector is: $D_{gd} = 307.0$ mm

6. Spatial distortions of the detector have been observed and corrected.

7. The detector has a spatial resolution of 150 μm and a time resolution of 2 ns. This detector enables us to detect single atoms arriving position.

Chapter 3

Semi-Classical model

In the previous chapter, we reviewed the experimental setup and finished the chapter showing two experimental interference patterns.

In this chapter, we will present a wise semi-classical model used in similar experimental situations, which has already been presented inter alia in [12]. This model will be compared to the experimental results. To do so, we present a user friendly form of the atom-surface potential which enables us to take into account retarded effects. Finally, we will see that regarding the experimental data, and the characterized geometry of the nanograting, we have to introduce retarded effects in order to retrieve the Lifshitz atom-surface interaction coefficient.

3.1   The model

To give an overview of the model, the wave function diffracted by the nanograting on the detector is given by Fraunhofer's far-field diffraction formula. The atom-surface interactions are taken into account by introducing an additional phase. This means that we add an additional phase to the wave at each point of the aperture (i.e, the exit of the slit) figure 3.1. The additional phase is given by the action variation along the classical trajectories for atoms propagating in the slit. This justifies calling this model *semi-classical.*

First of all, without considering the atom-surface potential, we can justify the use of Fraunhofer's diffraction formula regarding the geometries and velocities involved in our experiment. In our experiment, the distance from the grating to the detector is $D_{gd} = 307.0$ mm, the average slit size of the grating is $a_{slit} = 102.7$ nm, and
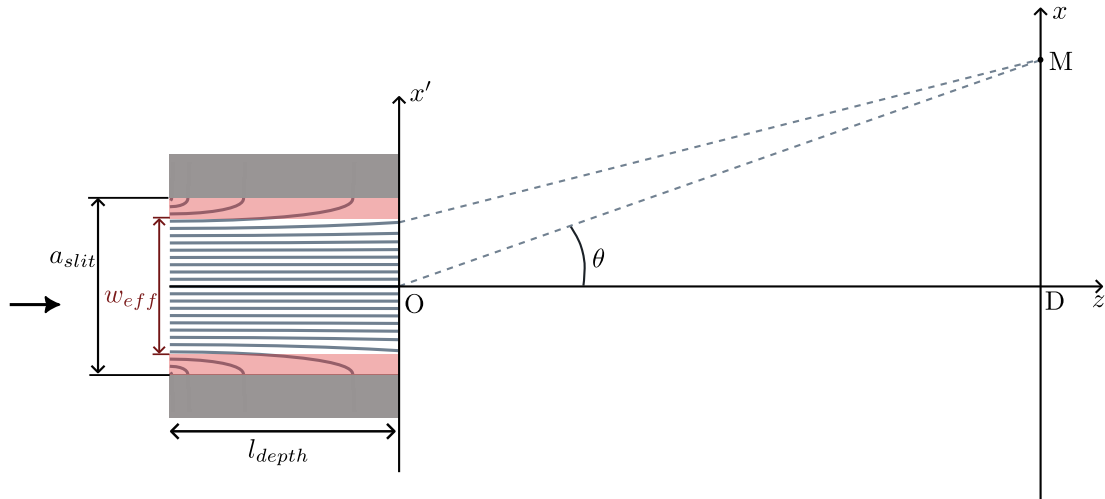
Figure 3.1: Schematic representation of the semi-classical model, for an atom propagating along the z-axis with velocity $v_z = 26.2$ m/s

$\lambda_{dB} = 0.38$ nm at 26.2 m/s ($\lambda_{dB} = 0.52$ nm at 19.1 m/s), the Fresnel number

$$\mathcal{F} = \frac{a_{slit}^2}{\lambda_{dB} D_{gd}}, \tag{3.1}$$

is $\mathcal{F} \approx 9.0 \times 10^{-5}$ at 26.2 m/s ($\mathcal{F} \approx 6.6 \times 10^{-5}$ at 19.1 m/s). Hence, for both velocity ranges, we have $\mathcal{F} \ll 10^{-3}$, which validates the use of Fraunhofer's far-field diffraction formula.

Before defining the additional phase due to the atom-surface potential, we have to introduce the notion of "effective slit".

3.1.1 Effective slit : w_{eff}

If we look at the classical trajectories, as illustrated in the slit figure 3.1, we can see that if an atom enters the slit too close to a wall, it will hit the wall, loose its metastability, and therefore, won't be detected. This phenomenon is taken into account through the effective slit w_{eff}, which has already been introduced in [12], and is shown in pale red in figure 3.1. It appears that the slit aperture becomes smaller due to the atom-surface interactions. As can be seen from equation (3.1), this helps to ensure that we can apply the Fraunhofer diffraction formula, since it is equivalent to reducing a_{slit}. The effective slit is:

- $w_{eff} = 70.3$ nm, at 19.1 m/s.
- $w_{eff} = 74.3$ nm, at 26.2 m/s.

3.1.2 Additional phase : ϕ_{AS}

The atom-surface interactions are taken into account via an additional phase ϕ_{AS}. This phase corresponds to the classical action ($S = \int \mathcal{L} \, dt$) variation of the atom along a classical trajectory.

From the remaining trajectories (trajectories that lead to exit the slit) plotted in figure 3.1, we see that these trajectories are nearly parallel to the z-axis. Indeed, at 26 m/s the difference between the trajectories and the parallel is about 1% only for trajectories at 0.1 nm from effective zones (red pale in figure 3.1).This is due to the high kinetic energy of the atoms compared to the potential energy inside the effective slit w_{eff}.

Therefore, we assume, as it has been done in ref [23], [12], that the classical trajectories are rectilinear, parallel to the z-axis, so the action variation is given by the difference of classical actions along a straight line. Hence, the additional phase is

$$\phi_{AS}(x') = \frac{1}{\hbar} \int_{t_1}^{t_2} dt \, (\frac{1}{2}mv^2 - V_{AS}) - \frac{1}{\hbar} \int_{t_1}^{t_2} dt \, \frac{1}{2}mv^2$$

$$\approx -\frac{1}{\hbar v} \int_{l_{depth}} dz \, V_{AS}(x', \mathrm{z}). \tag{3.2}$$

Where v is the propagation velocity of the atom, V_{AS} the atom-surface interaction potential, and x' a given position inside the slit.

Since we integrate over a straight line, this approximation is often used in potential scattering and is called *eikonal approximation*. This is a reference to the eikonal equation in optics, which links wave optics to geometrical optics, where light propagates along straight rays [24], [25].

3.1.3 Diffraction Pattern

The diffracted pattern is given by Fraunhofer's diffraction formula, the plane wave emitted by each point x' has an additional phase ϕ_{AS} due to the atom-surface interactions. Finally, the square modulus of the diffracted wave function on the detector is given by

$$|\psi(\theta)|^2 = \left| \sum_{slits} \int_{w_{eff}} dx' \, e^{-ikx'sin(\theta)+i\phi_{AS}(x')} e^{\left(-\frac{x'^2}{2\sigma_{coh}^2}\right)} \right|^2, \tag{3.3}$$

where θ is the diffraction angle. The factor $\exp\left(-\frac{x^2}{2\sigma_{coh}^2}\right)$ is a Gaussian weight to take into account the coherence of the extended source with $\sigma_{coh} = L_c/2$ and $L_c = \lambda_{dB}L_g/a_{src}$, the transverse coherence length given by the van Cittert-Zernike theorem [26] where a_{src} is the size of the source. The wave function equation (3.3) should not be regarded as the diffracted wave function for a single atom, due to the Gaussian factor. It is an effective wave function which takes into account the spatial extension of the source. Taking the different experimental parameter (see section 2.5), $L_c = 560 \pm 45$ nm at 19.1 m/s (380 ± 30 nm at 26.2 m/s). We only consider spatial coherence, since regarding the time of flight selection in the experimental data section 2.4, we can consider the source as quasi-monochromatic.

Thus, the diffracted pattern should have exhibited interferences with good visibility since $p_g = 200.0$ nm. The visibility loss in the measured diffracted patterns comes from both the open length $L_g = 306$ μm (see figure 2.6) of the nanograting, and the spatial extension of the source. So we have to take into account the implied angular beam distribution that fits a Gaussian function with standard deviation $\sigma_{beam} = 0.230$ mrad. This is done by taking the convolution product between the angular beam distribution and the diffracted wave function, see figure 4.15.

This approach using an effective wave function is not the most refined and will be reconsidered in chapter 4.

3.1.4   Atom-Surface interactions

The calculation of the Casimir-Polder potential is based on a relatively heavy numerical calculation, and for convenience, we look for a user-friendly form of the atom-surface potential. Hence, we have to make approximations in accordance with our experimental setup, those approximations are listed hereafter.

1 - *The surfaces of walls in a slit are considered as infinite walls.*

This assumption is based on the dimension of the slits of the nanograting, which guarantees that the atoms are close to the walls. It is less and less correct as either we increase the atom-surface distance, or we reduce the depth of the slit for a given depth, see figure 3.2.
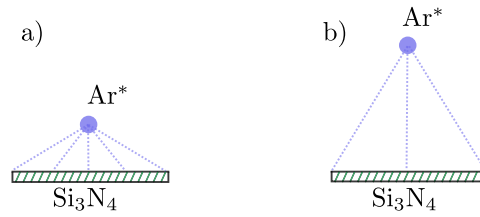
Figure 3.2: a) the atom is sufficiently close to the wall to consider the latter as infinite. b) the atom is too far from the wall which can not be considered as infinite anymore.

2 - *Inside the slit, the interaction potential between an atom and the two walls is considered as the sum of interaction potential between an atom and two single walls.*

This is justified by neglecting multiple images. As illustrated figure 3.3, the atom (considered as a dipole) interacts with its image I_1. This image dipole I_1 has an image dipole I_2 in the opposite wall. This second image dipole also interacts with the atom. Since the distance between the second image I_2 and the atom is much larger than between I_1 and the atom, its influence will be neglected.
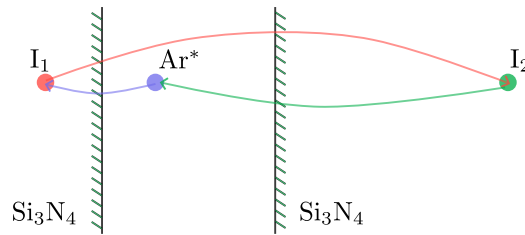
Figure 3.3: Multiple images. The atom induces its image dipole I_1. The image dipole I_1 generates its image in the opposite wall I_2, which also interacts with the atom.

3 - *Surface roughness is not taken into account.*

By means of the effective slit, we do not keep atoms which propagate too close to the surface, then atoms which exit the slit should have propagated at distances of about 10 nm from the surface, so we should not be sensitive to the surface roughness.

4 - *No temperature related effects.*

We worked at room temperature $T \lesssim 300$ K, therefore, the thermal energy $k_B T \approx 0.03$ eV (k_B is the Boltzmann constant) is too small compared to the energy associated with the atomic transitions (≈ 1.53 eV at 811.531 nm) involved in the

atom-surface interactions, see [3]. So temperature will be considered as null.

5 - *Internal surfaces are considered flat.*

This last approximation refers to two different geometrical properties of the slits. First, the slit stadium shape figure 2.21, i.e. the shape of the slit in height. Second, the shape of the slit along the propagation axis as illustrated figure 2.18b.

- The stadium form is simplified by considering that $11/15^{th}$ of the final result corresponds to the diffraction by a 102.7 nm slit and $4/15^{th}$ by a 97.5 nm slit, see figure 3.4. This means that the potential at both extremities of the slit is assumed to be the same as in the case of an infinite surface.
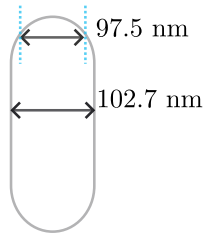
Figure 3.4: Approximation to take into account the stadium shape of the slits.

-The shape of the slit along the propagation axis which is 80 nm straight and 20 nm rounded is approximated as 95 nm straight. This can be justified by looking at the phase ϕ_{AS} along a trajectory in both cases figure 3.5. This approximation is only useful from a numerical point of view, since we have more than 10^4 simulations to run, it is faster when considering a straight slit.
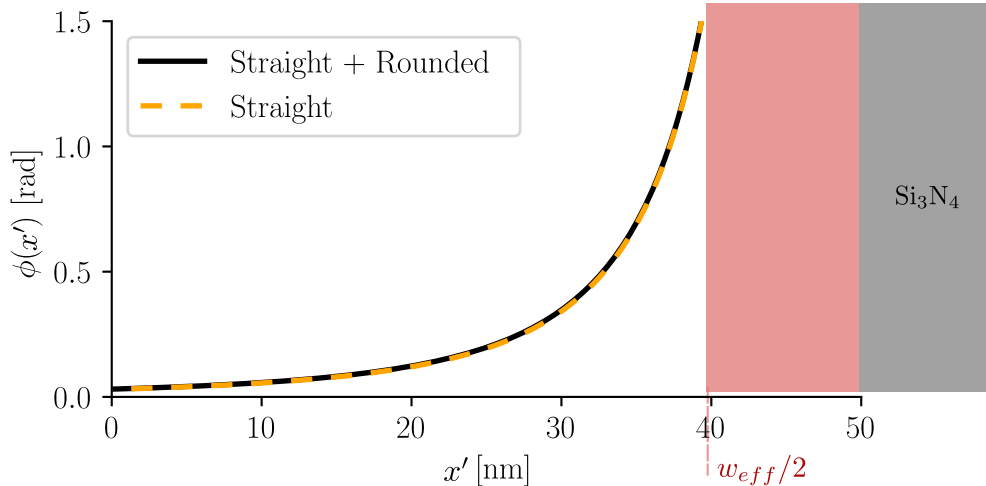
Figure 3.5:   Comparison   of   the   phase   for   a   straight   slit   (orange),   and straight+rounded slit (black), for v=26.2 m/s and C_3=1.25 a.u. The pale red zone represent the effective slit as in figure 3.1.

The potential in the rounded part is calculated using the same potential form as in the case of an infinite wall $-C_3/l^3$, where the atom-surface distance l is changed at position z according to the radius of curvature of the bar.

Therefore in the slit, atoms will interact along the whole depth of the slit, which is considered to be 95 nm, with potential of the form $-C_3/l^3$ in the non retarded regime and $-C_4/l^4$ in the retarded regime, where l is the atom-surface distance and C_3, C_4 are atom-surface interaction coefficients.

3.1.4.1   Atom-Surface interactions : retarded effect

Still looking for a user-friendly form of the atom surface interaction potential, in order to take into account retarded effects, we will write the potential as

$$V(l) = -\frac{C_3}{l^3}.F(l),$$ (3.4)

where the function F should vary from $F(l \to 0) = 1$ to $F(l \to \infty) \propto \frac{1}{l}$, in order to retrieve the two asymptotic behaviors. To write the potential as equation (3.4), we used the potential derived using linear response theory by Wylie and Sipe in [27] [28], which writes in the case of a perfect conductor, and an atom in its ground state:

$$V(l) = -\frac{1}{48\pi^2 l^3} \sum_n \left|d^{0n}\right|^2 \left[l_n + (2 - l_n^2)f(l_n) + 2l_n\,g(l_n)\right]$$ (3.5)

where $l_n = \frac{2\omega_{0n}}{c_0}l$, n refers to the possible excited states connected with electric dipole transition to the initial state.

$|d^{0n}|^2 = |d_x^{0n}|^2 + |d_y^{0n}|^2 + |d_z^{0n}|^2$, with $d_\alpha^{0n} = \langle 0 | D_\alpha | n \rangle$, $\vec{D}$ being the electric dipole operator of the atom.

$f(t) = Ci(t)\sin(t) - [Si(t) - \pi/2]\cos(t)$

$g(t) = -Ci(t)\cos(t) - [Si(t) - \pi/2]\sin(t)$, Si and Ci being the sine and cos integral respectively.

Equation (3.5) is simply the dipolar part of the atom-surface interaction, for an atom considered as a point dipole (no charge distribution) over a short interface (this is ensured by the effective slit). In their articles Wylie and Sipe also mention that they do not take temperature dependence in account, and that they omit the transverse part of the microscopic polarization field.

3.1.4.2 Ar* : Approximations to get a potential of the form $-\frac{C_3}{l^3}F(l)$

For Ar* atoms, the main transition involved in the atom surface interaction is the transition $^3P_2 \rightarrow {}^3D_3$ at 811.531 nm (in air). Actually, there is not only one transition involved in the interaction, the seven first transitions (by importance) have transition $\in$ [696.543, 912.297]nm (in air). Actually, seventeen transitions referenced from the $^3P_2$ state of argon are in the NIST database [29]. Since the main transitions are centered around 811.531 nm, we will make the rather strong assumption that all transitions involved in the bracket of equation (3.5) will have the same frequency dependence, thus $l_n = \frac{2(2\pi)}{\lambda_{opt}}l$. Therefore, under this assumption one can take the bracket out of the sum, and recalling that in the case of the perfect conductor $C_3 = \frac{1}{48\pi\epsilon_0}\sum_n |d^{0n}|^2$ [3], one writes the atom surface interaction potential in the case of the perfect conductor as

$$V_{WS}^{perfect}(l) = -\frac{C_3^{perfect}}{l^3} \cdot \frac{1}{\pi}\left[\xi_{opt}l + (2 - (\xi_{opt}l)^2)f(\xi_{opt}l) + 2(\xi_{opt}l)\ g(\xi_{opt}l)\right], \quad (3.6)$$

where $\xi_{opt} = \frac{2(2\pi)}{\lambda_{opt}}$, λ_{opt}=811.531 nm. Thus, we define

$$F(l) = \frac{1}{\pi}\left[\xi_{opt}l + (2 - (\xi_{opt}l)^2)f(\xi_{opt}l) + 2(\xi_{opt}l)\ g(\xi_{opt}l)\right]. \quad (3.7)$$

The function equation (3.7) is plotted figure 3.6, the blue dashed lines indicate the effective atom-surface distance in the slit. We see from this plot that when considering retardation effects, the atom-surface interaction is reduced by $\approx 15\%$ in average.
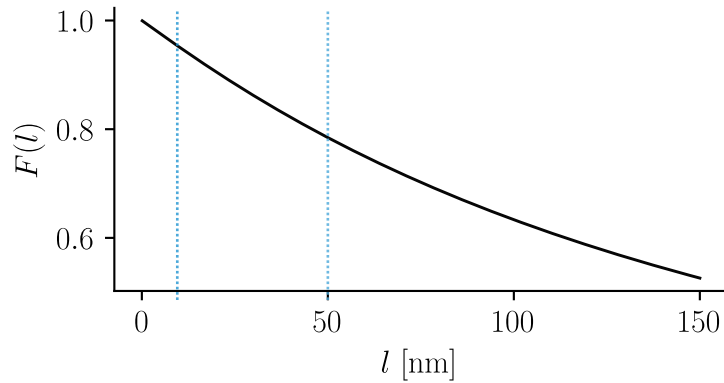
Figure 3.6: Function which takes into account the retardation effects

To verify the assumptions we made so far we can plot the potential (3.6) and the asymptotic behaviors, see figure 3.7
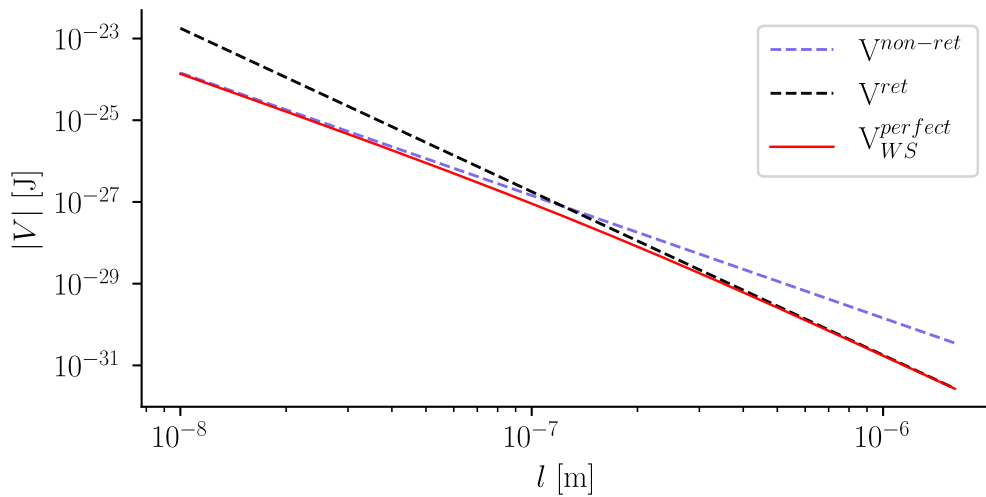
Figure 3.7: Perfect conductor - Log log plot of the absolute value of the potentials with respect to the distance to the surface, the non-retarded regime (black dashed), the retarded regime (blue dashed), the red line corresponds to the potential equation (3.6)

We see from figure 3.7 that in the case of a perfect conducting surface, by making use of the potential (3.6) we retrieve the asymptotic behaviors for the non retarded and retarded regimes.

In our experiment, the nanograting is made of silicon nitride, which is a dielectric. We still assume that we can use the potential equation (3.6), but we replace $C_3^{perfect}$ by $C_3^{Si_3N_4}$, the result and the asymptotic behavior of atom-surface interactions in the case of a dielectric surface are plotted figure 3.8.
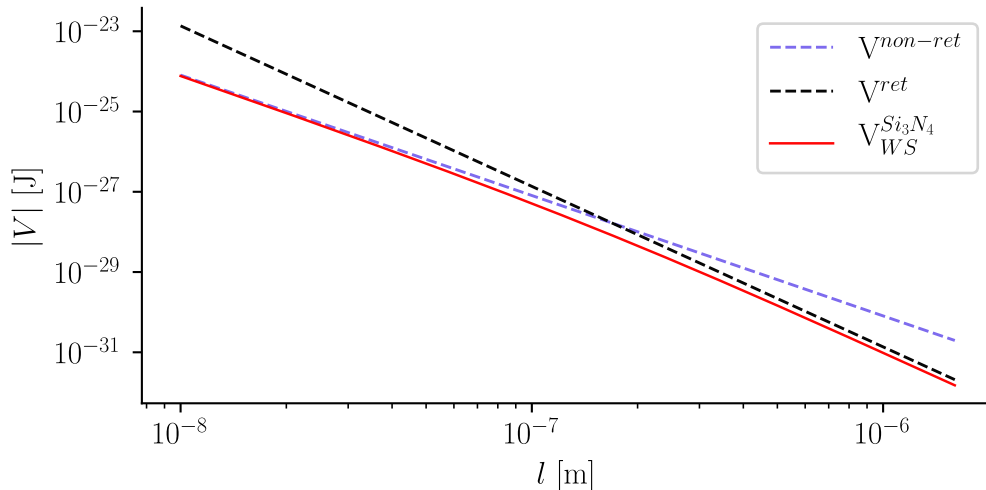
Figure 3.8: Dielectric (Si_3N_4) - Log log plot of the absolute value of the potentials with respect to the distance to the surface, the non-retarded regime (black dashed), the retarded regime (blue dashed), the red line corresponds to the potential equation (3.6)replacing $C_3^{perfect}$ by $C_3^{Si_3N_4}$.

We see in figure 3.8 that there is a worse agreement in the retarded regime between the potential we derived and the retarded asymptotic behavior. This could be due to the optical index of silicon nitride in the UV. However, since we have atom surface distances lower than 51 nm, the discrepancy between the potential (3.6) and the retarded regime will be negligible.

In the following, we will refer to the potential equation (3.6) as *Wylie and Sipe potential* since it derives from the Wylie and Sipe expression (3.5).

Note : All atom surface interaction coefficients, i.e C_3 and C_4, are given with their derivation for both the perfect conductor and dielectric (Si_3N_4) cases in appendix A.

3.2 Comparison to Experimental results

In the following we do not explicitly measure atom surface interactions as a goal, but we probe the need to take into account retardation effects to describe our experimental data, where the atom surface distances are ≤ 51 nm. To do so, we compare two models of the atom-surface interaction potential with respect to the data at 26 m/s (see figure 2.22). In the first model, we will take the non-retarded atom-surface interaction potential.

$$V_{non\ ret}(l) = -\frac{C_3}{l^3},$$
(3.8)

while in the second model we do take into account retardation effect by using the potential,

$$V_{WS}(l) = -\frac{C_3}{l^3} . F(l), \tag{3.9}$$

where F is given by equation (3.7).

Actually, the potentials we use in the simulations take into account the two walls of the slit, see page 40, item 2.

3.2.1 χ^2-Neymann

To compare both models of the atom-surface interaction potentials (non-retarded and retarded), we make use of the Neymann's χ^2

$$\chi^2 = \sum_{\theta} \frac{(I_\theta^{exp} - I_\theta^{theo})^2}{\sigma_\theta^2}, \tag{3.10}$$

where σ_θ is the signal noise standard deviation, taken as the square root of the number of detected events at angle θ. I_θ^{exp} and I_θ^{theo} are the experimental and theoretical number of detected events at angle θ.

The parameters can be classified into two categories. The first category corresponds to the two theoretical parameters, the atom surface interaction coefficient C_3 and the maximum phase shift ϕ^{max}. ϕ is the additional phase shift that carries the atom-surface interactions, see equation (3.2). The maximum phase shift is considered as a parameter, it is equivalent to varying the effective slit size w_{eff} (and thus the minimum atom-surface distance l_{min}), see figure 3.5.

The second category corresponds to the experimental parameters, e.g. the velocity distribution, the geometry of the nanograting, the angular beam distribution, etc. The experimental parameters are considered as fixed and have been constrained by means of external techniques.

For both theoretical models, we look for the parameters (C_3 and ϕ^{max}) which minimize the χ^2 (3.10). We first let the parameters vary over a wide range of values. The result is plotted in figure 3.9. Surfaces correspond to $\chi^2_{min} + 40\sigma$, where $\sigma = 6.2$ is the standard deviation for a χ^2-distribution with two parameters [30]. This is not entirely appropriate here, as we shall see in chapter 5.

We observe multiple local χ^2 minima for different maximum phase shifts. These local minima lead to a minimum atom-surface distance of $l_{min} \approx 17.5, 13.1, 11.0, 10.1$ nm, respectively. The global minimum corresponds to $\phi^{max} = 10.5$ rad ($\Leftrightarrow l_{min} =$

13.1 nm). This is in agreement with the expected minimum atom-surface distance from classical trajectories figure 3.1.
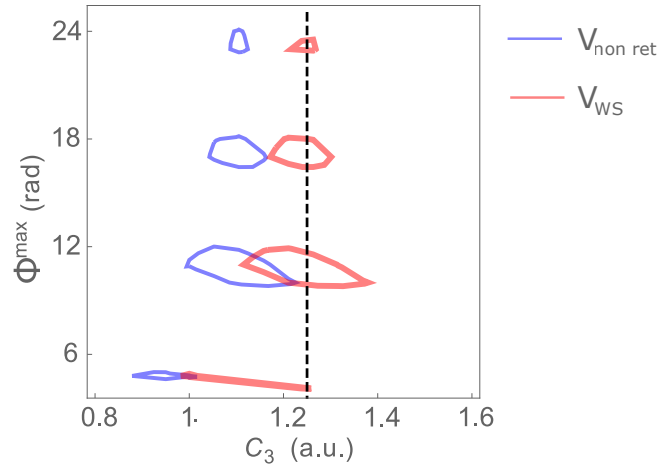
Figure 3.9: $\chi^2_{min} + 40\sigma$ surfaces for both models, non retarded (blue) and retarded (red). The dashed line shows the theoretical expected value for $C_3^{Si_3N_4}$

The dashed black lines in figure 3.9 and figure 3.10, indicate the expected C_3 value for ${}^3P_2$ Ar* interacting with a Si_3N_4 surface one gets from Lifshitz's formula, see appendix A.

Figure 3.10 is an enlargement of figure 3.9, the surfaces corresponds to $\chi^2_{min} + n\sigma$, $n = 1, 3, 6, 9$. We see that there are more than 30σ between the expected C_3 (dashed black) and the best fit (blue surfaces) when neglecting retarded effects.

Moreover, we retrieve a 15% difference between the retarded and non-retarded models as expected from figure 3.6.
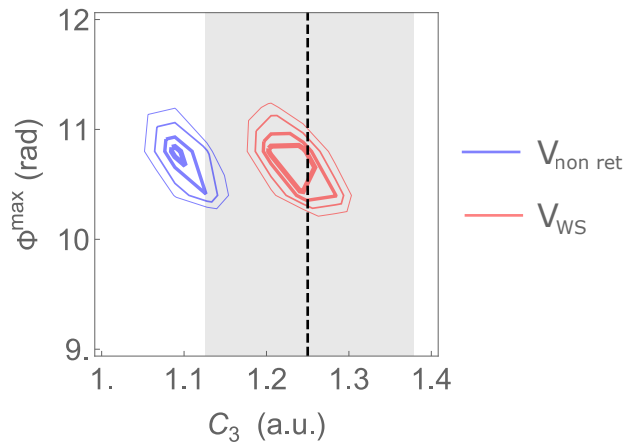
Figure 3.10: $\chi^2_{min} + n\sigma$ ($n = 1, 3, 6, 9$) surfaces for both model. The black dashed line represent the expected value for Ar* atom in front of Si$_3$N$_4$. The gray area represent the 10% uncertainty on the expected value.

Both models have similar values of χ^2_{min}, so neither case indicates a better model. We do not give the value of χ^2_{min} since here it would be a mistake to interpret it in terms of goodness-of-fit test or as qualifying how close the models are to the data, as will be discussed in chapter 5.

The best fit obtained when taking retarded effect into account is plotted figure 3.11.
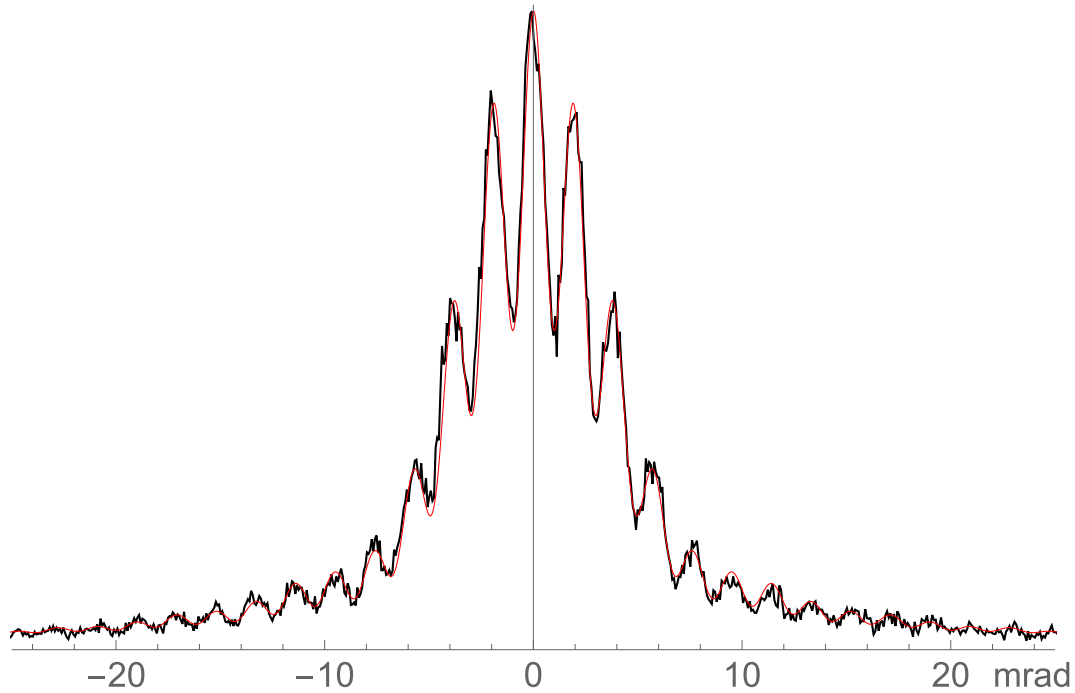
Figure 3.11: data at 26m/s (black), with the best fit using the Wylie and Sipe potential (red).

This result supports what was already mentioned by E. A. Hinds and V. Sandoghdar in [31], where the authors indicated that the non retarded potential in the case of a two level atom near a metallic surface, "is correct at distances less than 0.12λ". Actually, in our case, 51 nm corresponds to 0.06λ, but we work with a multilevel atom in front of a dielectric. To conclude, one should keep in mind that

One has to take into account retarded effects when atom-surface (or dipole-dipole) distance is a non-negligible fraction of the predominantly contributing optical wavelength.

Influence of the fixed parameters :
If we now allow the geometry of the nanograting to vary. We can enlarge the diffraction pattern either by reducing the slit size or increasing the atom-surface

interactions. The same reasoning holds for the depth of the slit. Therefore, it is of critical importance to have a precise characterization of the geometry of the nanograting. By making use of the semi-classical model, we found that

$$
\begin{cases}
\Delta a_{slit} = \pm 1 \text{ nm} \Rightarrow \Delta C_3 = \pm 0.07 \text{ a.u} \\
\Delta l_{depth} = \pm 10 \text{ nm} \Rightarrow \Delta C_3 = \pm 0.16 \text{ a.u}
\end{cases}
\tag{3.11}
$$

3.2.2 Discussion of the expected C_3 value

The main problem when calculating the atom-surface interaction coefficient when we use the Lifshitz formula, is that we need the optical properties of the material for $\omega = 0 \rightarrow \infty$.

There are not many optical measurements for wavelengths smaller than 190 nm for Si_3N_4. The only measurements that exist dates from 1973. Another major problem comes from the change in optical properties of amorphous Si_3N_4 depending on the manufacturing process. For example, to manufacture Si_3N_4 membrane, there are two main techniques. The low pressure chemical vapor deposition (LPCVD) (used for the membrane for our nanogratings), and plasma enhanced chemical vapor deposition (PECVD). The pressure and flow used will influence the optical properties of the final product. For more information, see [32]. The optical properties also depend on the geometry of the sample used, e.g. its width.

For the optical data from [33], the Si_3N_4 membrane was obtain from process close to the one used for our membrane.

In light of what we just said, the safest thing to do for future experiments is to characterize the optical properties of the nanograting we used or a sample obtained from the same fabrication process. It would also be of great interest to get the optical properties for wavelengths smaller than 190 nm, since it has not been done from a long time and that the Ar* atoms have transitions in the UV.

3.2.3 Limitations of the semi-classical model

In the previous section we compared the semi-classical model to the data at 26.2m/s, but not with the data at 19.1 m/s. Indeed, at 19.1 m/s, the eikonal approximation (section 3.1.2) no longer holds. Thus it is not possible to reproduce enough the data at 19.1 m/s with the semi-classical model presented so far. What should be done is to calculate the action variation along a classical trajectory which can not

be considered as a straight line anymore, or develop a model based on another approach.

We were considering either improving the semi-classical model or developing a model based on numerical resolution of the time-dependent Schrödinger equation. One main reason to develop a full QM model is that the semi-classical model can not take into account purely quantum effects such as quantum reflection, i.e reflection of matter wave on an attractive potential. Since we are interested in decreasing the atom propagation velocity, and that transverse atom velocity (atom velocity in the direction of the walls) is low, quantum reflection might occur. Therefore we decided to develop a model based on the time dependent Schrödinger equation, the next chapter is dedicated to this model.

3.3   Semi-classical model summary

1. The diffraction pattern is obtained by propagating the wave function at the exit of the slit using the far field Fraunhofer's diffraction equation.

2. Atom-surface interactions are taken into account by adding a phase to the wave function at the exit of the slit.

3. Ar* which hit the surface loose their metastability, thus they won't be detected, this is taken into account by considering a reduced effective slit.

4. The additional phase due to atom-surface interactions in the eikonal approximation is equal to the classical action variation along a straight line parallel to the propagation axis.

5. In the slit, atom-surface interaction potential is assumed to be of the same form as in the case of one atom in front of an infinite surface.

6. We use a potential form derived from the analytic expression given by Wylie and Sipe, this enables us to easily consider retarded effect.

7. Comparing the semi-classical model to the experimental data at 26.2 m/s proves the need to take into account retarded effect even if in the experiment atom-surface distances are $\lesssim 51$ nm.

8. Eikonal approximation does not hold while considering the experimental data at 19.1 m/s.

Chapter 4

1D time-dependent Schrödinger equation model

In this chapter, we present a new approach to model our experiment. This new approach is based on the time-dependent Schrödinger equation. It has been developed in collaboration with Dr. Naceur Gaaloul and Pr. Eric Charron.

2D simulations are computationally expensive due to the spatial resolution requirement to accurately represent the atom surface interaction potentials. We therefore provide a 1D model in which we look at the evolution of the transverse wave function of an atom in its reference frame. Using this 1D model, we test the simulation parameters (i.e. space and time resolution) required such that the result converges.

The results of the 1D simulations are discussed and superimposed on the experimental results. We then review some theoretical predictions made with the simulation, to guide future experimental developments. Systematic uncertainties related to the geometry of the nanograting are discussed with the help of the simulation. Finally, we recall the main limitations of our 1D approach, as well as the difficulties associated with a 2D simulation.

4.1   Numerical method : Split Operator

To numerically solve the time-dependent Schrodinger equation, we use the *Split Operator Method*. The SPO has been proposed by Feit et al. in 1982 [34]. It is a spectral method which relies on the decomposition of the evolution operator $U(t', t)$. This operator, when applied to the quantum state at time t, returns the quantum

state at time t',

$$\widehat{U}(t + dt, t) = e^{-\frac{i}{\hbar}\widehat{H}dt},$$

$$\psi(x, t + dt) = \widehat{U}(t + dt, t)\psi(x, t),$$

(4.1)

where $\widehat{H} = \widehat{T} + \widehat{V}$ is the time independent Hamiltonian operator, $\widehat{T}$ the kinetic operator and $\widehat{V}$ the potential operator. The evolution operator is then decomposed as follows:

$$\widehat{U}(t + dt, t) = e^{-\frac{i}{\hbar}\frac{\widehat{T}}{2}dt}e^{-\frac{i}{\hbar}\widehat{V}dt}e^{-\frac{i}{\hbar}\frac{\widehat{T}}{2}dt} + O(dt^3).$$

(4.2)

The potential and the kinetic operators are diagonal in the position and momentum space respectively. Thus, applying the potential operator simply corresponds to multiplying the wave function by $\exp\left(-\frac{i}{\hbar}\widehat{V}dt\right)$, while applying the kinetic operator corresponds to multiplying the Fourier transform of the wave function by $\exp\left(-\frac{i}{\hbar}\frac{\widehat{T}}{2}dt\right)$.

Therefore, making use of Fourier transform, it is easy to apply the approximate evolution operator equation (4.2). Note that since the SPO method relies on the use of Fourier transform, it is categorized as a spectral method.

In numerical method, one can use the Fast Fourier Transform (FFT) algorithm to get the Fourier transform. For a review of three different numerical methods for the time-dependent Schrödinger equation, including the SPO, see [35].

The scheme of the SPO method to propagate the wave function from time t to $t + dt$ is illustrated figure 4.1, so we simply have to repeat this sequence until the wave function has been propagated to the final desired time. Using this method, it is also possible to use a time-dependent potential.

$$\psi(x, t) \xrightarrow{\text{FFT}} \boxed{\times e^{-\frac{i}{\hbar}\frac{\widehat{T}}{2}dt}} \xrightarrow{\text{iFFT}} \boxed{\times e^{-\frac{i}{\hbar}\widehat{V}dt}} \xrightarrow{\text{FFT}} \boxed{\times e^{-\frac{i}{\hbar}\frac{\widehat{T}}{2}dt}} \xrightarrow{\text{iFFT}} \psi(x, t + dt)$$
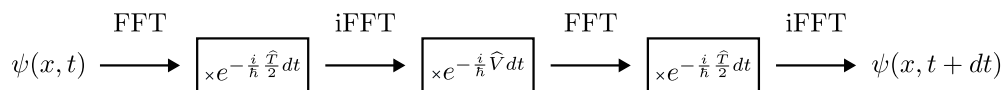
Figure 4.1: Illustration of the implementation of the split operator method

4.1.1 Space and time grids

In the case of a 1D problem, the space grid is defined by the number of grid points and the desired length to be represented. This also defines the spatial resolution of the grid,

$$dx = \frac{L}{ngpx},$$

(4.3)

with L the total length of the grid and $ngpx$ the number of grid points. Since the SPO method relies on FFTs, the spatial resolution defines the maximum energy E_{grid} that can be represented in the numerical simulation. The maximum energy is given in [36] and writes

$$E_{grid} = \frac{p_{grid}^2}{2m} = \frac{h^2}{8mdx^2}. \tag{4.4}$$

In the simulation, the spatial resolution will have to be chosen such that the total energy (kinetic+potential) of the physical problem is smaller than E_{grid}.

For the time resolution dt, following [36], one should choose dt such that $\epsilon = h/(2dt)$ is larger than the maximum energy change which is induced by the time-dependent process. Actually, one often chooses dt as one thousandth of the total time of propagation. This is not a general rule, and one should always verify that the simulation converges. For example, for both the spatial and time resolutions, we should verify that the result is unchanged while reducing the spatial and time resolutions by two,

$$\begin{cases} dx \to \frac{dx}{2} \\ dt \to \frac{dt}{2} \end{cases} \tag{4.5}$$

The convergence test (4.5) has to be performed until the result does not change anymore, this gives us the spatial and temporal resolutions we need to simulate our problem. We apply this to our simulation in section 4.2.3.5.

4.2 1D approach

Here, we present the 1D approach which is illustrated in figure 4.2. The wave function associated to an atom arriving on the nanograting is considered as a plane wave, as justified in section 4.2.1. Because the problem of the diffraction by a N slit grating can be reduced to the diffraction by one slit (see section 4.2.2 & appendix B), we only need to simulate the propagation inside one slit. We make two main assumptions, first, the atom-surface interaction potential is non-null only inside the slit. Second we assume that the wave function arriving on the slit takes the form of the slit.

When an atom hits the surface it looses its metastability, and so it is not detected, this is taken into account by absorbing the wave function at the surfaces. The 1D simulation starts by considering a rectangular wave function (same size as the slit),

then this wave function evolves during $t = l_{depth}/v$ (with v the atomic propagation velocity and l_{depth} the depth of the nanograting) in the atom-surface potential and is absorbed at the surfaces of the bars of the nanograting. The wave function outgoing the slit is (freely) propagated analytically to the detector.

The novelty of the simulation presented here is to take into account both the atom-surface interaction potential and absorbing boundary conditions inside the slit.
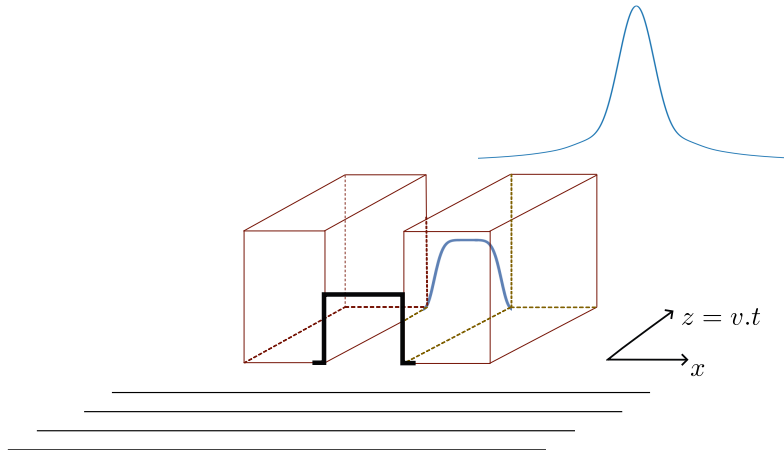
Figure 4.2: Representation of the 1D simulation principle.

4.2.1   Source model

To model the source we will use the same approach as proposed in [37]. The thermal cloud is considered as a collection of non-interacting Gaussian wave packets as illustrated in figure 4.3. The velocity distribution of an atom in the thermal cloud follows a Maxwell-Boltzmann distribution.
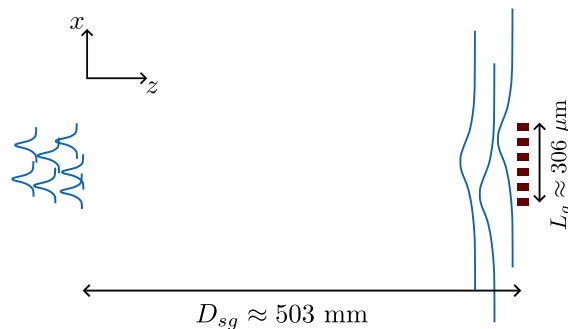
Figure 4.3: The source of atoms is represented by a collection of Gaussian wave packets, these wave packets freely propagate to the nanograting.

The momentum distribution for an atom in the source is given by

$$|\psi(p)|^2 \propto e^{-\frac{p^2}{2\sigma_p^2}}, \tag{4.6}$$

where $\sigma_p = \sqrt{k_B T m}$, and $p = \hbar k$. The wave function associated to an atom in the source $(t = 0)$ is

$$\Psi(x,0) = \frac{1}{\sqrt{2\pi}} \int dk e^{-\frac{p^2}{4\sigma_p^2}} e^{ik.x}. \tag{4.7}$$

Thus, the initial wave function associated to an atom of the source is given by :

$$\Psi(x,0) \propto e^{-\frac{2\pi}{\lambda_T^2}.x^2} = e^{-\frac{x^2}{4.\sigma_0^2}}, \tag{4.8}$$

where $\lambda_T = \sqrt{\frac{2\pi\hbar^2}{mk_B T}}$ and $\sigma_0 = \frac{\lambda_T}{2\sqrt{2\pi}}$.
We can verify that this is compatible with Heisenberg relation : $\sigma_0 \, \sigma_p = \frac{\hbar}{2}$.

The MOT has a temperature $T \approx 150 \ \mu$K, so $\lambda_T \approx 223$ nm. For an atom propagation velocity of about $v \approx 19$ m/s in the direction of the nanograting, the atom freely propagates from the source to the nanograting during $t \approx 26$ ms. The standard deviation time evolution, associated to the Gaussian wave function's spreading is

$$\sigma(t) = \sigma_0 \sqrt{1 + \frac{\hbar^2}{4m^2\sigma_0^4}t^2}, \tag{4.9}$$

where $\sigma_0 = \sigma(t = 0)$ is the standard deviation of the initial Gaussian wave function [38].

Hence, when an atom reaches the nanograting, it is represented by a Gaussian wave function $|\Psi(x,t)|^2 \propto e^{-\frac{x^2}{2\sigma(t)^2}}$, with a standard deviation $\sigma(t \approx 26$ ms$) \approx 465 \ \mu$m. The open length of the grating is $L_g \approx 306 \ \mu$m, thus the wave function of an atom covers almost uniformly the entire grating, which justifies that we consider a plane wave as the wave function of an atom incoming on the nanograting.

As in the semi-classical model, the loss of visibility is only due to the angular beam divergence.

4.2.2 Analytical propagation to the detector

The wave function outgoing the slit at time t_e is freely propagated to the detector in the momentum space. In position space, the wave function is then given by the

inverse Fourier transform. So, the wave function reaching the detector at t_d is given by

$$\psi(x, t_d) = \frac{1}{\sqrt{2\pi}} \int_{-\infty}^{+\infty} dk \, \exp\left(-i\frac{\hbar k^2}{2m}(t_d - t_e)\right) \, \tilde{\psi}(k, t_e) \, e^{-ikx}. \tag{4.10}$$

In the stationary phase approximation $t_e \ll t_d$, see [39], equation (4.10) can be written

$$\psi(x, t_d) \approx \sqrt{\frac{m}{\hbar(t_d - t_e)}} \tilde{\psi}\left(-\frac{mx}{\hbar(t_d - t_e)}, t_e\right) \exp\left(i\frac{mx^2}{2\hbar(t_d - t_e)}\right) e^{-i\frac{\pi}{4}} \tag{4.11}$$

This approximation leads to better results for longer propagation time, since the longer the propagation time, the faster the phase oscillates.

The wave function might theoretically tunnel from one slit to another, however, given the thickness of the bars of the nanograting, we neglect any tunneling effect. Thus, we have the same wave function ψ_{1_slit} that exits each slit of the grating, but located at different positions in space. Therefore, one can show (see Appendix B) that in the stationary phase approximation, the wave function diffracted by N slits is given by the wave function diffracted by a single slit multiplied by an analytic function as in classical optics. Therefore, we only need to simulate the propagation of the wave function in a single slit.

In the most general case where the grating can be turned by an angle α_g with respect to the x-axis (see figure 4.2), the square modulus of the wave function diffracted by N slits on the detector is given by

$$|\psi(x, t_d)|^2 \approx |\psi_{1\_slit}(x, t_d)|^2 \frac{\sin^2\left(\frac{mp_g \cos(\alpha_g)}{2\hbar(t_d - t_e)}Nx + \frac{mp_g \sin(\alpha_g)}{4\hbar(t_d - t_e)^2 v}Nx^2\right)}{\sin^2\left(\frac{mp_g \cos(\alpha_g)}{2\hbar(t_d - t_e)}x + \frac{mp_g \sin(\alpha_g)}{4\hbar(t_d - t_e)^2 v}x^2\right)}, \tag{4.12}$$

with p_g the nanograting period. The complete derivation is given in Appendix B. We have taken into account the possibility to add an angle because we observed, in the experiment, an influence of the orientation of the nanograting on the symmetry of the diffracted pattern.

For the specific case where the plane of the grating is orthogonal to the propagation axis ($\alpha_g = 0°$), equation (4.12) reduces to

$$|\psi(x, t_d)|^2 \approx |\psi_{1\_slit}(x, t_d)|^2 \frac{\sin^2\left(\frac{mp_g}{2\hbar(t_d - t_e)}Nx\right)}{\sin^2\left(\frac{mp_g}{2\hbar(t_d - t_e)}x\right)}. \tag{4.13}$$

4.2.3 Propagation in the grating

In this simulation approach, we do not have to artificially introduce the effective slit used in section 3.1.1. However, we still need to take into account the loss of Ar* which hit the surfaces and will not be detected. This is done by absorbing the wave function if it reaches distances lower than a given r_{min} from the surfaces. The absorption of the wave function is described in section 4.2.3.3. We first need to define the minimum distance at which the wave function has to be absorbed.

4.2.3.1 Minimum atom-surface distance : r_{min}

It is important to define the minimum atom-surface distance because it will also affect the size of the slit. A first approach is to consider the Ar* atom regarding its electronic configuration (see section 2.1.1) as a sphere of radius r_{Ar^*}, where r_{Ar^*} is given by the Bohr model using Slater's rule.

In Bohr's model, the energy associated to an atomic level n is given by

$$E_n = -13.6 \text{ eV} \left(\frac{Z^*}{n^*} \right)^2, \tag{4.14}$$

while the radius of the atom is given by

$$R_n = a_0 \frac{(n^*)^2}{Z^*}, \tag{4.15}$$

where a_0 is Bohr radius, n is the principal quantum number, n^* the effective quantum number and $Z^* = Z - \sigma$ is the effective nuclear charge (σ : screening). For Ar* in the electronic configuration of interest, Slater's rules give : $n^* = 3.7$ and $Z^* = 2.05$ ($\sigma = 7\sigma_{3s3p} + 8\sigma_{2s2p} + 2\sigma_{1s}$).

The numerical application leads to $E_4 \approx 11.59$ eV, which is close to the measured [29] energy of the $^3P_2$ energy level of Ar*, $E_4 \approx 11.55$ eV. This validates that we can consider Ar* as a sphere, with radius given by equation (4.15), $r_{Ar^*} \approx 0.35$ nm.

Therefore, in the model, we assume that the wave function has to be absorbed at a distance $r_{min} = 0.35$ nm from the surfaces. The underlying hypotheses being that at distances lower than $r_{min} = r_{Ar^*}$ an overlap occurs between the electron of Ar* atoms and the electrons of the surfaces.

4.2.3.2 Atom-surface potential

To model the atom-surface interactions, we used the Wylie and Sipe potential derived in equation (3.9). We modify it by adding a repulsive part, thus we write it V_{LJ} in reference to the Lennard-Jones potential,

$$V_{LJ}(l) = V_{WS}(l) + \frac{C_6}{l^6}, \tag{4.16}$$

where l is the distance between the atom and the surface, V_{WS} the attractive Wylie and Sipe potential, and C_6 is not the van der Waals coefficient, but a coefficient to get the minimum of the potential equation (4.16) at distances $l = r_{min}$ from the surfaces. C_6 is given by

$$C_6 = \frac{C_3}{2} \, r_{min}^3. \tag{4.17}$$

The atom-surface interaction potential equation (4.16) is plotted in figure 4.4.
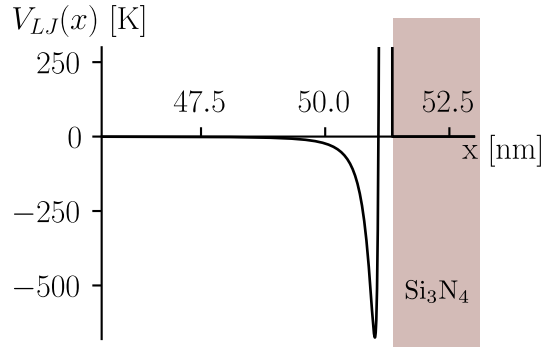
Figure 4.4: Atom-surface interaction potential, the Si_3N_4 surface is represented by the red area, located at 51.35 nm for $a_{slit} = 102.7$ nm.

Actually, we do not directly use the potential of equation (4.16) in the simulation. We will modify a part of the potential only for atom-surface distances lower than r_{min}, this is just a numerical trick to get better absorption results (see next section 4.2.3.3). The modification function is given by equation (4.18) and is plotted in figure 4.5a. The modified atom-surface interaction potential we will use in the simulation is plotted figure 4.5b.

$$f_{modif}(x) = \begin{cases} U_0 \, \cos\left(\frac{\pi}{2} \frac{|x| - \left(\frac{a_{slit}}{2} - r_{min}\right)}{l_{ab} + r_{min}}\right)^2 & \text{if } \frac{a_{slit}}{2} - r_{min} \leq |x| \leq \frac{a_{slit}}{2} + l_{ab} \\ 0 & \text{otherwise} \end{cases} \tag{4.18}$$

with $U_0 = V_{LJ}(\frac{a_{slit}}{2} - r_{min})$, the value of the minimum of the atom-surface potential. l_{ab} is the distance over which the modification function goes from its minimum U_0 to 0.
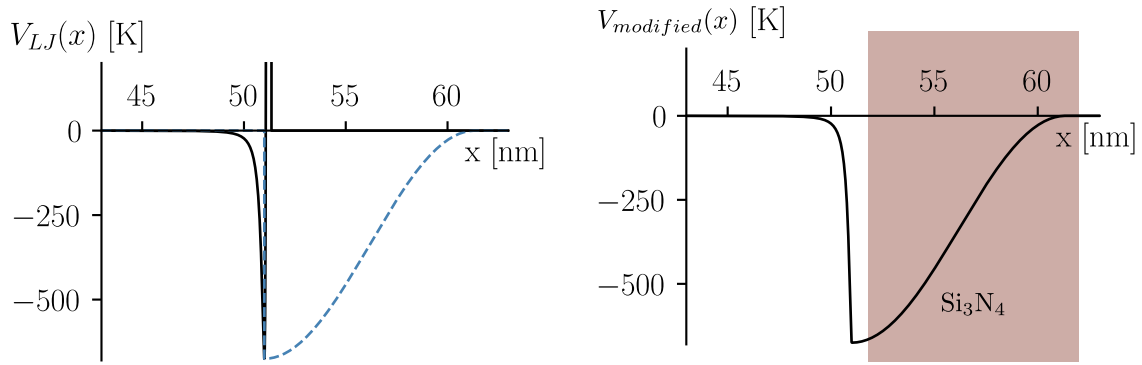
(a) Atom-surface potential (black - solid), and the modification function (blue - dashed)

(b) The modified atom-surface interaction potential. The surface is represented in red.

Figure 4.5: Modification of the atom-surface interaction potential ($a_{slit} = 102.7$ nm).

Finally, the wave function evolves in the potential equation (4.16), and is absorbed in the region represented in blue in figure 4.6. The wave function evolves in the modified part of the potential only on 0.1 nm (see next section 4.2.3.3) on each side, which is negligible with respect to the size of the slit $a_{slit} = 102.7$ nm. Moreover, we did not modify r_{min} nor a_{slit}, to see the impact of the modification of the repulsive part of the potential, but we should look at the proportion of the wave function that is impacted by this modification. This is discussed later in section 4.2.3.6.

Figure 4.6: Modified atom-surface potential (black - solid), the red area represent the surface while the blue area represent the absorption region. $a_{slit} = 102.7$ nm, so the surface is located at 51.35 nm.
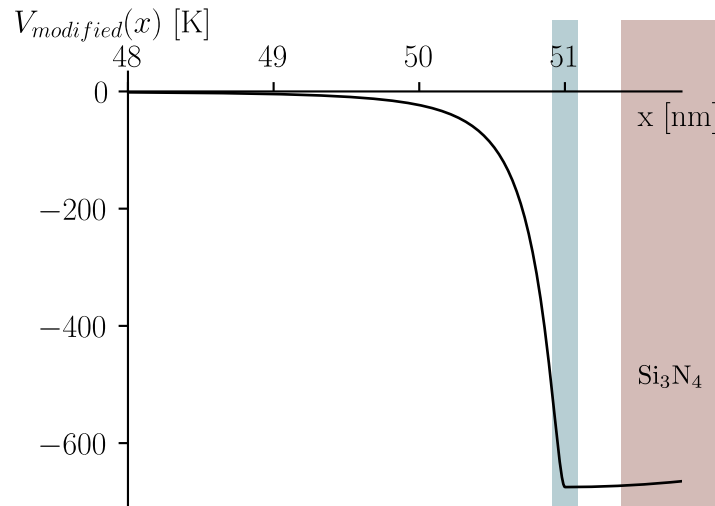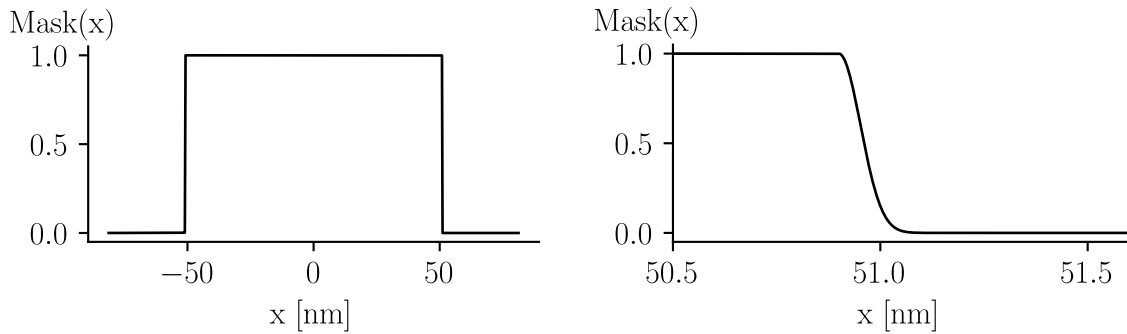
4.2.3.3 Absorption of the wave function

There are different ways of absorbing wave functions in simulations. The most common way is to make use of complex potentials [40] (which is a generalization of pure negative imaginary potentials). But, the main problem of this method is that, it is difficult to parameterize the complex potential to get the desired absorption length and amplitude. The absorption is improved for longer complex potentials, but here we are interested in absorbing the wave function over the shortest distance. Another problem of this method is related to the use of a potential. It means that there is a dependence with the energy of the particle, thus, during the propagation (i.e the time evolution), the absorption does not occur at the same distance to the surface, if we take a constant complex potential. So, the complex absorbing potential has to be modified during the propagation.

An easier way to absorb the wave function is to make use of mask functions. These functions are equal to one in the zone of interest and zero where we want the wave function to be absorbed. Then, we multiply the wave function at each time step of the simulation by the mask function. Actually, one cannot use a function which directly goes from one to zero. Even with the mask function technique, the absorption length is non null (which is also referred to as absorbing zone or area). However it is much easier to parameterize than any complex potential. Using the mask function technique it is also possible to absorb the wave function over very short distances and at constant positions. The mask function we used is

$$
Mask(x) = \begin{cases} 1 & \text{if } |x| < (x_{abs} - d) \\ \cos^{\alpha}\left(\frac{\pi}{4}\left(1 + \frac{|x| - x_{abs}}{d}\right)\right) & \text{if } (x_{abs} - d) \leq |x| \leq (x_{abs} + d) \\ 0 & \text{otherwise} \end{cases} \qquad (4.19)
$$

where x_{abs} is the position at which the wave function is absorbed ($x_{abs} = \frac{a_{slit}}{2} - r_{min}$). The total absorption length is equal to $2d$. α is a parameter to change the slope, often taken to be equal to 2. In our case, we take $\alpha = 12$ since it leads to better absorption results. The function (4.19) is plotted in figure 4.7 for $d = 0.2$ nm and $\alpha = 12$.

We then multiply the wave function by the mask function at the end of each time step, that is, at the end of the propagation scheme of figure 4.1 to perform the absorption. We also use the function (4.19) as the initial wave function since we assume in our model that the wave function takes the form of the slit.

(a) Full plot of the mask function (a_{slit} = 102.7 nm).

(b) Zoom on the edge of the mask function, i.e the absorption area (a_{slit} = 102.7 nm).

Figure 4.7: Mask function used to absorb the wave function.

Note that whatever absorption technique one uses, it will always introduce reflections. These reflections are purely numerical. Therefore, one has to reduce the amplitude of the reflections so that it is negligible with respect to the amplitude of the wave function. To do so, one can change the parameters α, d in equation (4.19) or change the time step dt. This will be discussed in section 4.2.3.5, since it is closely related to the simulation convergence test.

The shape of the wave function in the absorbing areas is affected by the shape of the mask function, see figure 4.7b. The impact of the absorbing length on the wave function is discussed in section 4.2.3.6.

4.2.3.4 Wave function at the exit of the slit

We now have the initial wave function which is given by equation (4.19) (with a normalization coefficient), we have the atom-surface interaction potential, and the absorption function.

We let the initial wave function evolve in the atom-surface interaction potential for $t_e = v/l_{depth}$ (where v is the atom propagation velocity and $l_{depth} = 95$ nm the depth of the nanograting).

The square modulus of the wave function at the end of the slit ($t = t_e$) is plotted figure 4.8a. A zoom in the absorption region is plotted figure 4.8b, where we see that the wave function is absorbed at $r_{min} = 0.35$ nm of the wall, over an absorption length of about ~ 0.2 nm (the effective absorption length is smaller than the length over which the mask function goes from one to zero).

We can also plot the real (figure 4.9a) and imaginary part (figure 4.9b) of the
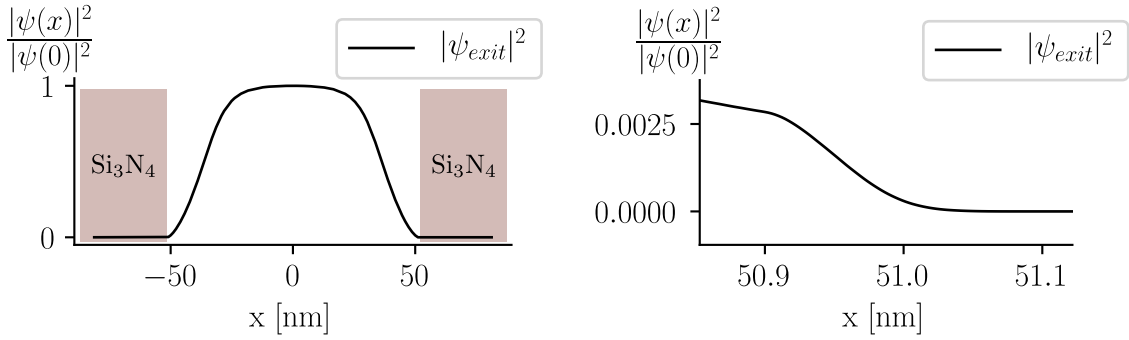
(a) Square modulus of the wave function at the exit of the slit. $a_{slit} = 102.7$ nm

(b) Zoom on the absorption region. $a_{slit} = 102.7$ nm, so the surface is located at 51.35 nm

Figure 4.8: Square modulus of the wave function at the exit of the slit.

wave function at the end of the propagation for $a_{slit} = 102.7$ nm.
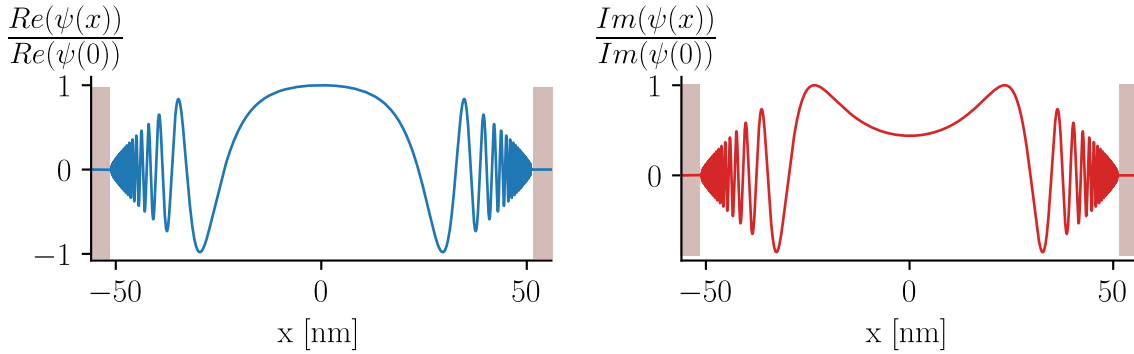
(a) Real part of the wave function at the exit of the slit. The red pale zones indicate the Si_3N_4 bars of the slit.

(b) Imaginary part of the wave function at the exit of the slit. The red pale zones indicate the Si_3N_4 bars of the slit.

Figure 4.9: Real and imaginary part of the wave function at the exit of the slit.

Moreover, it is possible to access the wave function at any desired time step, thus we can reconstruct the dynamics of the wave function inside the slit (see figure 4.10). From this plot, we see that, as the atom propagates through the slit, the probability of finding it near a surface decreases. An analogy can be made with the semi-classical view we used in figure 3.1. The atom is attracted to surfaces, if the atom hits a surface it falls back to the ground state and is therefore not detected. This explains why the norm of $|\psi(x)|^2$ decreases and why $|\psi(x)|^2$ seems to become thinner as the atom evolves in the slit.

As we can see from the equation (4.11) (stationary phase approximation), the wave function on the detector is related to the Fourier transform of the wave func-

tion at the exit of the slit. Therefore, the thinning of the wave function implied by the atom-surface interactions contributes to enlarge the diffracted pattern. Moreover, the same argument illustrates the importance to access the shape of the wave function at the exit of the slit.
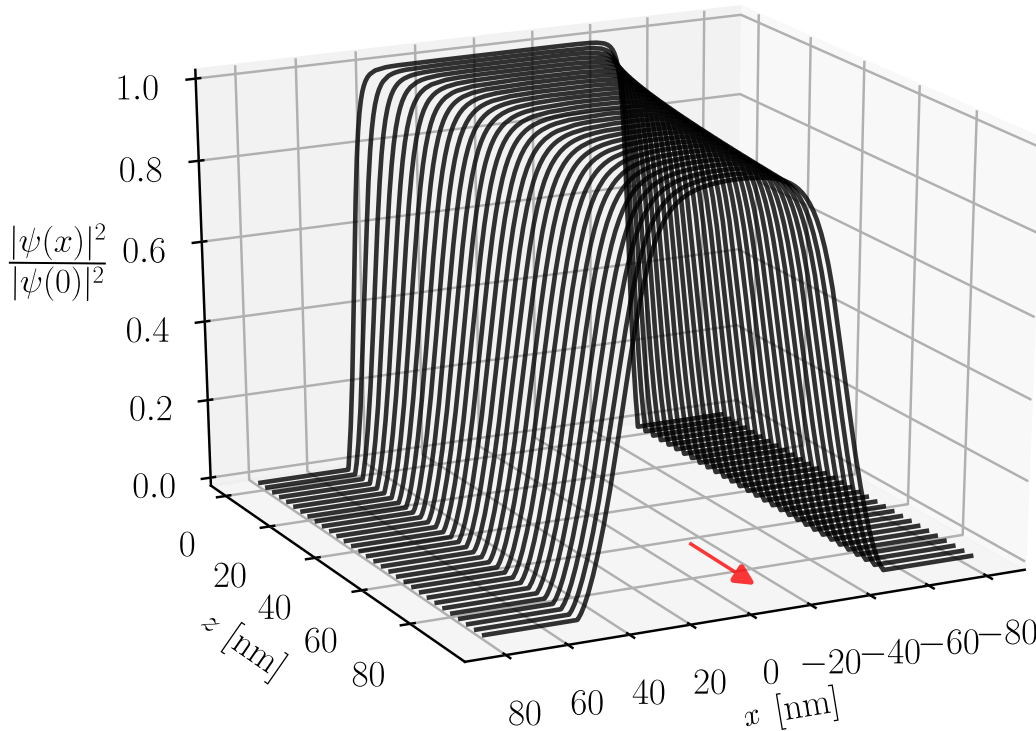
Figure 4.10: Evolution of the square modulus of the wave function in the slit ($a_{slit} = 102.7$ nm).

4.2.3.5   Convergence of the simulation

In section 4.1 we mentioned the need to verify the convergence of the simulation. To do so, we said that we need to see if the result does not change while reducing the space grid resolution $dx \rightarrow dx/2$ and reducing the time step $dt \rightarrow dt/2$. Here the subtlety comes from the mask function we use to absorb the wave function. Absorption is improved when the time step dt is reduced. Thus, in the absorption region the wave function is always different. Therefore one always have a different result while reducing the time step and might think that the simulation does not converge.

A way to understand the improvement of the absorption while reducing dt, is

that with a small time step, the wave function does not change a lot and so there are no abrupt changes involved by applying the mask function. Any abrupt change in the mask function will induce mechanically numerical reflections or instabilities. This is why we used a function that does not go directly from 1 to 0.

Therefore, to test the convergence of the simulation, we need to define two different time steps, dt the time step of propagation and Δt the time step of absorption. This means that we do not necessarily absorb the wave function at the end of the propagation over dt. To test the convergence, we check if the square modulus of the wave function at the exit of the slit changes significantly while changing $dt \rightarrow dt/2$ for the same Δt . The result is given in table 4.1. In the last column, R gives the variation between the integral of the square modulus of the wave function for the two different time steps dt. The column entitled "Evaluated" is a visual evaluation. A *Bad* result is illustrated figure 4.11, where there are reflections in the absorption region. A *Good* result is illustrated figure 4.12. If visually the result is considered as *Bad*, then the variation difference (R) is not estimated, as we do not keep this result.

v (m/s)	Δt (.10^{-9} ms)	dt (.10^{-9} ms)	Evaluated	R=1-$\frac{int1}{int2}$
19.5	0.5	0.5	Good	
		0.25	Bad	
	0.25	0.25	Good	$3,6.10^{-7}$
		0.125	Good	
	0.1	0.1	Good	$3,9.10^{-7}$
		0.05	Good	

Table 4.1: Table with the different parameters to evaluate the convergence of the simulation

We performed the same convergence test for the different velocity ranges of interest [18.7, 19.5] m/s, [25.5, 26.9] m/s, also for the different slit size we used (102.7 nm and 97.5 nm) and for a range of C_3 atom-surface interaction coefficient $\in$ [1.05, 1.40] a.u.

The results of all the tests show that taking $\Delta t = dt = 0.25$ ps and a number of grid points such that the spatial resolution $dx = 2.5$ pm leads to a converged simulation for all the parameter range needed. With those time step and spatial resolution, the maximum difference variation (R) observed was ≤ 2.5 x 10^{-6} for the different parameters conditions of interest in our problems.

Figure 4.11: Bad result : in the zoom inset (c) the absorption of the wave function introduce some reflections. In inset (b) the amplitude of the variations is $\delta \sim 5.7$ x10^{-5}. The surface is located at 51.35 nm for $a_{slit} = 102.7$ nm.
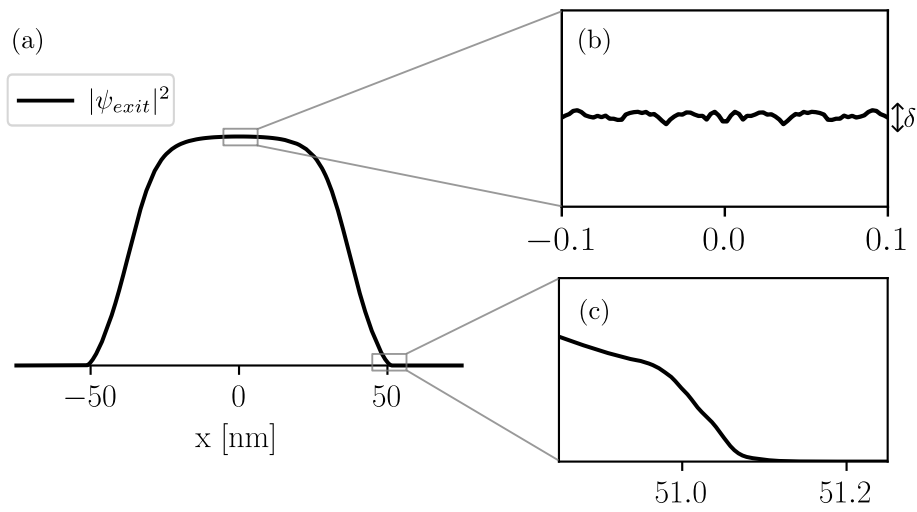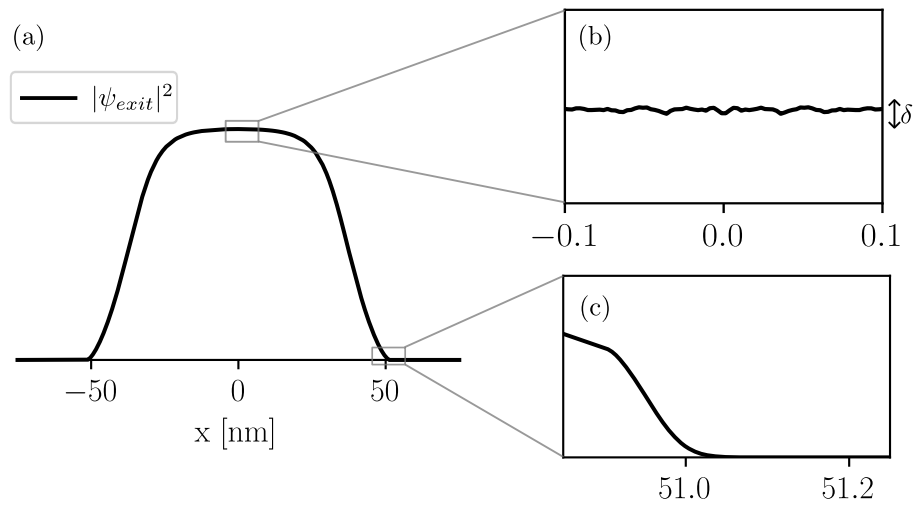

Figure 4.12: Good result : in the zoom inset (c) the absorption of the wave function occur without spurious reflections. In inset (b) the amplitude of the variations is $\delta \sim 2.7$ x10^{-5}. The surface is located at 51.35 nm for $a_{slit} = 102.7$ nm.

4.2.3.6 Influence of the absorption function

The shape of the mask function and its absorbing length influences the shape of the wave function where it should be absorbed. Here, we try to quantify the impact of the absorbing length, and of the modified potential on the wave function at the exit of the slit. To do so, we look at the ratio of the integral of the square modulus of the wave function in the absorbing zone, with the integral of the square modulus of the total wave function, see figure 4.13. We do it first for the initial wave function, since it is at the beginning that the amplitude of the wave function is maximum in the absorbing zones, see figure 4.13a.

$$2 \times \int_{x_{abs}-d}^{+\infty} |\psi(x, t = 0)|^2 dx \bigg/ \int_{-\infty}^{+\infty} |\psi(x, t = 0)|^2 dx \approx 0.12 \ \%. \tag{4.20}$$

At the exit of the slit (at time t_e), due to the loss of atoms close to the surface, the amplitude of the wave function decreases close to the walls, thus

$$2 \times \int_{x_{abs}-d}^{+\infty} |\psi(x, t = t_e)|^2 dx \bigg/ \int_{-\infty}^{+\infty} |\psi(x, t = t_e)|^2 dx \approx 4.5 \times 10^{-4} \ \%. \tag{4.21}$$

This justifies that the absorbing length is sufficiently small to have a negligible influence on the wave function at the exit of the slit. Moreover, this also justifies that the modification of the repulsive part of the potential has a negligible impact on the wave function.
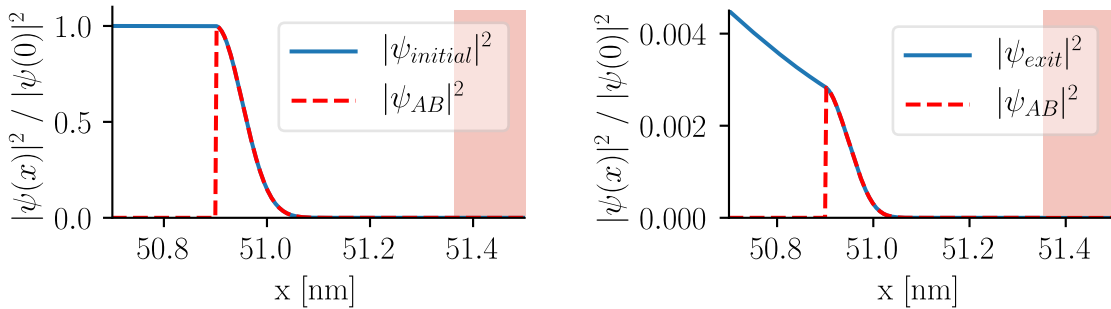
(a) Influence of the absorbing zone on the initial wave function.

(b) Influence of the absorbing zone on the wave function at the exit of the slit.

Figure 4.13: Dashed red lines represent the part of the square modulus of the wave function which is located on the absorbing zone. Solid blue lines represent the square modulus of the wave function, the pale red zone represents the Si_3N_4 surfaces. Here, $a_{slit} = 102.7$ nm.

4.3   Simulation result

We use the stationary phase approximation (see section 4.2.2) to propagate the wave function outgoing from the slit (figure 4.8a) up to the detector. The square modulus of the wave function on the detector is plotted figure 4.14, the envelope represents the diffraction by one slit. Instead of using equation (4.13), we use a Dirac comb with a period equal to the interfringe $i = (\lambda_{dB} D_{gd})/p_g$ (where D_{gd} is the distance from the grating to the detector, p_g the period of the grating) to avoid undesirable grid resolution effects. This is justified because we use a final grid with much fewer grid points than in the propagation simulation. This is also justified by the large number of slits of the nanograting.
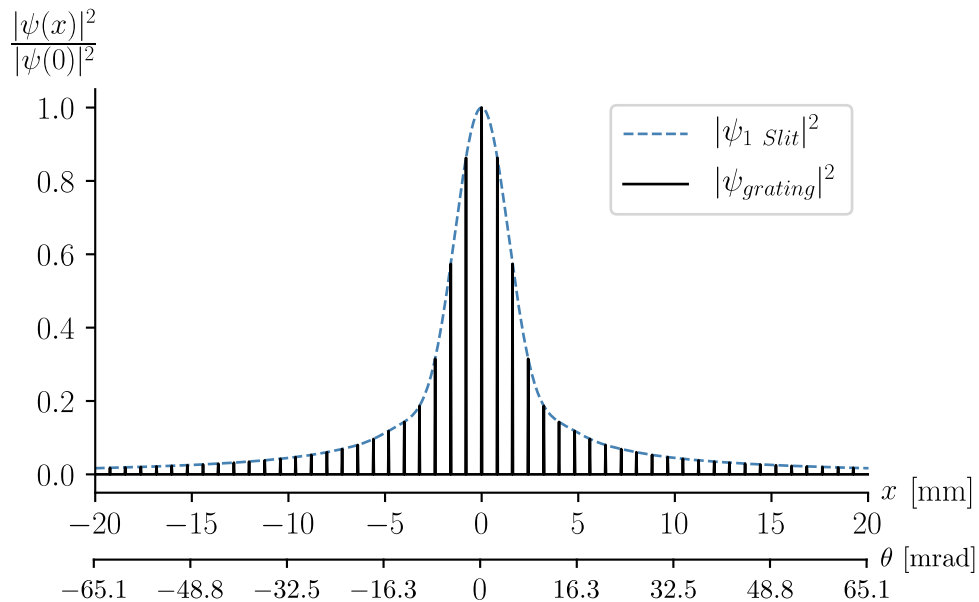
Figure 4.14: Simulation result of the square modulus of the wave function on the detector, for the diffraction by one slit (blue - dashed) and by N>>1 slits (black - solid).

The black curve in figure 4.14, represents the square modulus of the wave function of a single atom diffracted by the nanograting on the detector.

Now, we need to consider the velocity distribution, the slit size distribution, and the angular beam distribution that we have in the experimental results. The diffracted wave function depends on the atom propagation velocity since it defines the de Broglie wavelength and the interaction time in the slit. The velocity distribution cannot be reduced to only consider the wave function diffracted for a mean velocity. The same is true for the slit size distribution due to the stadium shape (see figure 2.21b), the wave function diffracted by different slit sizes is not equal to

the wave function diffracted by an average slit. The stadium shape is taken into account considering that $11/15^{th}$ of the slit has a size $a_{slit} = 102.7$ nm, while $4/15^{th}$ a size $a_{slit} = 97.5$ nm.

To consider the angular beam distribution, we should perform the simulation for the different incidence angles. This is not straightforward to simulate in the 1D approach. However, regarding the source size ($\approx 250 \ \mu$m), the nanograting open length ($L_g = 306 \ \mu$m), and the distance from the source to the grating ($D_{sg} \approx 503$ mm), the incidence angle are $\lesssim 0.035°$. We experimentally observed influence of the orientation of the nanograting with respect to the propagation axis for angles $\gtrsim 0.2°$, thus we consider in a first approximation that the wave function at the end of the slit does not depend on the incidence angle.

4.3.1   Angular beam distribution

As discussed in section 4.2.1, the atoms in the source can be regarded as an ensemble of independent Gaussian wave functions. These wave functions spread during free propagation (~ 26 ms) from the source to the nanograting, so that they cover uniformly all the slits of the nanograting. So, on the detector the square modulus of the wave function of an atom is given by $|\psi_{grating}|^2$ illustrated in figure 4.14.

Since the source has spatial extension and that we push the atoms, all atoms do not arrive with the same incidence angle on the nanograting. In first approximation, two different atoms (with different incidence angles) will be represented by the same $|\psi_{grating}|^2$ on the detector but centered around different positions. This is illustrated in figure 4.15. Hence the angular beam distribution which is both due to the spatial extension of the source and the pushing process will smear the final detected pattern. This loss of visibility in an extended incoherent source in classical optics is referred to as *spatial coherence* [41].

Finally, to take into account the spatial coherence of our source of atoms, we take the convolution product between $|\psi_{grating}|^2$ and the angular beam distribution, as in section 3.1.3. In the experiment, the angular beam distribution fits in first approximation a Gaussian function with standard deviation $\sigma_{beam} = 0.23$ mrad at 26 m/s ($\sigma_{beam} = 0.25$ mrad at 19 m/s).
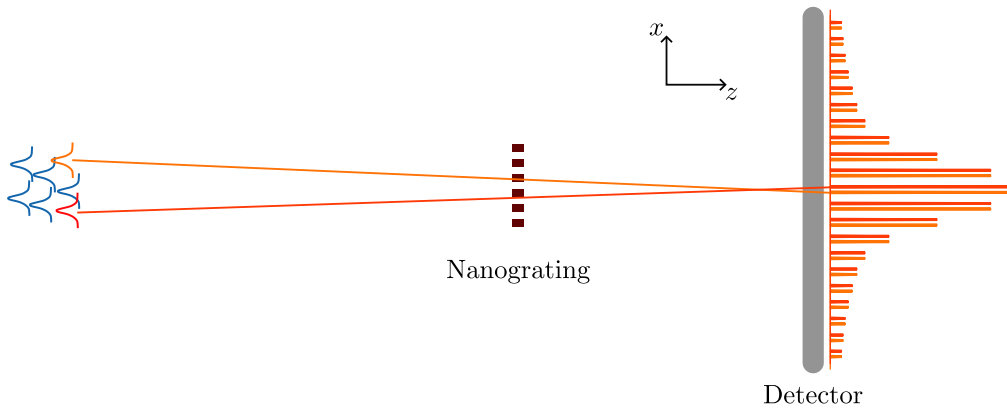
Figure 4.15: Visibility loss due to the spatial extension of the source and the pushing process.

4.3.2 Velocity distribution

Previously, we took into account the spatial coherence of the source, and now we focus on the temporal coherence of the source. Our experimental setup allows us to post-select atoms with respect to their time of flight, and since we selected a very short time-of-flight range (see figure 4.16), we consider that the velocity distribution is uniform for both experimental data sets (section 2.4). For larger time of flight one should take into account the Jacobian determinant to get the velocity distribution from the time-of-flight distribution.
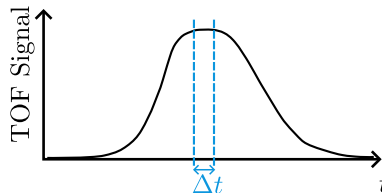
Figure 4.16: TOF distribution, the two dashed blue lines represent the TOF post-selection.

To take into account the velocity distribution, we want to perform a continuous sum of periodic functions (the wave functions diffracted by N slits) but on a discrete number of velocities (we want the simulation time to remain reasonable). It is therefore necessary to find the best way to avoid any beat-notes phenomena. To do so, we consider a problem close to the one we are interested in, but for which we have an analytical solution. We look for the best way to numerically compute the following integral,

$$I(x) = \frac{1}{\omega_{max} - \omega_{min}} \int_{\omega_{min}}^{\omega_{max}} \cos^2(\omega x) d\omega, \tag{4.22}$$

the analytical result is given by

$$I(x) = \frac{1}{2} + \frac{\sin(2\omega_{max}\ x) - \sin(2\omega_{min}\ x)}{4(\omega_{max} - \omega_{min})\ x}. \tag{4.23}$$

Now let consider the arithmetic average

$$I_{sum}(x) = \frac{1}{N} \sum_{n=1}^{N} \cos^2(\omega_n\ x), \tag{4.24}$$

where $\omega_n = \omega_{min} + (n-1)\frac{\omega_{max}-\omega_{min}}{N-1}$, and where we will set $N = 11$.

Finally, let us consider the numerical integration method, using the following function of the Scipy package for Python [42] *scipy.integrate.simpson*

$$I_{simps}(x) = \frac{1}{\omega_{max} - \omega_{min}} integrate.simpson(\cos^2(\omega_l\ x), \omega_l) \tag{4.25}$$

where ω_l is the lth element of a list of length $N = 11$, and integrate.simpson is the numerical integration method. Now we want to see what is the most accurate method between (4.24) and (4.25) to get the closest result to equation (4.23). To do so, we plot the difference $(I(x) - I_{sum}(x))/I(x)$ and $(I(x) - I_{simps}(x))/I(x)$ in figure 4.17.
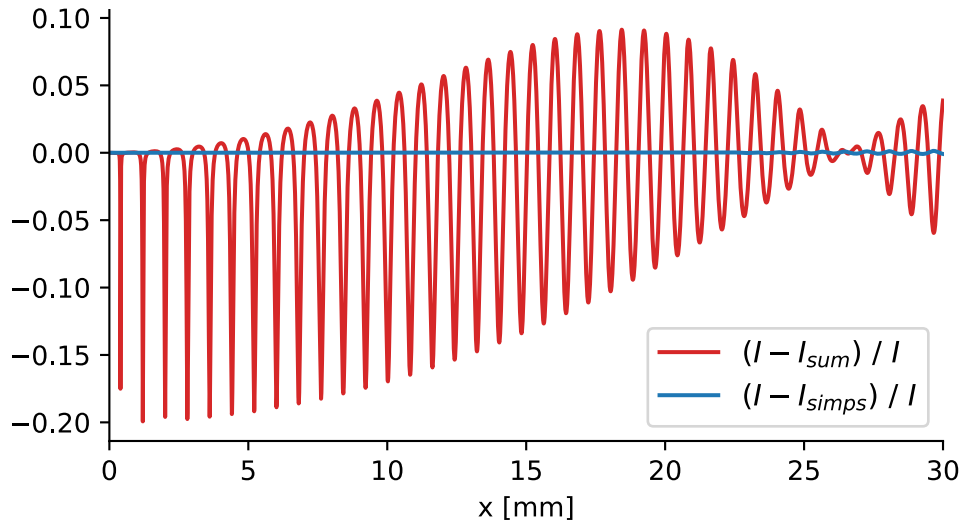
Figure 4.17: Difference between an analytic solution and two approximation method; in red with a simple discrete sum, and in blue with a numerical integration algorithm.

In figure 4.17 we used

$$\begin{cases} \omega_{max} & = \pi \frac{m\ p_g}{h\ D_{gd}} v_{max} \approx 4.0 \text{ mm}^{-1} \\ \\ \omega_{min} & = \pi \frac{m\ p_g}{h\ D_{gd}} v_{min} \approx 3.8 \text{ mm}^{-1}, \end{cases} \tag{4.26}$$

for $v_{max} = 19.5$ m/s and $v_{min} = 18.7$ m/s, to have a test model as close to our problem of interest as possible.

From this we see that it is important to use the appropriate numerical method to compute the continuous sum on a discrete sample. Furthermore, we see that for 11 velocities, the discrepancy between the analytical result and the numerical integration method is ≤ 1.5 ‰ $\forall\ x \in [-30, 30]$ mm, while the discrepancy is up to 0.2 % when taking the arithmetic average.

Hence, to get the final result, we perform the simulation for 11 different velocities in the velocity range of interest and take into account the velocity distribution by mean of the numerical integration method with Simpson's rule.

Note : the numerical integration method with Simpson's rule [30], requires an even number of intervals (in our case 11-1=10).

4.3.3   Slit size distribution

We take into account the stadium shape of the slit (see figure 2.21) in two steps. First, we normalize the wave function at the end of the slit by the same reference for both slit sizes. This means that we will have fewer atoms that are outgoing from the smaller slit,

$$\begin{cases} \psi(x, t_e; a_{slit} = 102.7) & \rightarrow\ \psi(x, t_e; a_{slit} = 102.7)/\sqrt{N_{ref}} \\[2ex] \psi(x, t_e; a_{slit} = 97.5) & \rightarrow\ \psi(x, t_e; a_{slit} = 97.5)/\sqrt{N_{ref}}, \end{cases} \tag{4.27}$$

where N_{ref} is the reference norm. We choose

$$N_{ref} = \int dx\ \left|\psi(x, t = 0; a_{slit} = 102.7)\right|^2. \tag{4.28}$$

Second, we will consider that diffraction by the slit of size $a_{slit} = 102.7$ nm will contribute to $11/15^{th}$ of the final detected pattern, while the diffraction by a slit of size $a_{slit} = 97.5$ nm contribute to $4/15^{th}$. These slit sizes come from the experimentally measured slit size distribution, see figure 2.21b.

4.3.4   Final result

Finally taking into account all what we mentioned before, considering an atom-surface interaction coefficient $C_3 = 1.25$ a.u we obtain the result plotted figure 4.18, for atom propagation velocity $v\ \in [18.7, 19.5]$ m/s. It is important to remind

the reader that except the chosen value of r_{min} there are no free parameters in this simulation approach. In future simulations, r_{min} should be changed according to the complete QED calculation of the Casimir-Polder potential. The angular beam distribution at 19m/s fits a Gaussian distribution with standard deviation $\sigma_{beam} = 0.25$ mrad. The angular beam distribution is different from that at 26 m/s even if the open surface of the nanograting is unchanged ($L_g = 306$ μm). This is because in the experimental apparatus, we only have a slit in front of the nanograting. Thus, for different propagation velocity, the source size can be slightly different (at the end of the pushing process).
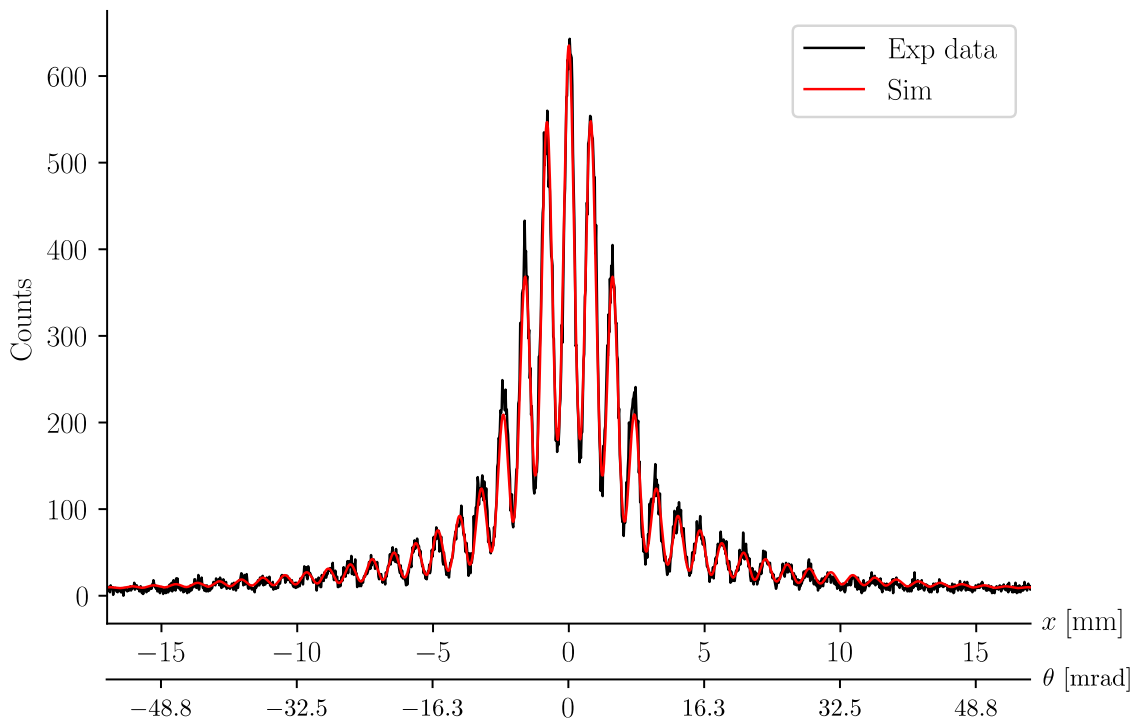
Figure 4.18: Simulation result for $C_3 = 1.25$ a.u (red), experimental data for $v \in [18.7, 19.5]$ m/s (black).

In figure 4.18, we plot both the data and the simulation result. What we see is that the physical phenomenon seems to be well taken into account. Nevertheless, this should not be considered as a measurement, because, we need to first test the model we presented in this chapter by doing a goodness-of-fit test before pretending to perform a measure of the atom-surface interaction potential. This is the topic of chapter 5.

Simulation can also be used for the experimental data set at 26 m/s. Here, we consider $C_3 = 1.25$ a.u. $\sigma_{beam} = 0.23$ mrad. The propagation velocity of the atoms

$v \in [25.5, 26.9]$ m/s. The result is plotted figure 4.19.
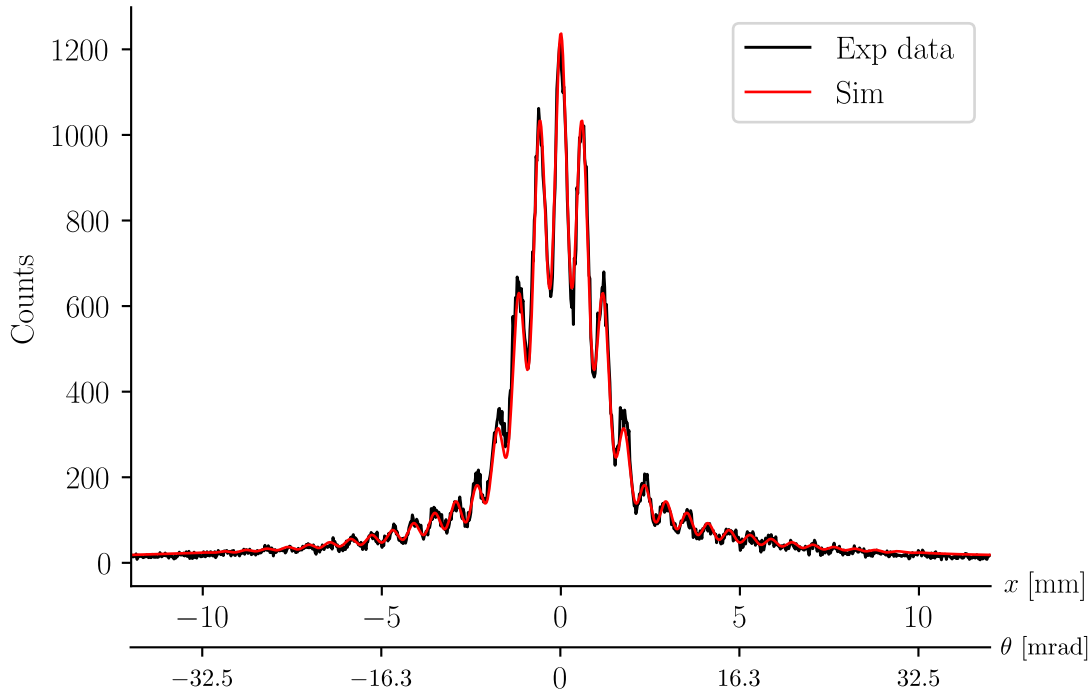
Figure 4.19: Simulation result for $C_3 = 1.25$ a.u (red), experimental data for $v \in [25.5, 26.9]$ m/s (black).

4.3.5   Outlook using the 1D-TDSE model

The model presented in this chapter allows us to obtain results close to the experimental results at 19 and 26 m/s. We can therefore use this model to make theoretical predictions. The experiment was designed to reach low propagation velocities. Thus, it is interesting to see what happens if we reduce the velocity. One may ask whether there is a velocity below which no more atoms exit the nanograting. Before trying to give an answer to this question, we focus on a case that is experimentally feasible.

Hereafter, we look at the predicted diffraction pattern we obtain when we consider the nanograting we have, but for atoms propagating at $v = 10.0$ m/s. We do not take into account any velocity distribution, however we still take into account the angular beam distribution. We assume that the angular beam distribution follows a Gaussian distribution with standard deviation $\sigma_{beam} = 0.25$ mrad. The result is plotted figure 4.20.

We see that by reducing the velocity, the envelope of the diffracted pattern is enlarged. This is mainly due to the thinning of the wave function at the exit of the

Figure 4.20: Simulation result for $C_3 = 1.25$ a.u, $p_g = 200.0$ nm, $a_{slit} = 102.7$ nm, $\sigma_{beam} = 0.25$ mrad and $v = 10.0$ m/s.

slit. Moreover, visibility is improved because reducing the atom propagation velocity increases the de Broglie wavelength and therefore the interfringes (see section 4.3.1). The main limitation to overcome in the experiment is to increase the atomic flux.

For lower velocities, in the simulations we still have a wave function coming out of the slit, but it is very narrow, because only the atoms passing through the middle of the slit will come out. The diffraction pattern on the detector becomes wider while we reduce the velocity. The widening of the diffraction pattern is not trivial and is related to the Fourier transform of the wave function at the slit exit (and so depends on the shape of $|\psi_{exit}|^2$).

The nanogratings are manufactured in the OIA team, thus it would be possible to get other geometries. In the following, we look at a diffraction pattern for atoms propagating at 19.1 m/s, but for a nanograting with slit size $a_{slit} = 50.0$ nm, period $p_g = 100.0$ nm and depth $l_{depth} = 95.0$ nm. The angular beam distribution is also considered as a Gaussian distribution with standard deviation $\sigma_{beam} = 0.25$ mrad. The result is plotted in figure 4.21.

We see that the diffraction envelope is larger because atoms propagate at distances lower than 25 nm from a surface, so the interactions are strong enough to get a narrow wave function at the exit. The visibility is also improved as the interfringe

75

is enlarged due to the smaller period of the nanograting.

The benefits of such a nanograting geometry are related to the possibility to explore the atom-surface interactions for very short separation distances.
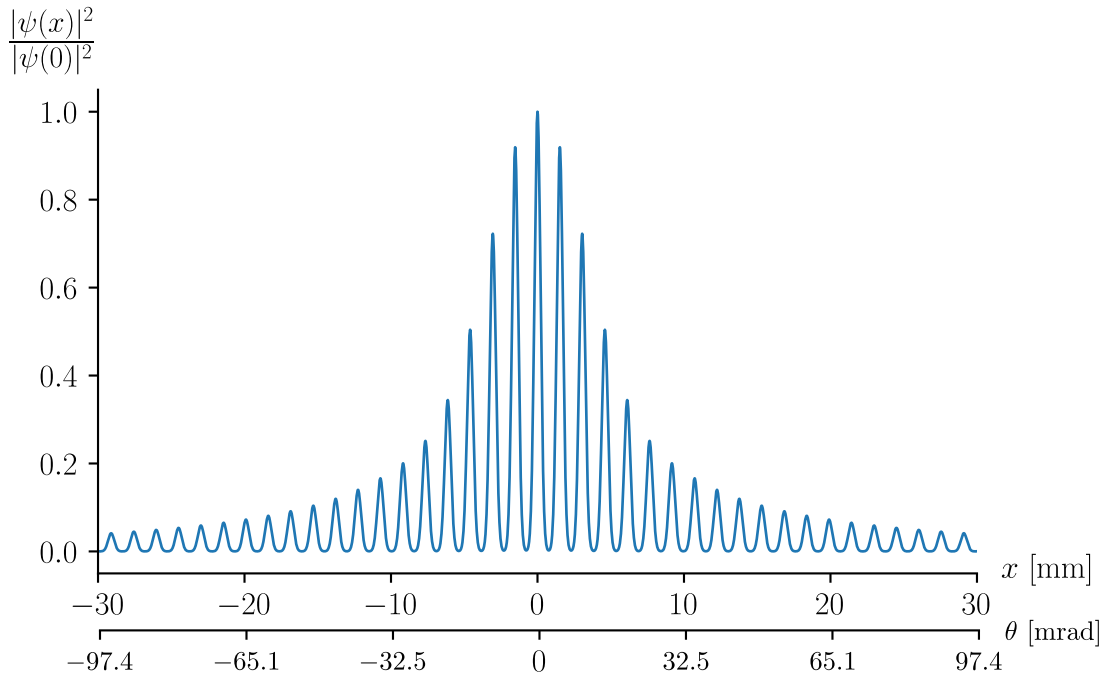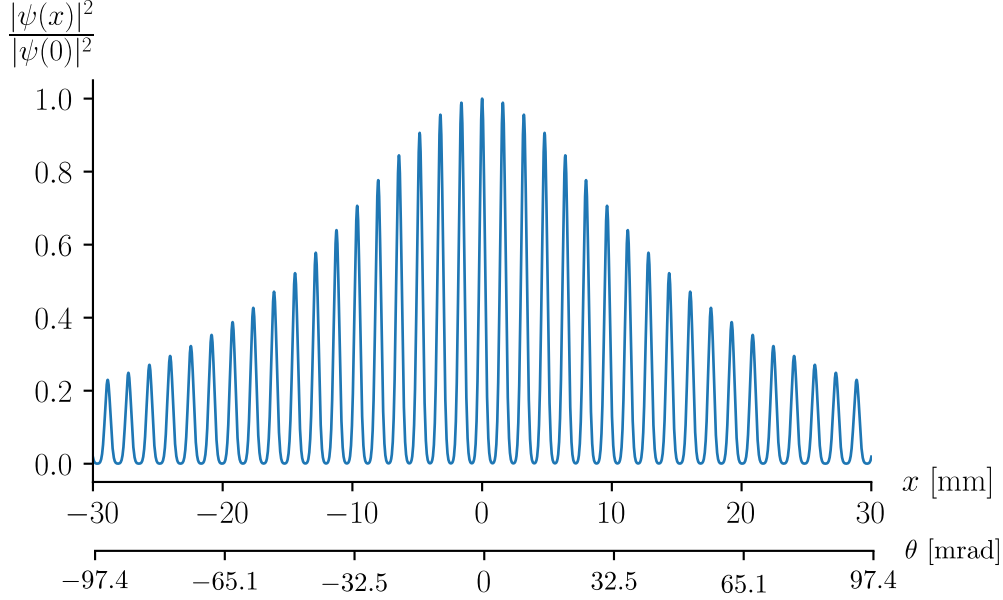

Figure 4.21: Simulation result for $C_3 = 1.25$ a.u, $p_g = 100.0$ nm, $a_{slit} = 50.0$ nm, $\sigma_{beam} = 0.25$ mrad and $v = 19.1$ m/s.

4.3.6   Interdependence of the parameters

We mentioned in chapter 3 that some parameters modify the diffraction pattern in the same manner. For example, reducing C_3 and reducing a_{slit}, can possibly lead to a very similar diffraction pattern as if we take a larger C_3 and larger a_{slit}.

To illustrate this, let consider the following case :

$$\begin{cases} l_{depth} & = 95.0 \text{ nm, nanograting depth} \\ v & = 19.0 \text{ m/s, atom propagation velocity} \\ \sigma_{beam} & = 0.230 \text{ mrad, angular beam distribution} \\ D_{gd} & = 307.0 \text{ mm, distance from the nanograting to the detector} \\ a_{slit} & = 100.0 \text{ nm, size of the slit of the nanograting} \\ C_3 & = 1.250 \text{ a.u, atom-surface interaction coefficient} \end{cases} \quad (4.29)$$

The corresponding simulation result is labeled ψ_1. Now we look for the atom-surface interaction coefficient C_3 which give the closest result while taking $a_{slit} = 99.0$ nm. We obtain the result labeled ψ_2 for $C_3 = 1.196$ a.u. The two results are plotted figure 4.22. The difference $||\psi_1(x)|^2 - |\psi_2(x)|^2| \leq 2.8 \times 10^{-3} \ \forall \ x \in [-30.0, 30.0]$ mm.

This means that for 100000 total number of atoms detected, the difference would be less than 3 atoms in a single bin (wherever the bin). The same analysis can be done with the depth of the nanograting. This gives us the systematic uncertainties related to the nanograting geometry,

$$\begin{cases} \Delta a_{slit} = \pm 1 \text{ nm} \Rightarrow \Delta C_3 = \pm 0.06 \text{ a.u} \\ \\ \Delta l_{depth} = \pm 5 \text{ nm} \Rightarrow \Delta C_3 = \pm 0.06 \text{ a.u} \end{cases} \tag{4.30}$$

These systematic uncertainties are consistent with what has been estimated with the semi-classical model in section 3.2.1.
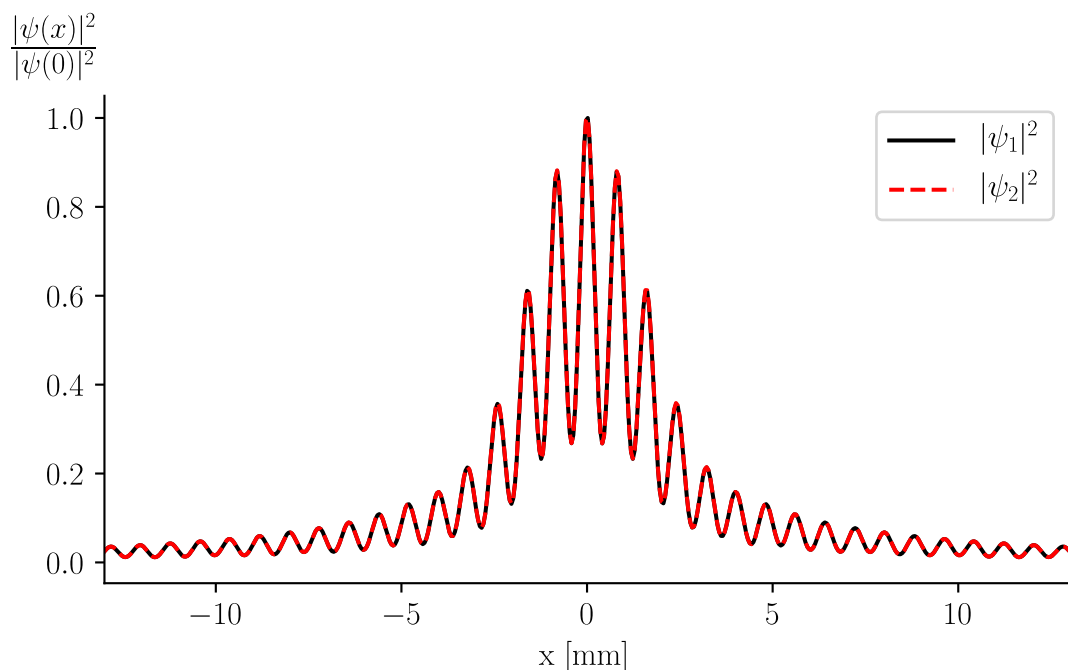
Figure 4.22: Black : simulation result for $C_3 = 1.25$ a.u, $a_{slit} = 100.0$ nm. Red : simulation result for $C_3 = 1.196$ a.u, $a_{slit} = 99.0$ nm

4.4 Main limitations of the 1D TDSE approach

If the simulation, as plotted in figure 4.18, seems to give correct results, before we perform goodness-of-fit tests it is important to keep in mind the main assumptions we made in this 1D TDSE approach. Those are listed below.

1. When we take into account the angular beam distribution, we do not take into account the influence of the incidence angle on the wave function at the exit of the slit. The wave function at the exit of the slit should depend on the incidence

angle since the atom will not experience the same potential depending on the angle. Thus it would be better to get the wave function depending on the incidence angle, and then to take into account the angular beam distribution the same way as we did for the velocity distribution but by taking a Gaussian instead of a uniform distribution. Unfortunately, it is not straightforward to add an angle dependence in the 1D approach.

2. We used the same Wylie and Sipe potential as in section 3.1.4. As we already mentioned also in this section, this atom-surface interaction potential is derived assuming sufficient atom-surface distance to consider the atom as a dipole. Also for the repulsive part we added, it could be of another dependence (different power law) with respect to the atom-surface distance, see [43].

3. We used Bohr model to define a minimum atom-surface distance r_{min}. This model might be reasonable for Ar* atoms freely propagating from the source to the nanograting. However, inside the nanograting slits, this minimum distance r_{min} could be larger, e.g., with respect to the nature of atom-surface interactions, the excited electron level should be shifted by the Stark effect. Thus even considering a spherical atom, its radius would be larger in the slit.

4.5 Difficulties related to a 2D simulation

The problem we are interested in is illustrated with the different scales involved figure 4.23.
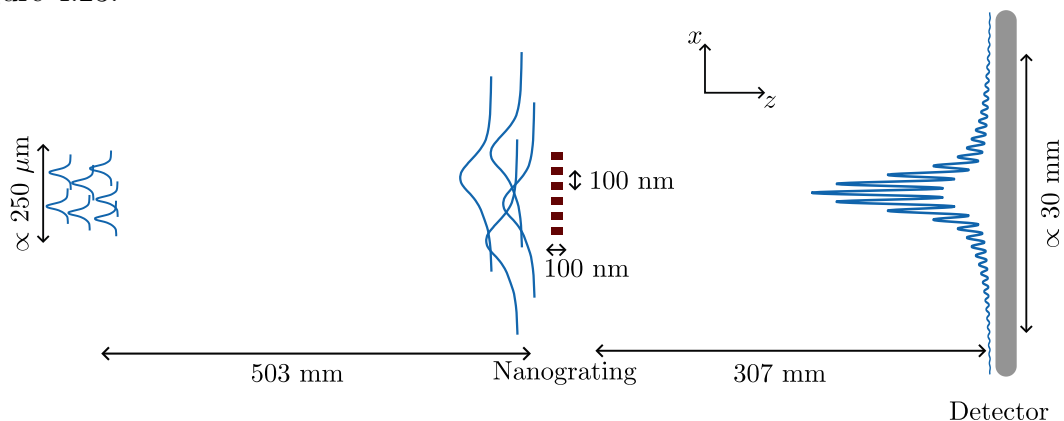
Figure 4.23: Schematic representation of the problem

There are two different ways to look at the considered problem in order to simulate it on a 2D grid (x,z):

1. the 2D grid represents the laboratory reference frame.

2. the 2D grid represents the atom reference frame.

In both cases, due to the energy involved by the atom-surface interaction potential, we need a spatial resolution of 2.5 pm (see section 4.2.3.5). We need this resolution in both x and z directions to take into account the atom-surface potential at the entrance and exit of the nanograting.

In approach n°1, if we take $L_z \approx 80$ cm and $L_x \approx 3$ cm, then $ngpz \approx 2^{38}$ and $ngpx \approx 2^{33}$ (where $ngpx$ and $ngpz$ are the number of grid points for x and z axis respectively). Thus, we would need to perform the simulation on a 2D grid with $\approx 2^{71}$ grid points. This is impossible.

In approach n°2, we need a 2D grid which contains most of an atom wave function. The detected pattern is about 3 cm large, which means that the wave function associated to an atom should be about the same order of magnitude. Thus, we would need a 2D square grid with $L_z = L_x \approx 3$ cm, so the 2D grid should be made out of $\approx 2^{66}$ grid points. One could also try to simulate the problem only around the nanograting since everywhere else it is only free propagation. In this case, the wave function is represented by a Gaussian function with standard deviation $\sigma \approx 0.465$ mm as we justify in section 4.2.1. Taking a square grid with $L_z = L_x = 6\sigma \approx 2.8$ mm (in order to contain 99.7% of the wave function), one would still need a 2D grid made out of $\approx 2^{60}$ grid points. Therefore, this approach is also not feasible.

One could think to use a non-linear grid or an adaptive grid. These numerical methods are quite difficult to implement. Since we were trying to develop a new approach to model our data, we decided to develop a simple 1D model to see the needed numerical resources (resolution, number of grid points, etc.) to properly simulate the atom-surface interactions in our experiment.

4.6   1D TDSE model summary

1. We developed a 1D simulation approach based on the numerical resolution of the time-dependent Schrödinger equation.

2. Regarding the experimental conditions, we assumed that atoms reaching the nanograting are represented by plane waves. Also, the propagation from the nanograting to the detector is analytical by making use of the stationary phase approximation.

3. We only have to simulate the evolution of the wave function inside a single slit. The initial wave function takes the form of the slit, it is then propagated by letting it evolve in the atom-surface potential during $t = v/l_{depth}$.

4. Simulation convergence tests led us to use a spatial resolution $dx = 2.5$ pm and a time resolution $dt = 0.25$ ps.

5. The loss of metastable atoms is considered by absorbing the wave function when it reaches the surfaces.

6. We defined a minimum atom-surface distance at which the wave function has to be absorbed based on Bohr's model.

7. We took into account the angular beam distribution. And also, we took into account the velocity distribution by means of a numerical integration algorithm.

Chapter 5

Statistical data analysis

In the previous chapter, we presented a new model which seems to represent well the experimental results. However, a qualitative approach is not sufficient to judge the accuracy of the 1D-TDSE model. In this chapter, we will see different statistical tools to test the agreement or not between the 1D-TDSE model and the experimental results. The results presented in this chapter are also due to fruitful discussions with Dr. Benoît Darquié.

We did not realize this procedure in chapter 3, because, on the one hand, the model did not allow it (not close enough to the experimental data) and on the other hand, the objective was not to make a measurement of the atom-surface interactions. The objective was to compare two models of the atom-surface interaction.

Here, the goal is to measure the atom-surface interactions potential with the 1D-TDSE model. But the model must be tested before claiming to make a measurement. To do so, we will start by introducing the appropriate statistical tools for a multinomial histogram (which correspond to the experimental data set we have). We also review goodness-of-fit test, and apply it to the 1D-TDSE model. We show that the model is rejected by the experimental data presented in section 2.4. Such result is explained thereupon. Suggestions for corrections to the model are given at the end of this chapter.

5.1   Data binning

First of all, we need to start by defining the data binning. The detector determines the arrival position of the electron avalanche on a continuous copper wire. Thus, if the numerical precision is infinite, the set of position is continuous.

Huge number of digits in the calculated position is meaningless, several factors

(such as the size of the holes of the MCP) limit the position resolution of the detector. Thus, we can *bin* the data, see figure 5.1.

This means that the position set is dicretized in N_x intervals called *bins*. So we construct a histogram that gives us the number of atoms detected per bin.

Then we can choose the data binning. For a large number of bins N_x we have better spatial resolution but fewer atoms per bin, conversely for a small number of bins we have more atoms per bin but we loose

Figure 5.1: data binning illustration

spatial resolution. Therefore, the choice of the binning is a balance between large atom numbers and enough binning.

5.2 Statistical tools

5.2.1 The likelihood

One of the statistical tools we will use to compare our model to the data is the so-called "likelihood". We define the likelihood following the approach given in [44]. Consider the experimental data set at 19 m/s figure 2.23. We are interested in the probability that our theory is correct regarding this experimental data set. We write this probability (following the notation in [44]): *P(theory|data)*. This is a conditional probability which, by making use of Bayes' theorem, can be expressed as

$$P(\text{theory}|\text{data}) \propto P(\text{data}|\text{theory})\ P(\text{theory}), \qquad (5.1)$$

P(theory) : probability that the theory is true.
P(data|theory) : The likelihood. Probability of observing the obtained data under the considered theory.

Since we don't know *P(theory)*, it is impossible to access the probability that the theory is correct regarding the data. In section 5.3, we see how we can test a theory using computational techniques.

First, let define the notations, following those used in [45]. Let $\vec{n} = (n_1, n_2, ..., n_{N_x})$, represent the observed data and let n_i give the number of measured atoms in the ith bin. N_x is the total number of bins, and N_{exp} is the total number of atoms in the

experimental data set: $N_{exp} = \sum_i n_i$.

Let $\vec{y}(\vec{\theta}) = (y_1(\vec{\theta}), y_2(\vec{\theta})..., y_{N_x}(\vec{\theta}))$, where $y_i(\vec{\theta})$ represent the predicted number of atoms in the ith bin, and $\vec{\theta}$ the set of parameters in the model. We write the underlying theoretical probability density function $p(\vec{\theta})$.

We need to define the null hypothesis H_0 : $\vec{n}$ is a random sample of our theoretical model. We then use the following notation for the likelihood : $\mathcal{L}(H_0) = P(data|theory)$.

Actually, looking for the best fit, means to look for the parameters $\vec{\theta}$ which maximize the likelihood $\mathcal{L}(H_0)$. In other words, we are looking for the set of parameters that maximizes the probability of obtaining the observed data from the theoretical model considered.

To see how we should proceed to find the best fit parameters, let consider the following problem illustrated figure 5.2.
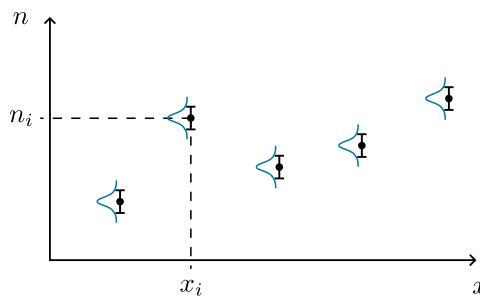
Figure 5.2: Illustration of an experimental data set with normally distributed data points

We consider that the experimental data are Gaussian distributed and that all bins are independent. Thus, following [46], the likelihood writes :

$$\mathcal{L}(H_0) = \prod_i \frac{1}{\sqrt{2\pi}\sigma_i} \exp\left(-\frac{\left(n_i - y_i(\vec{\theta})\right)^2}{2\sigma_i^2} \right). \tag{5.2}$$

σ_i is the standard deviation in the ith bin.

To find the maximum likelihood, one can make use of the likelihood ratio λ, which corresponds to the ratio between the likelihoods of two different hypothesis (two different models),

$$\lambda = \frac{\mathcal{L}(H_0)}{\mathcal{L}(H_1)}, \tag{5.3}$$

For the hypothesis H_1, one can use the saturated model. The saturated model is a model set to be equal to the observed data in each bin : $y_i = n_i \, \forall \, i$. Thus, $\mathcal{L}(H_1)$ does not depend on $\vec{\theta}$.

So, for Gaussian distributed data, the likelihood ratio writes

$$\lambda = \prod_i \exp \left(-\frac{\left(n_i - y_i(\vec{\theta})\right)^2}{2\sigma_i^2} \right), \tag{5.4}$$

and by defining

$$\chi^2 = -2 \ln(\lambda), \tag{5.5}$$

one gets the usual

$$\chi^2 = \sum_i \frac{\left(n_i - y_i(\vec{\theta})\right)^2}{\sigma_i^2}. \tag{5.6}$$

The saturated model does not depend on the the model parameters, thus finding the parameter set $\vec{\theta}$ which minimize χ^2 equation (5.6), one gets the maximum for $\mathcal{L}(H_0)$, since $\chi^2 = -2 \ln(\mathcal{L}(H_0)) + 2 \ln(\mathcal{L}(H_1))$.

About the standard deviation σ_i in equation (5.6), there are three typical cases. First, one can assume that data points follow a normal distribution with the same standard deviation in each bin, then $\sigma_i = \sigma$ and so minimizing equation (5.6) is the same as mininmizing $R^2 = \sum_i \left(n_i - y_i(\vec{\theta})\right)^2$, which is called the least square. Second, one can set $\sigma_i = \sqrt{n_i}$, and get the *Neyman* χ^2 we used in chapter 3,

$$\chi^2_{Ney} = \sum_i \frac{\left(n_i - y_i(\vec{\theta})\right)^2}{n_i}. \tag{5.7}$$

Third, one can set $\sigma_i = \sqrt{y_i(\vec{\theta})}$, this lead to the *Pearson* χ^2

$$\chi^2_{Pear} = \sum_i \frac{\left(n_i - y_i(\vec{\theta})\right)^2}{y_i(\vec{\theta})}. \tag{5.8}$$

Those estimators are widely used because they can also be used for goodness-of-fit tests. As indicated in [45], the χ^2 as defined in equation (5.5), thanks to the likelihood ratio test theorem, will follow asymptotically a χ^2-distribution.

However, one should be careful while interpreting the value of the χ^2 in terms of goodness of fit. As it is underlined in [46], the χ^2 defined equation (5.5) will follow

a χ^2-distribution only if the number of detected atoms in each bin is large. Moreover, the Neyman χ^2_{Ney} is the slowest (compared to χ^2_{Pear}) to reach its asymptotic behavior.

In conclusion, with this simple example, we have recalled where the usual χ^2 test comes from. Furthermore, we see that using one of the three forms mentioned above $(R^2, \chi^2_{Ney}, \chi^2_{Pear})$, we assume that the experimental data are normally distributed. This might be the case if a large number of atoms is detected in a bin thanks to the central limit theorem. However, in our case, only few atoms per bin are present in the tails of the diffracted patterns. Therefore, to use one of the χ^2 forms (5.7) or (5.8) is not appropriate.

5.2.2   Multinomial histogram

It is important to understand how our experimental data are distributed, since it also defines the likelihood $\mathcal{L}(H_0)$.

The theoretical probability to detect an atom in the ith bin is $p_i(\vec{\theta})$. Thus, after N_{exp} trials, the expected number of atoms in the ith bin is given by $y_i(\vec{\theta}) = N_{exp}\, p_i(\vec{\theta})$, and the variance is given by $N_{exp}\, p_i(\vec{\theta})(1 - p_i(\vec{\theta}))$.

In the case where we would have only one bin, we recognize the binomial distribution. Here since we have more than one bin it is a multinomial distribution. Indeed, "An example of the multinomial distribution is a histogram containing N events distributed in k bins, with r_i events in the ith bin" [47].

The likelihood for a multinomial histogram is given in [45],

$$\mathcal{L}(H_0) = N_{exp}!\; N_{exp}^{N_{exp}} \prod_i \frac{\left(y_i(\vec{\theta})\right)^{n_i}}{n_i!}. \tag{5.9}$$

Using the likelihood ratio and the saturated model, the authors of [45] constructed the χ^2 for a multinomial histogram,

$$\chi^2_m = 2 \sum_i n_i \; \ln\left(\frac{n_i}{y_i(\vec{\theta})}\right). \tag{5.10}$$

Since the χ^2_m equation (5.10) is constructed by making use of the likelihood ratio, it also follows asymptotically (for a large number of events in each bin) a χ^2-distribution.

As a consequence, we have the appropriate estimator regarding our experimental data. The parameters $\vec{\theta}$ that minimize χ^2_m equation (5.10) correspond to the best-fit

parameters. Although, we cannot interpret its value in terms of goodness of fit, because we cannot use its asymptotic behavior.

5.3   Goodness-of-fit test

In the previous section, we defined the likelihood, and we have seen that minimizing χ^2, we get the best fit parameters, which maximize $\mathcal{L}(H_0)$. In other words, we get the parameters which maximize the probability that the observed data are a random sample of our theoretical model.

However, so far we did not test the null hypothesis. To test an hypothesis, one needs to test it with respect to an alternative hypothesis H_1. When the alternative hypothesis is not specified, we talk about a goodness-of-fit test [46]. Because the χ^2 and χ^2_m in the previous section have been defined from the likelihood ratio of two hypothesis, where we used the saturated model as H_1 (the unspecified alternative hypothesis), χ^2 and χ^2_m can be used for goodness-of-fit test.

To explain how we can perform a goodness-of-fit test, we use χ^2 equation (5.6) for reasoning, but it applies in the same way to χ^2_m equation (5.10). We can interpret χ^2 as a distance between the model and the experimental data. The parameter set that minimizes this distance leads to the best fit, then we label the best fit parameter set $\vec{\theta}_{fit}$, and the associated χ^2 value $\chi^2_{exp,min}$.

Now, consider that our theoretical probability density function $\vec{p}(\vec{\theta}_{fit})$ is the true physical law followed by the experiment. We can generate a simulated experiment which follow $\vec{p}(\vec{\theta}_{fit})$, with the same total number of recorded atoms as in the real experiment N_{exp}. We call this simulated experimental result $\vec{n}_{sim}$. Then we minimize χ^2 with this simulated experiment, this gives us the best-fit parameters for this simulated experiment $\vec{\theta}_{sim}$, and the associated minimum χ^2 value $\chi^2_{sim,min}$. Thus we get a typical value of the minimum distance between our theoretical model and data obtained considering that the model is true. If we repeat the process for thousands of simulated experiments, we then get the distribution of the typical distance that one would observe if the experiment follows our theoretical model.

At the end, we compare the $\chi^2_{exp,min}$, with the distribution of the $\chi^2_{sim,min}$ obtained for thousands of simulated experiment, see figure 5.3. If the $\chi^2_{exp,min}$ (i.e. the distance between the model and the real experimental data) is much larger than the typical χ^2_{min} one would observe if the experiment follows our theoretical model, then the model is rejected. Otherwise, the model can not be rejected.
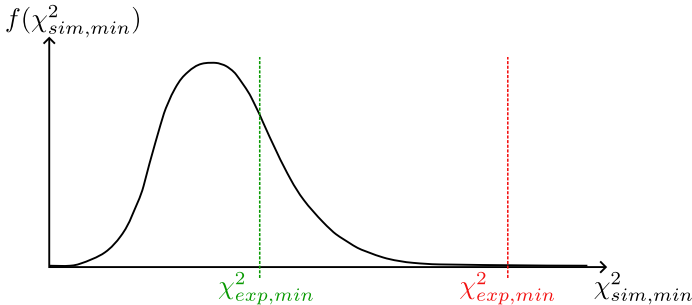
Figure 5.3: Illustration of the χ^2 distribution reconstruct by Monte-Carlo simulation (black, solid). In red (green) is represented a case where the $\chi^2_{exp,min}$ indicate to reject (not reject) the model.

By recording the best-fit parameters for the simulated experiment, we obtain a distribution, centered around $\vec{\theta}_{fit}$, and thus if the model is not rejected, one gets the statistical uncertainty on the parameters, see figure 5.4. A more complete explanation of goodness-of-fit test can be found in [44].
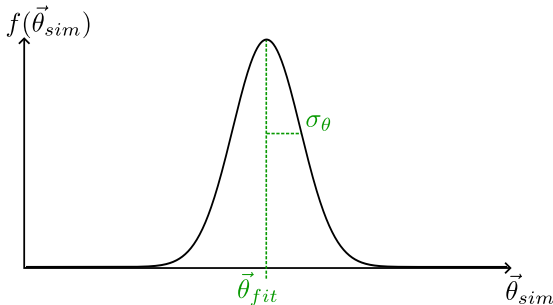
Figure 5.4: Parameter distribution centered around the best fit parameter (green), in the case where the model is not rejected.

5.3.1   Monte-Carlo Method

"The Monte Carlo method is a numerical technique for calculating probabilities and related quantities by using sequences of random numbers." [44].

We will make use of Monte-Carlo method to generate the simulated experiments. The Monte-Carlo method we used is von Neumann's acceptance-rejection method. The principle is illustrated figure 5.5.
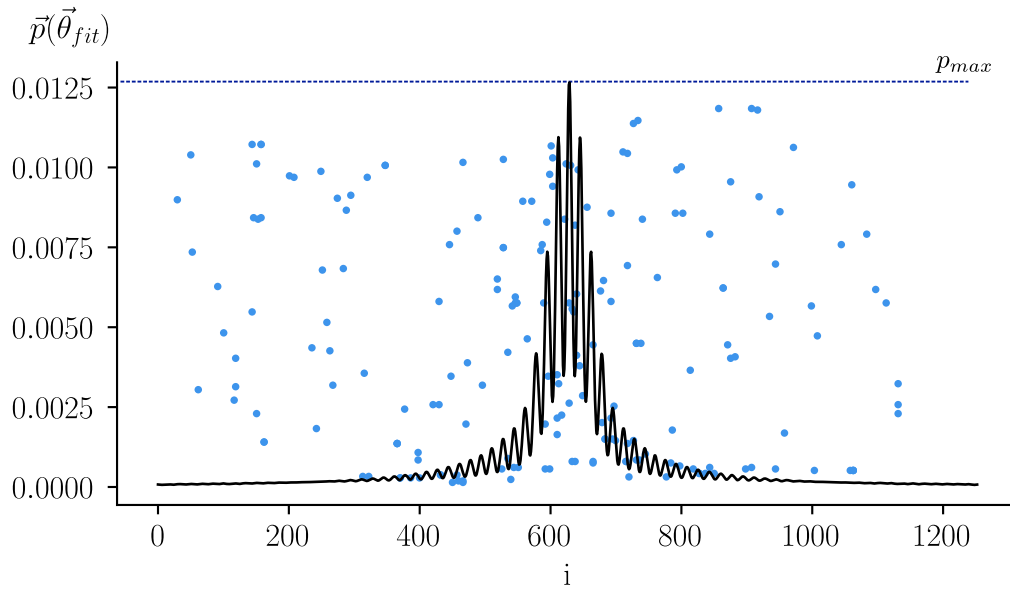
Figure 5.5: Illustration of the acceptance-rejection method

The algorithm is given in [44]. It consists of three steps :

1. Generate a random number i_{rnd}, uniformly distributed in $[1, N_x]$

2. Generate a random number u, uniformly distributed in $[0, p_{max}]$

3. if $u < p_{i_{rnd}}(\vec{\theta}_{fit})$ then i_{rnd} is accepted.

One has to repeat those three steps until the number of accepted events is the same as the total number of atoms in the real experiment. The Monte-Carlo method then enables us to generate simulated experiments such as the one plotted figure 5.6.
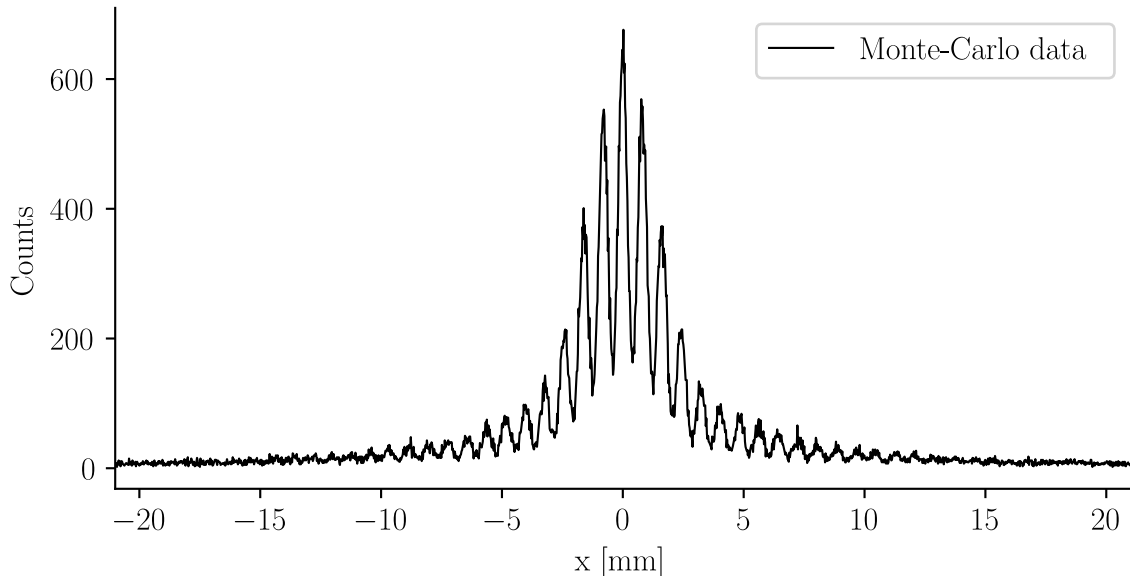
Figure 5.6: Simulated experiment obtained with the acceptance-rejection method

We now need to minimize χ_m^2 equation (5.10) for thousands of such simulated experiments, to obtain the distribution of $\chi_{m,min}^2$. A simulated experiment takes about 20 to 30 seconds to generate since we have $\sim 100\,000$ atoms in the real experimental data set. This computation time could be reduced by considering a more optimised area in which we generate random numbers, see [44]. When one speaks about Monte-Carlo simulations, one refers to the use of simulated experiments to give χ^2 and parameter distributions.

Comment on the signal binning :

As one can see from the expression of χ^2 and χ_m^2, their value will depend on the choice of the binning : N_x. Indeed, one can either increase the spatial resolution by increasing N_x, but then there are fewer atoms per bin, or reduce the spatial resolution by reducing N_x and thus increase the number of atoms per bin. As mentioned in [48] "Our experience is that in most experiments the number of bins is chosen too high".

Even if some rules have been proposed, there are no general rules for the choice of the binning. A usual advice is to use a binning which leads to a spatial resolution to be $1/10^{th}$ of a characteristic dimension. In our case, the characteristic dimension we take is the size of an interfringe. Hence, the resolution of all the experimental data (and simulated experiments) plotted so far is too high, and the binning has to be reduced by two, $N_x \to N_x/2$. All the goodness-of-fit test presented have been performed on the reduced binned data. Moreover we checked if the result of the test

was not changed by reducing and enlarging the binning.

When one has only one parameter, it is highly recommended to use a binning independent test such as the Kolmogorov-Smirnov test. In this test, we look for the smallest distance between the cumulative distribution function (CDF) of the model and the CDF of the experimental data, see [49]. One can also perform a goodness-of-fit test using Monte-Carlo, with the same approach as we presented for χ^2.

Comment on the choice of the χ^2 :

The importance of the choice of the χ^2, with respect to the data point distribution, might not appear clear. One could use the χ^2 equation (5.6) even for sample with low number of atoms, find the best fit parameter by minimizing the χ^2, and get the statistical uncertainty using Monte-Carlo simulations.

The problem comes from outliers. Outliers are data points which for different reasons (a defect in the detector, a source of local noise , etc.) are far apart from the rest of the signal. Outliers do not contribute in the same way depending on the χ^2 one uses. An outlier contributes more to the value of the usual χ^2 equation (5.6) than to the value of χ^2_m equation (5.10). This could lead to a poor estimation of the best-fit parameter and to an overestimation of the statistical uncertainty using Monte-Carlo method.

5.3.2   Results

5.3.2.1   1D time dependent Schrödinger equation model

Now we use everything we have presented to test the 1D-TDSE model. Here we only consider one parameter, the atom-surface interaction coefficient C_3. We still use the χ^2_m rather than the Kolmogorov-Smirnov test (which should be used since we only have one parameter) in preparation for future tests where we want to consider other parameters, e.g. the minimum atom-surface distance r_{min}, the slit size a_{slit} etc.

For the 1D-TDSE, for a single value of C_3, we have to remember that we need to consider two slit sizes, and for each slit size we have to run the simulation for eleven different propagation velocities. Therefore, to generate the 1D-TDSE results for hundreds of different values of C_3, we have to run the simulation 2200 times. Each simulation lasts $\sim$ one minute. This was done on the USPN's MAGI calculation cluster, taking $\sim$ 17 hours to generate the 2200 simulation results.

Finally, for experimental data at 19 m/s, minimizing χ^2_m equation (5.10) for $x \in [-24, 24]$ mm, the minimum value is $\chi^2_{exp,min} = 2197$, the associated best fit

parameter is $C_3 = 1.17$ a.u. For $x \in [-24, 24]$ mm, there are 999 bins, with a bin size of 0.048mm. From this best fit, i.e., the 1D-TDSE model with $C_3 = 1.17$ a.u, we generate the χ_m^2 distribution from 10 000 simulated experiments using the Monte-Carlo method. The χ_m^2 distribution is given figure 5.7.
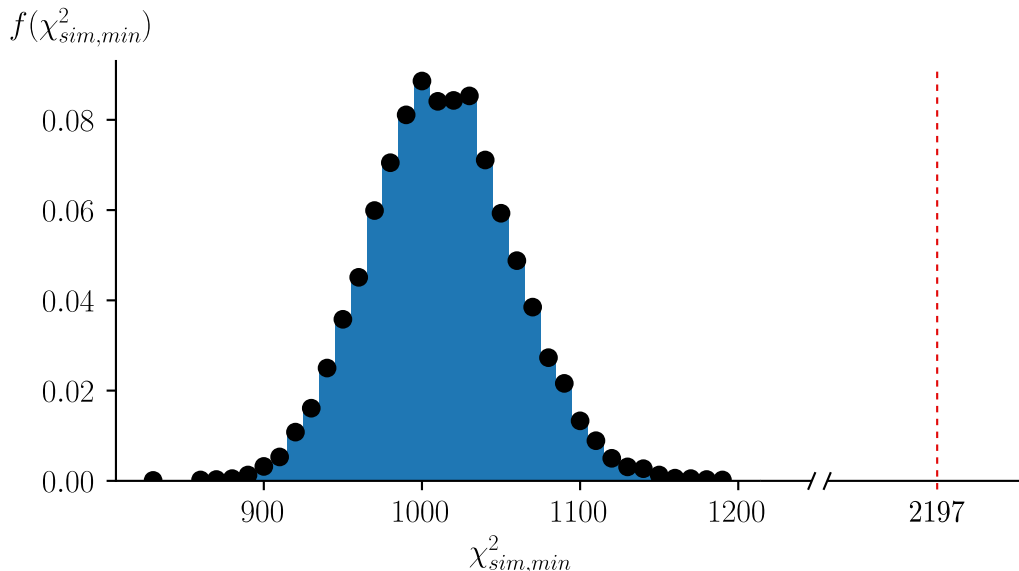
Figure 5.7: $\chi_{m,min}^2$ distribution obtained from the Monte-Carlo simulations, the red dashed line represents the value $\chi_{exp,min}^2$ obtained for the real observed experimental data.

Regarding the $\chi_{exp,min}^2 = 2197$ obtained for the real observed experimental data, our 1D-TDSE model is rejected. To reject a model or not, a quantity of interest is the P-value defined as,

$$P = \int_{\chi_{exp,min}^2}^{\infty} f_{\chi^2}(z)dz, \tag{5.11}$$

where f_{χ^2} is the χ^2 distribution, as plotted in figure 5.7. The P-value indicates that one would obtain a larger χ^2 than the one observed for the experimental data in $P \times 100$ % of the cases. The P-value used to reject a model is partly subjective, one often use the value $P = 0.001$, thus if $P < 0.001$ the model is rejected.

Here, the P-value would be much lower than 0.001. Actually for the 10 000 simulated experiments, none has a $\chi_{sim,min}^2$ value in the vicinity of $\chi_{exp,min}^2$. Therefore, it is not possible in our case to return any P-value.

The parameter distribution is plotted, figure 5.8a. What we see is that we obtain a normal distribution centered, as expected, around $C_3 = 1.17$ a.u (this is not a measure of the C_3 value since the model is rejected). Fitting the C_3 distribution with a Gaussian function $\propto \exp(-(C_3 - \overline{C}_3)^2/(2\sigma_{C_3}^2))$, one measures a standard

deviation $\sigma_{C_3} = 0.010$ a.u, which represent a 0.9 % statistical uncertainty.

In figure 5.8b, we performed exactly the same protocol, using the same experimental data, but with a reduced total number of atoms. Hence, the best fit is obtained for $C_3 = 1.15$ a.u. We also performed the Monte-Carlo method to generate 10 000 simulated experiment. What we observe is, now, the $\sigma_{C_3} = 0.019$ a.u, which represent a 1.7 % statistical uncertainty. This is consistent with what is expected from the central limit theorem, multiplying the total number of atoms by 3.7 the standard deviation is divided by $\sqrt{3.7}$.

Then, we can estimate that we need a total number of atoms of $\sim 7.2 \times 10^6$ to get a statistical uncertainty of ~ 0.1 %. This requires ~ 2880 hours ($= 120$ days) of data acquisitions. Therefore, it is necessary to increase the atomic flux in order to reach very low statistical uncertainty.

For huge total number of atoms detected, it is better to perform multiple short (few hours) data acquisition. The Ar* flux reduce after few hours because the magnetic field which focuses the electron to excite the atoms decrease along the day, so the signal to noise ratio also decrease. There are also other fluctuations for long period of data acquisition such as the laser beams intensities and polarizability. These fluctuations change the MOT size and so alter the angular beam distribution since we only have one slit to select the beam.

Note that the total number of atoms does not play a role in the goodness-of-fit test, the model is still rejected with the same distance between the Monte-Carlo χ^2 distribution and the $\chi^2_{exp,min}$.
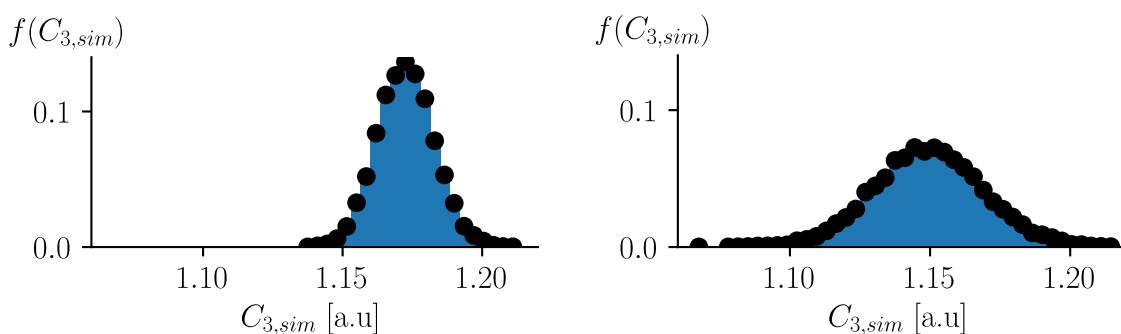
(a) C_3 distribution from the MC simulations for a total number of atoms $N_{exp} = 99708$

(b) C_3 distribution from the MC simulations for a total number of atoms $N_{exp} = 26862$

Figure 5.8: Parameter distribution for different total number of detected atoms

We performed the goodness-of-fit test for different x intervals to see if the model leads to better results when we do not go far in the tails of the diffracted pattern. We

find that the model is still rejected. Only the best-fit parameter C_3 is impacted when changing the interval x. We also compare the 1D-TDSE model to the experimental data at 26 m/s and the model is also rejected. In the case of the experimental data at 26 m/s, the $\chi^2_{exp,min}$ value is further to the $\chi^2_{sim,min}$ distribution than for the data at 19 m/s. This mean that the discrepancy between the 1D-TDSE model and the data decreases while decreasing the atom propagation velocity. This is probably related to the fact that we consider a uniform velocity distribution. For the same time of flight window (1 ms), we have a larger velocity distribution when the average velocity is higher.

5.3.2.2 Semi classical *vs* 1D-TDSE model

So far, we showed that the 1D-TDSE model is rejected for both experimental results (at 19 and 26 m/s), but what about the Semi-Classical model we used? What we do here is to construct a test statistic function of the experimental data set,

$$\lambda^{SC}_{Sch} = \frac{\mathcal{L}(H_0)}{\mathcal{L}(H_1)}, \tag{5.12}$$

where, on the one hand, the hypothesis H_0 is: $\vec{n}$ is a random sample of the semi-classical model. On the other hand, H_1 is : $\vec{n}$ is a random sample of the 1D-TDSE model. Making use of the likelihood ratio and the saturated model we can define

$$\begin{cases} (\chi^2_m)^{SC} & = -2\ln(\lambda^{SC}) \\ (\chi^2_m)^{Sch} & = -2\ln(\lambda^{Sch}). \end{cases} \tag{5.13}$$

λ^{SC} (λ^{Sch}) is the likelihood ratio between the semi-classical (1D-TDSE) model and the saturated model. Thus, we can rewrite $\lambda^{SC}_{Sch} = \lambda^{SC}/\lambda^{Sch}$ as

$$\lambda^{SC}_{Sch} = \exp\left(\frac{1}{2}\left((\chi^2_m)^{Sch} - (\chi^2_m)^{SC}\right)\right). \tag{5.14}$$

So, if $(\chi^2_m)^{Sch} < (\chi^2_m)^{SC}$ then $\lambda^{SC}_{Sch} < 1$, hence the 1D-TDSE model would better represent the experimental data set. Indeed, this is what we can observe for the experimental data set at 26 m/s, see table (5.1). There is no need to do this for the experimental data set at 19 m/s, as the semi-classical model cannot be used, as we explained section 3.2.3.

Therefore, the semi-classical model is also rejected, since it is less likely to represent the experimental data than the 1D-TDSE model, which is itself rejected.

x [mm]	$(\chi^2_{m,min})^{Sch}$	C_3^{Sch} [a.u]	$(\chi^2_{m,min})^{SC}$	C_3^{SC} [a.u]	$((\chi^2_{min})^{Sch}-(\chi^2_{min})^{SC})/2$
[-8,8]	1528	1.2705	1590	1.24242	-31
[-10,10]	1786	1.246	1890	1.20202	-52
[-12,12]	2084	1.2215	2438	1.15152	-177
[-15,15]	2438	1.1935	3444	1.09091	-503
[-20,20]	3238	1.155	5677	1.0202	-1220

Table 5.1: Results of the χ^2_m minimization for both models with respect to the experimental data at 26 m/s

Moreover we see that the more we include the tails of the diffraction pattern, the more the discrepancy between the models increase.

5.3.3 Possible issues

Here we discuss possible issues that have to be investigated to possibly get a better agreement between the 1D-TDSE model and the experimental data. We can separate this part in two, on the one hand, we have the theoretical issues and on the other hand, the experimental ones.

5.3.3.1 Theoretical issues

1- Atom-surface interaction potential

There are several things that can be corrected here. First, we have neglected the entrance and exit of the slit. Second, we should replace the modified Wylie and Sipe potential equation (4.16), by the complete numerically calculated Casimir-Polder potential. The minimum atom-surface distance r_{min} could also play a role since it affects the effective size of the slit.

2- Propagation axis

In the simulation, we consider that atoms propagate parallel to the surfaces. As we already mentioned in section 4.4, we should take into account the influence of the angular beam distribution on the wave function at the exit of the slit. This work is ongoing.

5.3.3.2 Experimental issues

1- Nanograting geometry

The measured nanograting geometry may be inaccurate. Estimated parameters may be subject to change due to systematic uncertainties in SEM imaging techniques. The geometrical characterization of the nanograting is the main limitation we have to present. By using the model and the asymmetry of the diffraction pattern when rotating the nanograting, it might be possible to better constrain the geometry of the nanograting.

2- Metastable Argon atoms

One disadvantage of working with metastable atoms is that they have a lot of internal energy. Thus, they can pull out electrons from different surfaces, and so the nanograting surfaces might not be neutral for a short period of time. This would modify the atom-surface interaction. The nanograting is connected to the ground, the charges evacuate quickly but possibly not quickly enough compared to the flux of metastable Argon atoms.

3- Detection

There might be some loss of detection efficiency in the tails of the diffracted patterns. The angle of atoms arriving on the detector could play a role. If there is such an effect of the incidence angle of the atoms on the detection efficiency in the tails, then the effect is smaller than what we are able to detect. The detected numbers of atoms are of the same order of magnitude in the tails on both sides.

5.3.3.3 Few simple trials

We tried to reduce the discrepancy between the theory and the experimental data, by implementing easy modifications of the model.

First, we tried to take into account both more propagation velocities (29 instead of 11), and more slit sizes for the stadium slit shape figure 2.21 (5 instead of 2). We did not get any significant improvement.

Second , for two slit sizes and eleven velocities, we tried to take into account the

geometry of the slit along the propagation axis figure 2.18. We can also take into account the rounded part of the potential in a 1D simulation. This is possible since we can use time dependent potential as we mentioned section 4.1. The modified atom-surface interaction potential equation (4.16) for the rounded slit is plotted figure 5.9. This did not lead to a better agreement between the model and the experimental data.
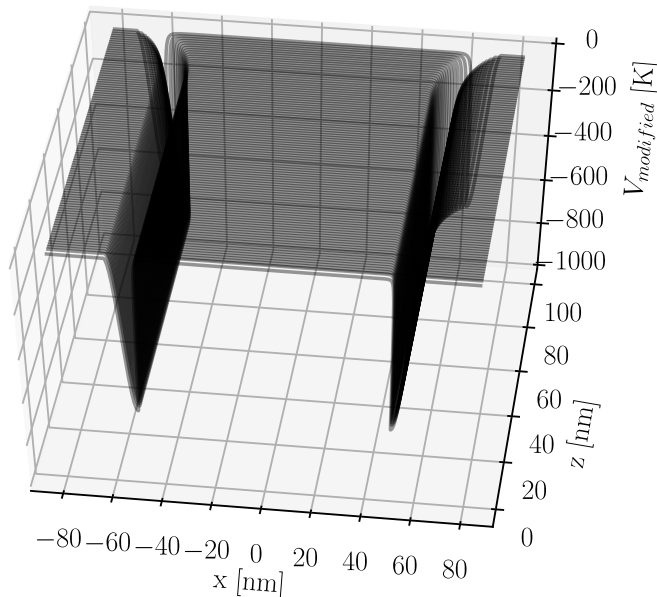
Figure 5.9: Modified Atom-surface potential, with rounded geometry at the exit of the slit.

Finally, we tried to change the main slit size. This means that we run the simulation considering a straight slit, we took into account eleven velocities and two slit sizes. But instead of taking 102.7 nm and 97.5 nm, we tried larger and smaller slit sizes. Reducing the slit size slightly reduced the minimum χ_m^2, and thus improved (a bit) the agreement between the model and the data. Although the model is still rejected, this indicates two possibilities. Either the slit sizes estimated from SEM images are larger than in reality and should be reduced. Or either we did not get the normal incidence in the experiment. This last assumption is not privileged because the nanograting would have to be rotated by 5.7° (for $a_{slit} = 102.7$ nm) with respect to the normal incidence for the apparent size of the slit to be reduced by 0.5 nm.

5.4 Remark about the detection noise

So far we mentioned possible lack of detection efficiency, but we did not discuss the counts due to detection noise. There are different sources of noise such as the electronic chain, temperature fluctuation, or possible ions or electrons present in the vacuum chamber. We now give orders of magnitude of the detection noise contribution to the experimental data sets. Let us assume that each count due to the detection noise is independent.

In an experiment when we do not push the atoms, all the counts on the detector arise from detection noise. The mean flux of the noise is ~ 30 Hz, distributed over the entire surface of the detector. The detector surface is a disk of radius 4 cm $S_{detector} = 50.27 \text{ cm}^2$, from which we select only the surface covered by the diffraction pattern, which is assimilated to a rectangle of surface $S_{pattern} = 8(\text{cm}) \times 0.1(\text{cm}) = 0.8 \text{ cm}^2$. Thus, the flux of counts due to noise in the diffracted pattern area is ~ 0.48 Hz. Moreover, we select atoms with respect to their arriving time of flight, and the time selection is a window of length 1 ms over 65 ms. Therefore, the flux of the noise in the experimental data presented in section 2.4 is $\sim 7.3 \times 10^{-3}$ Hz. For a 40 hours acquisition (approximately the time needed for the data set at 19 m/s), the total number of events due to detection noise is ~ 1063. This estimation is most probably lower than in reality. Because Ar* has enough energy to pull out electrons from surfaces, there could be more electrons in the vacuum chamber which could then possibly increase the detection noise.

To get a better estimation of the detection noise, we should run the experiment, and push the atoms, while obstructing the nanograting.

The reason we did not take the detection noise into account is illustrated figure 5.10. We see that the best-fit model predicts a higher number of events in the tails than detected. This is why we are first looking for a lack of detection efficiency. However, for future analysis, the dark noise will have to be modeled and added to the theoretical model.
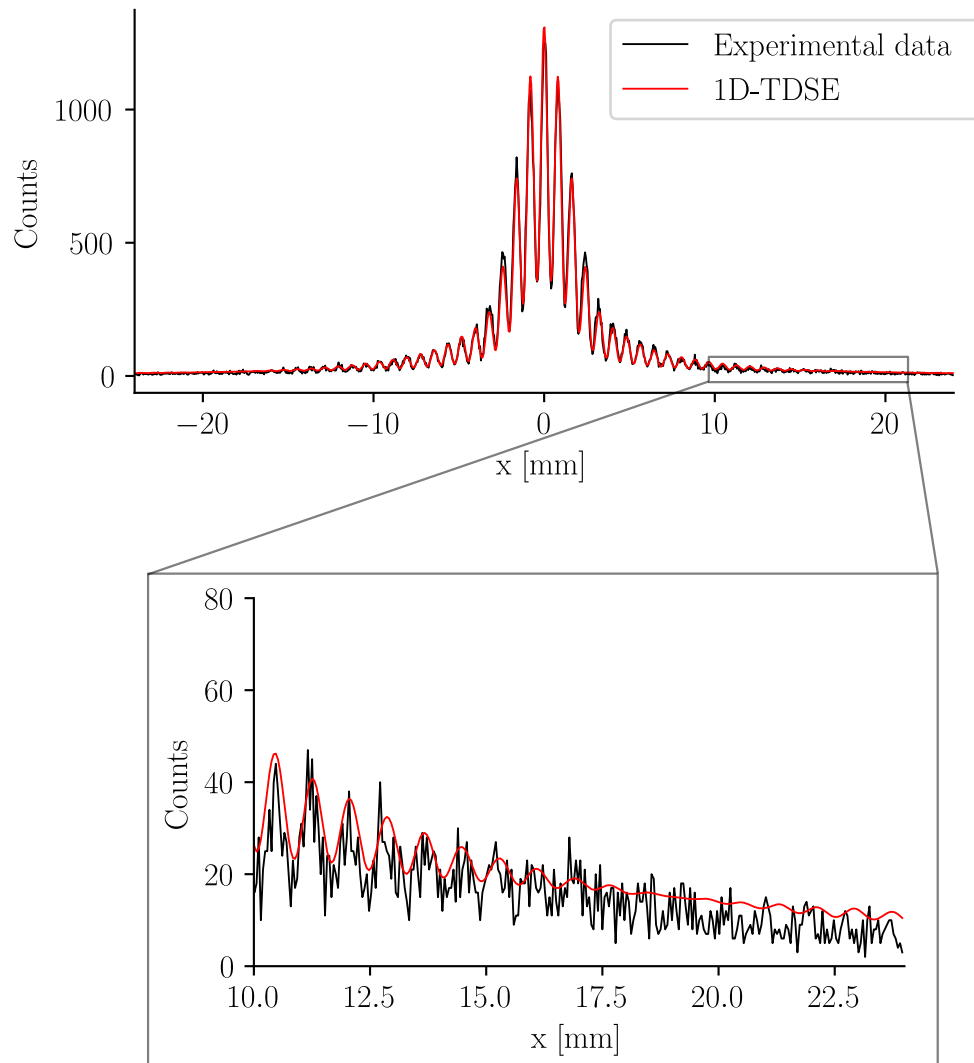
Figure 5.10: 1D-TDSE best fit (red) and experimental data at 19m/s (black). The binning has been chosen such that the spatial resolution is $dx = 0.048$ mm (total of 999 bins).

5.5 Statistical data analysis summary

1. We recalled the origin of the χ^2 minimization to find the maximum likelihood and thus the best-fit parameters.

2. Our experimental data sets correspond to multinomial histograms.

3. One has to be careful while choosing the appropriate estimators regarding how its experimental data points are distributed.

4. We give the adapted χ^2_m one should use to find the maximum likelihood for a multinomial histogram.

5. Regarding to the low number of atoms detected in the bins in the tails of the diffracted patterns, we had to perform Monte-Carlo simulations to reconstruct the χ^2_m distributions.

6. The goodness-of-fit test showed that both the 1D-TDSE (chapter 4) and semi-classical (chapter 3) model are rejected. But for different reasons, for the 1D-TDSE model, it seems that we are limited by experimental issues, while for the semi-classical model, the theoretical approach itself is the limiting factor.

7. Even if both models are rejected we proved that the 1D-TDSE model better represents the experimental data than the semi-classical one.

Conclusion

The experiment reviewed in this thesis has been designed in order to perform an accurate measurement of the Casimir-Polder potential. The experimental technique is based on the diffraction of a slow atomic beam of Ar^* using a Si_3N_4 nanograting. The main benefits of such choices are the following. First, the atoms do not stick to the diffracting structure and so do not alter its geometry during the data acquisition. Second, the use of slow atoms increases the interaction time between the atom and the surface of the nanograting. Thus, the atom-surface interactions become predominant in the diffraction pattern.

In chapter 3, we interpreted the experimental data at 26 m/s with a semi-classical model. This enabled us to show that the experimental setup is already sensitive enough to discern phenomena such as retardation effects for an atom surface distance less than 51 nm. However, the semi-classical model was not adapted for the experimental data at 19 m/s. This led us to develop a new model which relies on the numerical solution of the 1D time-dependent Schrödinger equation, see chapter 4.

Using statistical tools that are adapted to the distribution of the experimental data points, see chapter 5, we performed goodness-of-fit tests. This led us to reject both of the presented models (semi-classic and 1D-TDSE). Although not for the same reasons. For the semi-classical model, the underlying assumptions are very strong compared to the experimental data, while the 1D-TDSE model is more sensitive to different experimental parameters. The rejection of the 1D-TDSE model means that either physical phenomenon are not taken into account or some experimental parameters were not controlled with sufficient precision. However, we have shown that the 1D-TDSE model is closer to the experimental data than the semi-classical one. The major limitations of this TDSE model are related to the 1D representation, therefore, it is not straightforward to add any angular dependence in this model.

Among all the strengths of this experiment, there are still some weaknesses that

need to be addressed. For example, the atomic flux is very low and so makes it difficult to reach atom propagation velocities lower than 15 m/s. This low flux also deteriorates the signal-to-noise ratio. The use of argon atoms in a metastable state increases the electronic noise in the experiment and can possibly charge the surfaces of the nanograting.

We have observed experimentally that there is a strong influence of the orientation of the nanograting with respect to the atomic beam propagation axis. When the orientation angle is changed, the amplitude of the interference orders changes, and thus the diffraction pattern becomes asymmetric. So far we have not been able to reproduce such results in the theoretical models. However, this effect could be used to perform a tomographic study, and so help in characterizing the nanograting geometry. The orientation angle is a parameter which can be controled with high precision thanks to the use of the hexapod from SmarAct company.

It is important to keep in mind that the nanograting is the cornerstone of this experiment. The nanograting we used was developed in the OIA group to perform Casimir-Polder potential measurements. We characterized the nanograting geometry using SEM images. However, because of the strong interdependence of the atom-surface interaction and the geometry of the nanograting, it is necessary to gain in precision for the geometric characterization of the nanograting. We get the same theoretical diffracted pattern when we use a large C_3 and large a_{slit}, or a small C_3 and small a_{slit}. Thus, finding an independent method for geometry characterization, such as using an atomic force microscope (AFM), would be helpful. Furthermore, it would be of great interest to study the optical properties of the nanograting, especially for high-energy photons.

Finally, in the near future, the models would have to be modified to account for the orientation angle dependence. Experimental parameters such as the angular distribution of the beam or the location of the nanograting in the beam must be controlled with better accuracy. A tomographic study would enable one to possibly decorrelate the geometry of the nanograting and the atom-surface interaction in the diffracted patterns.

Appendix A

Atom-surface interaction coefficients

In this appendix, we review the calculation of the atom-surface interaction coefficient. We first remind some properties of generalized susceptibility. Second, we present how we calculated the atom surface interaction coefficient in the non retarded regime. Finally we give the coefficient in the retarded regime. Further information and calculation techniques can be found in [5].

A.1   Generalised susceptibility

Atom-surface interaction rely on the response of both the atom and the surface to an electromagnetic excitation. In linear response theory, one defines the general susceptibility which we write α and depend on the frequency of the electromagnetic excitation.

Here we give some of the properties of generalised susceptibility, one can find derivation of those properties and more information on linear response theory in [50].

In general, α is a complex function,

$$\alpha(\omega) = \alpha'(\omega) + i\alpha''(\omega). \tag{A.1}$$

One can find general properties of the susceptibility by making use of the theory of the complex variable. Let $\omega = \omega' + i\omega''$, then one can show that

$$\alpha(-\omega^*) = \alpha(\omega)^*, \tag{A.2}$$

it follows that for ω purely imaginary

$$\alpha(i\omega) = \alpha(i\omega)^*. \tag{A.3}$$

We see from equation (A.3), that on the imaginary axis, α is real. In [50] we can find the following theorem regarding generalized susceptibility : on the upper imaginary axis the real function α decreases monotonically from a positive value to zero for $\omega \rightarrow i\infty$.

A.2 Non retarded : C_3

We are interested in calculating the Lifshitz atom-surface interaction coefficient

$$C_3 = \frac{\hbar}{16\pi^2\epsilon_0} \int_0^\infty \alpha(i\omega)\frac{\epsilon(i\omega) - 1}{\epsilon(i\omega) + 1}d\omega, \tag{A.4}$$

which was first given in [2], and where α is the atomic dynamic polarizability, and ϵ the dielectric permittivity of the surface. It is important to keep in mind that, $\alpha(i\omega)$ and $\epsilon(i\omega)$ are real for $\omega \rightarrow i\infty$, as we mentioned earlier.

A.2.1 Dynamic polarizability α

The dynamic polarizability is given by

$$\alpha(\omega) = \frac{e^2}{m} \sum_n \frac{f_n}{\omega_n^2 - \omega^2 - i\omega\gamma_n}, \tag{A.5}$$

where γ_n is the energy level n linewidth, ω_n is the pulsation associated with the transition to the energy level n. f_n is the oscillator strength, which can be rewritten by making use of the Einstein A_n coefficient for spontaneous emission. More information on dynamic polarizability can be found in [51]. The dynamic polarizability on the positive imaginary axis is

$$\alpha(i\omega) = 2\pi\epsilon_0 c_0^3 \sum_n \frac{A_n}{\omega_n^2(\omega_n^2 + \omega^2)}. \tag{A.6}$$

There are seventeen transitions referenced in the NIST database for the Ar* in the $^3P_2$ state, see [29]. In the case where the surface is a perfect conductor ($\epsilon(i\omega) \rightarrow \infty$),

$$C_{3,perfect} = \frac{\hbar}{16\pi^2\epsilon_0} \int_0^\infty \alpha(i\omega)d\omega \approx 2.23 \text{ a.u.,} \tag{A.7}$$

for Ar* atoms.

A.2.2 Dielectric permittivity of the surface

We write the susceptibility of the surface as

$$\epsilon(\omega) = \epsilon_1(\omega) + i\epsilon_2(\omega), \tag{A.8}$$

it is related to the optical refractive index n and absorption coefficient k by

$$\epsilon(\omega) = (n(\omega) + ik(\omega))^2, \tag{A.9}$$

which leads to

$$\begin{cases} \epsilon_1(\omega) = n(\omega)^2 - k(\omega)^2 \\[2mm] \epsilon_2(\omega) = 2n(\omega)k(\omega). \end{cases} \tag{A.10}$$

Then, one can make use of the Kramers-Kronig relation,

$$\epsilon_1(\omega) = 1 + \frac{2}{\pi}\mathcal{P}\int_0^\infty \frac{t\epsilon_2(t)}{t^2 - \omega^2}dt, \tag{A.11}$$

where $\mathcal{P}$ means principal part.

In equation (A.4) we are interested on purely imaginary frequencies, and since the susceptibility is real on the upper imaginary axis we can write

$$\epsilon(i\omega) = \epsilon_1(i\omega) = 1 + \frac{2}{\pi}\int_0^\infty \frac{t\epsilon_2(t)}{t^2 + \omega^2}dt. \tag{A.12}$$

The problem here is that we need an analytical expression for ϵ_2 and the optical properties for all frequencies from 0 to ∞.

Optical properties for Si_3N_4 : from 290 nm to 30 μm

The optical data come from [33] where they measured the optical properties of Si_3N_4 for optical wavelength from 290 nm to 30 μm. We use the Tauc-Lorentz model proposed in [52] to fit the measured ϵ_2,

$$\epsilon_{2,IR}(\omega) = \Theta(\omega - E_{g1})\sum_j \frac{A_1 E_{j,1}\Gamma_1(\omega - E_{g1})^2}{((\omega^2 - E_{j,1}^2)^2 + \Gamma_1^2\omega^2)\omega} \tag{A.13}$$

where we sum over the resonances. Θ is the Heaviside step function and the IR index means that we don't have the response in the UV so far. Data and fit are plotted in figure A.1.
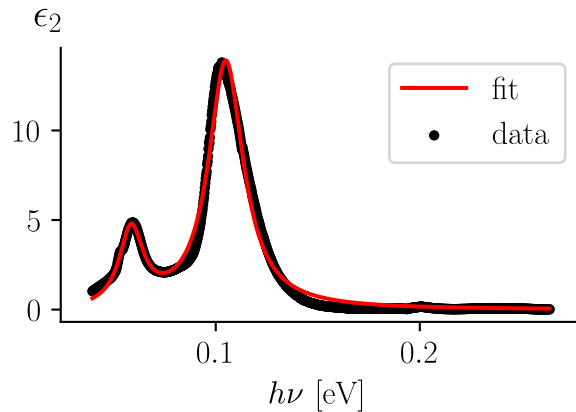
Figure A.1: Optical data (black, dotted), and the Tauc-Lorentz fit (red, solid)

Optical properties for Si_3N_4 : from 50 nm to 250 nm

The optical data come from [53]. We also make use of the Tauc-Lorentz model but for only one resonance,

$$\epsilon_{2,UV}(\omega) = \Theta(\omega - E_g)\frac{AE_0\Gamma(\omega - E_g)^2}{((\omega^2 - E_0^2)^2 + \Gamma^2\omega^2)\omega}. \tag{A.14}$$

Both data and fit are plotted figure A.2.
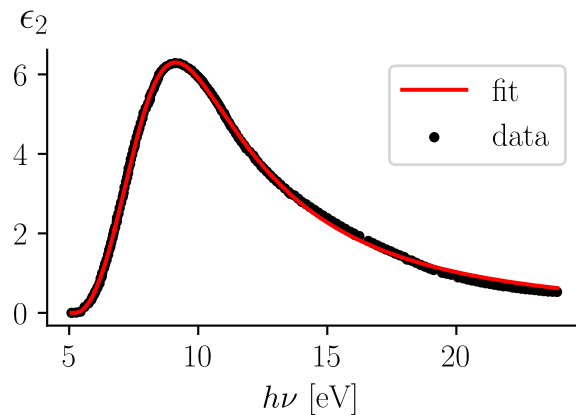
Figure A.2: Optical data (black, dotted), and the Tauc-Lorentz fit (red, solid)

Now, combining equation (A.13) and (A.14) we have the analytical expression for $\epsilon_2(\omega) = \epsilon_{2,IR}(\omega) + \epsilon_{2,UV}(\omega)$, for a wide range of frequencies. Thus, by making use of the Kramers-Kronig relation equation (A.12), we finally can calculate the non-retarded atom-surface interaction coefficient $C_3^{Si_3N_4} \approx 1.25$ a.u.

The accuracy of the C_3 coefficient depends on the optical properties measurements of the Si_3N_4 see discussion in section 3.2.2.

A.3   Retarded : C_4

The atom-surface interaction coefficient in the retarded regime for a perfect conductor is given (see [5]) by

$$C_4^{perfect} = \frac{3\hbar c_0 \alpha(0)}{2(4\pi)^2 \epsilon_0} \approx 5216.45 \text{ a.u.} \tag{A.15}$$

where $\alpha(0) = \alpha(i\omega = 0)$ is the static polarizability of the atom.

In the case of a dielectric surface, the retarded atom-surface interaction coefficient is given by

$$C_4^{dielectric} = \frac{3\hbar c_0 \alpha(0)}{2(4\pi)^2 \epsilon_0} \frac{\epsilon(0) - 1}{\epsilon(0) + 1} \approx 3989.05 \text{ a.u.} \tag{A.16}$$

where $\epsilon(0) = \epsilon(i\omega = 0)$, computed in section A.2.2 for Si_3N_4.

A.4   Core effect

It is important to keep in mind that we have a multielectron atom, therefore, we have to estimate the contribution of the core electrons to the atom-surface interactions. To do so, we do the same calculation as before, but consider the dynamic polarizability of the first ionic state. In front of a Si_3N_4 surface, the interaction coefficient for the first ionic state is $C_3 \approx 0.03$ a.u. This means that the core effect increases the atom-surface interaction coefficient by 2.4 %. For the moment it is negligible compared to the systematic uncertainties we have, but should be taken into account in the future.

Appendix B

From 1 to N slit diffraction

In this appendix, we will see that in atom optics, the diffraction pattern from a grating is obtained from the diffraction by a single slit multiplied by an analytic function that is the same as in classical optics.

B.1   Calculation

B.1.1   General case

The following calculations are based on those presented in [54] for an arbitrary grating in classical optics. Here, we will consider the possibility of adding an angle between the grating plane and the propagation axis. We observe an asymmetry in the intensity of the interference orders when the nanograting plane is not normal to the atom propagation axis. The problem is represented in figure B.1.
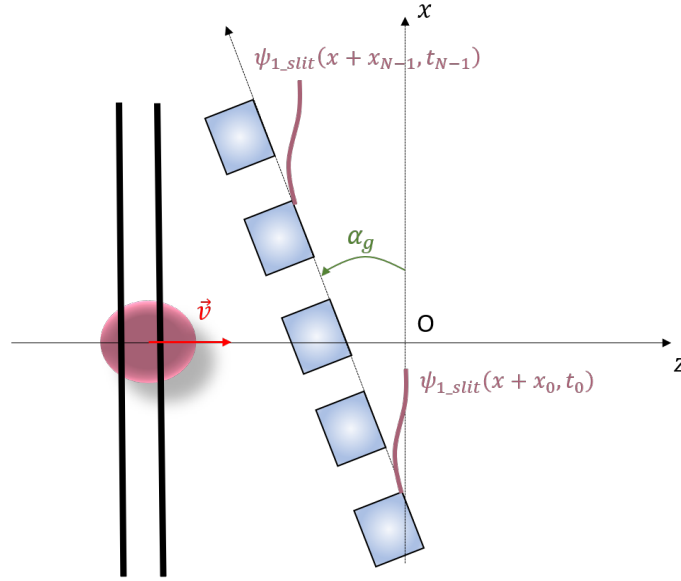
Figure B.1: Representation of the diffraction from a nanograting. Black lines symbolise the incident wave packet associated to the Ar* atom as plane wave with velocity v. Pink lines represent the wave function outgoing from each slits.

The parameters of the nanograting are :

$$\begin{cases} N & : \text{ total number of slits} \\ p_g & : \text{ grating period} \\ L_g & : \text{ length of the grating } (=(N\text{-}1)p_g) \end{cases} \quad \text{(B.1)}$$

We now want to express the coordinates of each slit. We first express the x-coordinate of the two extreme slits :

$$\begin{cases} n = 0 & \longrightarrow x_0 = -\frac{L_g}{2}\cos(\alpha_g) \\ n = N - 1 & \longrightarrow x_{N-1} = +\frac{L_g}{2}\cos(\alpha_g) \end{cases} \quad \text{(B.2)}$$

The x-coordinate of the slit n is given by :

$$x_n = x_0 + n p_g \cos(\alpha_g) \quad \text{(B.3)}$$

We do the same for the z-coordinate of each slit, the two extremities are given by :

$$\begin{cases} n = 0 & \longrightarrow z_0 = 0 \\ n = N - 1 \longrightarrow z_{N-1} = -L_g \sin(\alpha_g) \end{cases} \quad \text{(B.4)}$$

Thus, the z-coordinate of the nth slit is given by $z_n = -n p_g \sin(\alpha_g)$. Rather than using the z-coordinate, we will use the propagation time for the wave function outgoing from the slit n to reach the plane $z = 0$ (see figure B.1), this time delay is given by :

$$t_n = n \frac{p_g}{v} \sin \alpha_g \tag{B.5}$$

We set the initial time for the free propagation from the grating to the detector $t_{initial} = 0$, so the wave function in the plane $z = 0$ is given by the sum of the wave function outgoing from each slit (taking into account the propagation time to reach the plane $z = 0$ for all wave functions):

$$\psi(x, 0) = \sum_n \psi_{1\_slit}(x + x_n, t_n) \tag{B.6}$$

Regarding figure B.1, one can assume that all slits are independent (no tunneling). Thus, the wave function outgoing from one slit is the same for all slits, but at coordinates (x_n, z_n). Therefore, one can write the total wave function in momentum space as :

$$\tilde{\psi}(k, 0) = \sum_n \tilde{\psi}_{1\_slit}(k, 0) e^{ikx_n} e^{-\frac{i\hbar k^2}{2m} t_n} \tag{B.7}$$

$$\tilde{\psi}(k, 0) = \tilde{\psi}_{1\_slit}(k, 0) \sum_n e^{ik\left(x_n - \frac{\hbar k}{2m} t_n\right)} \tag{B.8}$$

replacing x_n and t_n by the expression given in (B.3) and (B.5) one gets :

$$\tilde{\psi}(k, 0) = \tilde{\psi}_{1\_slit}(k, 0) e^{ikx_0} \underbrace{\sum_n \exp(in \overbrace{(kp_g \cos(\alpha_g) - \frac{\hbar k^2}{2m} \frac{p_g}{v} \sin(\alpha_g))}^{A})}_{S}. \tag{B.9}$$

We will keep A as defined in (B.9) as long as possible in order to ease the calculations. S is a geometric series :

$$S = \sum_{n=0}^{N-1} \left(e^{iA}\right)^n = \frac{1 - e^{iAN}}{1 - e^{iA}} = \frac{e^{i\frac{AN}{2}}\left(e^{-i\frac{AN}{2}} - e^{+i\frac{AN}{2}}\right)}{e^{i\frac{A}{2}}\left(e^{-i\frac{A}{2}} - e^{+i\frac{A}{2}}\right)}, \tag{B.10}$$

we get :

$$S = e^{iA\left(\frac{N-1}{2}\right)} \frac{\sin\left(A\frac{N}{2}\right)}{\sin\left(\frac{A}{2}\right)}. \tag{B.11}$$

Hence equation (B.9) can be rewritten :

$$\tilde{\psi}(k, 0) = \tilde{\psi}_{1\_slit}(k, 0) e^{ikx_0} e^{iA\left(\frac{N-1}{2}\right)} \frac{\sin\left(A\frac{N}{2}\right)}{\sin\left(\frac{A}{2}\right)}. \tag{B.12}$$

We now need to propagate the wave function during a propagation time T, in order to obtain the wave function on the detector,

$$\tilde{\psi}(k,T) = \tilde{\psi}_{1\_slit}(k,0)e^{ikx_0}e^{iA\left(\frac{N-1}{2}\right)}\frac{\sin\left(A\frac{N}{2}\right)}{\sin\left(\frac{A}{2}\right)}e^{-i\frac{\hbar k^2}{2m}T}, \qquad (B.13)$$

keeping in mind that A depends on k, see equation (B.9), we have the wave function at the detector simply by taking the inverse Fourier transform of equation (B.13).

B.1.2 Stationary phase approximation

The distance between the detector and the nanograting is large, so the propagation time is long, under this condition one can use the stationary phase approximation, see [39].
In this approximation, the wave function on the detector is given by :

$$\psi(x,T) \approx \sqrt{\frac{m}{\hbar T}}\tilde{\psi}\left(-\frac{mx}{\hbar T},0\right)e^{i\frac{mx^2}{2\hbar T}}e^{-i\frac{\pi}{4}}, \qquad (B.14)$$

where T is the propagation time between the grating and the detector. In the case of a single slit, the probability density will be given by

$$|\psi_{1\_slit}(x,T)|^2 \approx \frac{m}{\hbar T}\left|\tilde{\psi}_{1\_slit}\left(-\frac{mx}{\hbar T},0\right)\right|^2, \qquad (B.15)$$

In the case of the total wave function outgoing from the grating, one has to use equation (B.13) in (B.14), and then taking directly the square modulus, one gets:

$$|\psi(x,T)|^2 \approx \frac{m}{\hbar T}\left|\tilde{\psi}_{1\_slit}\left(-\frac{mx}{\hbar T},0\right)\right|^2\frac{\sin^2\left(A\frac{N}{2}\right)}{\sin^2\left(\frac{A}{2}\right)}, \qquad (B.16)$$

with A calculated for $k = k_{stationnary} = -\frac{mx}{\hbar T}$.

Recognizing in (B.16) the diffraction by a single slit given in (B.15), we also replace A by its expression (see equation (B.9)). Finally, the square modulus of the wave function on the detector is given by :

$$|\psi(x,T)|^2 \approx |\psi_{1\_slit}(x,T)|^2\frac{\sin^2\left(\frac{mp_g\cos(\alpha_g)}{2\hbar T}Nx + \frac{mp_g\sin(\alpha_g)}{4\hbar T^2 v}Nx^2\right)}{\sin^2\left(\frac{mp_g\cos(\alpha_g)}{2\hbar T}x + \frac{mp_g\sin(\alpha_g)}{4\hbar T^2 v}x^2\right)}. \qquad (B.17)$$

In equation (B.17), terms in $\sin(\alpha_g)$ have negligible effects, no asymmetries in the interference orders are introduced by the angle α_g. The angle α_g only manifests as reducing the grating period by a factor $\cos(\alpha_g)$.

Bibliography

[1] H. B. G. Casimir and D. Polder, Phys. Rev. **73**, 360 (1948).

[2] E. M. Lifshitz, Soviet Phys. JETP **Vol: 2** (1956).

[3] D. Bloch and M. Ducloy, *Advances in atomic, molecular, and optical physics*, Vol. 50 (Academic Press, 2005), pp. 91–154.

[4] A. Laliotis, B.-S. Lu, M. Ducloy, and D. Wilkowski, AVS Quantum Sci. **3**, 043501 (2021).

[5] D. Dalvit, P. Milonni, D. Roberts, and F. d. Rosa, *Casimir physics* (Springer, 2011).

[6] S. Y. Buhmann, *Dispersion forces I: macroscopic quantum electrodynamics and ground-state casimir, casimir–polder and van der waals forces* (Springer, 2013).

[7] S. Y. Buhmann, *Dispersion forces II: many-body effects, excited atoms, finite temperature and quantum friction* (Springer, 2013).

[8] C. I. Sukenik, M. G. Boshier, D. Cho, V. Sandoghdar, and E. A. Hinds, Phys. Rev. Lett. **70**, 560 (1993).

[9] D. M. Harber, J. M. Obrecht, J. M. McGuirk, and E. A. Cornell, Phys. Rev. A **72**, 033610 (2005).

[10] S. Lepoutre, H. Jelassi, V. P. A. Lonij, G. Trénec, M. Büchner, A. D. Cronin, and J. Vigué, EPL **88**, 20002 (2009).

[11] J. D. Perreault and A. D. Cronin, Phys. Rev. Lett. **95**, 133201 (2005).

[12] R. E. Grisenti, W. Schöllkopf, J. P. Toennies, G. C. Hegerfeldt, and T. Köhler, Phys. Rev. Lett. **83**, 1755 (1999).

[13] R. Brühl, P. Fouquet, R. E. Grisenti, J. P. Toennies, G. C. Hegerfeldt, T. Köhler, M. Stoll, and C. Walter, EPL **59**, 357 (2002).

[14] J. D. Perreault, A. D. Cronin, and T. A. Savas, Phys. Rev. A **71**, 053612 (2005).

[15] A. Landragin, J.-Y. Courtois, G. Labeyrie, N. Vansteenkiste, C. I. Westbrook, and A. Aspect, Phys. Rev. Lett. **77**, 1464 (1996).

[16] H. Bender, P. W. Courteille, C. Marzok, C. Zimmermann, and S. Slama, Phys. Rev. Lett. **104**, 083201 (2010).

[17] J. M. Obrecht, R. J. Wild, and E. A. Cornell, Phys. Rev. A **75**, 062903 (2007).

[18] T. Taillandier-Loize, "Jet lent d'atomes d'argon métastables pour l'étude de l'échange de métastabilité, des interactions de van der Waals et des milieux d'indice négatif.", PhD thesis (Université Paris-Nord - Paris XIII, Dec. 9, 2014).

[19] J. Grucker, "Expériences d'optique atomique cohérente ou non avec un jet superfin d'atomes métastables de gaz rares", PhD thesis (Université Paris-Nord - Paris XIII, Dec. 2007).

[20] T. Taillandier-Loize, S. A. Aljunid, F. Correia, N. Fabre, F. Perales, J. M. Tualle, J. Baudon, M. Ducloy, and G. Dutier, J. Phys. D: Appl. Phys. **49**, 135503 (2016).

[21] F. Correia, "Jet lent d'atomes d'argon métastable pour l'étude de la diffraction au travers de nanoréseaux et de l'interaction avec des champs magnétiques co-mobiles", PhD thesis (Université Sorbonne Paris Cité, July 12, 2018).

[22] H. B. Tazi, "Nano-fabrication de réseaux membranaires en Si3N4 pour des applications aux ondes de matière", PhD thesis (Université Paris-Nord - Paris XIII, Dec. 16, 2019).

[23] C. R. Ekstrom, D. W. Keith, and D. E. Pritchard, Appl. Phys. B **54**, 369 (1992).

[24] L. D. Landau and E. M. Lifshitz, *Quantum mechanics: non-relativistic theory* (Elsevier, 2013).

[25] F. W. Byron and C. J. Joachain, Phys. Rep. **34**, 233 (1977).

[26] M. Born and E. Wolf, *Principles of optics: electromagnetic theory of propagation, interference and diffraction of light* (Elsevier, 2013).

[27] J. M. Wylie and J. E. Sipe, Phys. Rev. A **30**, 1185 (1984).

[28] J. M. Wylie and J. E. Sipe, Phys. Rev. A **32**, 2030 (1985).

[29] A. Kramida, Yu. Ralchenko, J. Reader, and and NIST ASD Team, NIST Atomic Spectra Database (ver. 5.9), [Online]. Available: `https://physics.nist.gov/asd` [2022, October 4]. National Institute of Standards and Technology, Gaithersburg, MD. 2021.

[30] W. H. Press, S. A. Teukolsky, W. T. Vetterling, and B. P. Flannery, *Numerical recipes 3rd edition: the art of scientific computing* (Cambridge University Press, 2007).

[31] E. A. Hinds and V. Sandoghdar, Phys. Rev. A **43**, 398 (1991).

[32] S. Zollner and E. Apen, AIP Conference Proceedings **550**, 532 (2001).

[33] K. Luke, Y. Okawachi, M. R. E. Lamont, A. L. Gaeta, and M. Lipson, Opt. Lett., OL **40**, 4823 (2015).

[34] M. D. Feit, J. A. Fleck, and A. Steiger, J. Comput. Phys. **47**, 412 (1982).

[35] C. Leforestier, R. H. Bisseling, C. Cerjan, M. D. Feit, R. Friesner, A. Guldberg, A. Hammerich, G. Jolicard, W. Karrlein, H. .-. Meyer, N. Lipkin, O. Roncero, and R. Kosloff, J. Comput. Phys. **94**, 59 (1991).

[36] U. Peskin, R. Kosloff, and N. Moiseyev, J. Chem. Phys. **100**, 8849 (1994).

[37] D. E. Miller, J. R. Anglin, J. R. Abo-Shaeer, K. Xu, J. K. Chin, and W. Ketterle, Phys. Rev. A **71**, 043615 (2005).

[38] C. Cohen-Tannoudji, B. Diu, and F. Laloe, *Quantum mechanics, volume 1* (Wiley-VCH, 1977).

[39] L. Mandel and E. Wolf, *Optical coherence and quantum optics* (Cambridge University Press, 1995).

[40] R. Kosloff and D. Kosloff, J. Comput. Phys. **63**, 363 (1986).

[41] J. W. Goodman, *Statistical optics* (John Wiley & Sons, 2015).

[42] P. Virtanen, R. Gommers, T. E. Oliphant, M. Haberland, T. Reddy, D. Cournapeau, E. Burovski, P. Peterson, W. Weckesser, J. Bright, S. J. van der Walt, M. Brett, J. Wilson, K. J. Millman, N. Mayorov, A. R. J. Nelson, E. Jones, R. Kern, E. Larson, C. J. Carey, İ. Polat, Y. Feng, E. W. Moore, J. VanderPlas, D. Laxalde, J. Perktold, R. Cimrman, I. Henriksen, E. A. Quintero, C. R. Harris, A. M. Archibald, A. H. Ribeiro, F. Pedregosa, P. van Mulbregt, and SciPy 1.0 Contributors, Nature Methods **17**, 261 (2020).

[43] A. Maury, M. Donaire, M.-P. Gorza, A. Lambrecht, and R. Guérout, Phys. Rev. A **94**, 053602 (2016).

[44] G. Cowan, *Statistical data analysis* (Oxford University Press, 1998).

[45] S. Baker and R. D. Cousins, Nucl. Instrum. Methods Phys. Res. **221**, 437 (1984).

[46] R. D. Cousins, *On goodness-of-fit tests*, Lecture at the University of California, 2016.

[47] F. James, *Statistical methods in experimental physics (2nd edition)* (World Scientific Publishing Company, 2006).

[48] B. Aslan and G. Zech, *Comparison of different goodness-of-fit tests*, arXiv: math/0207300, 2002.

[49] D. Taupin, *Probabilities, data reduction and error analysis in the physical sciences* (Éd. de Physique, 1988).

[50] L. D. Landau and E. M. Lifshitz, *Statistical physics: volume 5* (Elsevier, 2013).

[51] F. Le Kien, P. Schneeweiss, and A. Rauschenbeutel, Eur. Phys. J. D **67**, 1 (2013).

[52] G. E. Jellison and F. A. Modine, Appl. Phys. Lett. **69**, 371 (1996).

[53] H. R. Philipp, J. Electrochem. Soc. **120**, 295 (1973).

[54] A. Sommerfeld, *Optics lectures on theortical physics, vol. IV* (Academic Press, 1954).

Vers une mesure précise du potentiel Casimir-Polder entre des atomes d'argon métastables et un nanoréseau en transmission.

Depuis les années 1950, les interactions atome-surface, aussi appelées interactions Casimir-Polder, ont été étudiées au travers de nombreux travaux théoriques. Nombre d'expériences ont été proposées et réalisées afin de mesurer les interactions atome-surface. Pour autant, les expériences n'ont pas permis de mesurer le potentiel d'interaction atome-surface avec une incertitude inférieur à 10%. Dans cette thèse, nous présentons une expérience d'atomes froids dédié à l'étude des interactions Casimir-Polder. L'expérience repose sur la diffraction d'atomes d'argon métastables par un nanoréseau matériel en transmission. Au vu des vitesses de propagation des atomes, nous avons développé une simulation basée sur la résolution numérique de l'équation de Schrödinger dépendant du temps. Cette simulation nous permet d'étudier la diffraction d'un paquet d'ondes par une fente matérielle, tout en prenant en compte à la fois les interactions atome-surface et l'absorption de la fonction d'onde au contact des surfaces. Les résultats de la simulation sont confrontés aux données expérimentales à l'aide d'outils statistiques permettant de tester le modèle dans le but d'effectuer une mesure de précision

Mots-clés : Atomes froids, Casimir-Polder, Atome-surface, Simulation Schrödinger, Jet lent, Nanoréseau, Ondes de matières.

Toward accurate measurement of Casimir-Polder potential between metastable argon atoms and nanofrabricated transmission grating.

Since the 1950's, atom-surface interactions, also called Casimir-Polder interactions, have been studied through numerous theoretical works. Many experiments have been proposed and performed to measure the atom-surface interactions. However, the experiments did not allow to measure the atom-surface interactions potential with a better accuracy than 10%. In this thesis, we present a cold atom experiment dedicated to the study of Casimir-Polder interactions. The experiment is based on the diffraction of metastable argon atoms by a transmission material nanograting. Regarding the propagation velocities of the atoms, we have developed a simulation based on the numerical solution of the time-dependent Schrödinger equation. This simulation allows us to study the diffraction of a wave packet by a material slit, while considering both the atom-surface interactions and the absorption of the wave function at the surfaces. The results of the simulation are compared with the experimental data using statistical tools to test the model in order to make an accurate measurement.

Keywords : Cold atoms, Casimir-Polder, Atom-surface, Schrödinger Simulation, Slow atomic beam, Nanograting, Matter-wave.